We learn more by looking for the answer to a question and not finding it than we do from learning the answer itself.

– Lloyd Alexander, 1964.

University of Alberta

COMPUTER-AIDED ANALYSIS OF WHOLE SLIDE SKIN HISTOPATHOLOGICAL IMAGES

by

Cheng Lu

A thesis submitted to the Faculty of Graduate Studies and Research
in partial fulfillment of the requirements for the degree of

Doctor of Philosophy

in

Digital Signals and Image Processing

Department of Electrical and Computer Engineering

©Cheng Lu

Fall 2013
Edmonton, Alberta

Permission is hereby granted to the University of Alberta Libraries to reproduce single copies of this thesis and to lend or sell such copies for private, scholarly or scientific research purposes only. Where the thesis is converted to, or otherwise made available in digital form, the University of Alberta will advise potential users of the thesis of these terms.

The author reserves all other publication and other rights in association with the copyright in the thesis and, except as herein before provided, neither the thesis nor any substantial portion thereof may be printed or otherwise reproduced in any material form whatsoever without the author's prior written permission.

This thesis is dedicated to

my beloved parents, Hongguang Lu and Xiaoning Lu,

my grandparents, Zhengyu Lu and Cuizhen Teng, and my soulmate Zhen Ma.

Abstract

The histopathological examination of a biopsy is considered as the gold standard in the diagnosis of diseases for almost all kinds of cancer.Traditionally, the histopathological slides are examined under a microscope by pathologists. Nowadays, with the help of high speed, high resolution image scanning technique, a glass slide can be digitized at high magnification to create a digital whole slide image (WSI). Manual examination of the glass slides and the WSIs are time-consuming and difficult. Also, the traditional diagnosis is subjective and often leads to intra-observer and inter-observer variability. In this dissertation, I develop several key techniques of the computer-aided diagnosis (CAD) system for digital histopathological image analysis of skin specimen of melanocytic disease. This CAD system operates on reliable quantitative measures and provides objective and reproducible information that can be used by pathologist for diagnosis.

The proposed CAD system has six modules. In the first module, the whole slide skin image is automated segmented into biologically meaningful parts: epidermis and dermis. The high resolution image tiles of interest are then generated for further analysis. In the second module, the nuclei in the epidermis area are segmented using the proposed hybrid gray-scale morphological reconstructions and local region

adaptive threshold selection methods. In the third module, two efficient techniques based on local double ellipses descriptor analysis and radial line scanning analysis are proposed to detect the melanocytes. In the fourth module, an efficient technique is proposed to detect the mitotic cells in the multi-spectral histopathological images. Based on the pre-segmented regions of interest (ROI), the morphological features and the spatial relationship are analyzed in the fifth module. These features reveal the cytological and architectural characteristics of the tissue sample that are correlated to the disease diagnosis. In the last module, classification is performed using the pre-extracted features in order to grade the skin tissue.

The experimental results based on a set of skin WSIs show that the proposed CAD system is able to provide objective and reproducible measures that can assist to the final diagnosis by pathologist.

Acknowledgments

First and foremost, I would like to express my sincere gratitude to my supervisor, Prof. Mrinal Mandal and Dr. Naresh Jha for their encouragement, guidance and invaluable support throughout my graduate studies. All my achievements have been benefited from their knowledge, and inspiration. These years which I have been under their supervision will be remembered as one of my "life honor".

I am deeply indebted to Dr. Muhammad Mahmood, who has been my research collaborator during the past three years, for his valuable guidance and suggestions during our collaborative research. I learned and gained enormously from his knowledge and experience. It would not have been possible to write this thesis without his help.

I would also like to thank the members of my defense committee, for taking their previous time to review my thesis and giving valuable suggestions for my research. I am deeply grateful to my committee members: Dr. Roger J. Zemp, Dr. Hong Vicky Zhao, Dr. Nilanjan Ray, who provided valuable suggestions and comments during the course of my PhD tenure.

I would also like to acknowledge the China Scholarship Council (CSC) and my alma mater Northwest Agricultural and Forestry University (especially my previous supervisor Dr. Dongjian He), for awarding me the scholarship to support my study at University of Alberta.

Much respect to my labmates, classmates, and friends. Dr. Gencheng Guo, Dr. Tao Xu, Dr. Ming Ying, Dr. Mingli Song, Dr. Rongfei Fan, Dr. Bo Hu, Dr. Yanan Fu, Dr. Hengzhen Gao, Dr. Saman Atapattu, Mr. Jorge Morales, Mr. Chao Feng, Mrs. Yue Li, Mr. Jianzhao Huang, Mr. Peng Shao, Mr. Heting Fu and his wife, Mr. Yue Yang, Mr. Fuyong Li, Mr. Jichuan Shi, Mr. Ming Liu, Mr. Zhao Xu, and many others. They make my days meaningful and happy. The years I spent at the University of Alberta is an unforgettable period of learning and working experience.

Heartiest thanks to my girlfriend, Zhen Ma, now a Postdoctoral fellow at Agriculture and Agri-food Canada (Saint Hyacinthe, Quebec, Canada), for her faithful love, infinite and long distant support and care.

Last but far from the least, my heartiest love and thanks to my parents, Hongguang Lu and Xiaoning Lu, my grandparents, Zhengyu Lu and Cuizhen Teng: thank you for your tremendous love, devotion and encouragement throughout my life, for which mere words cannot express my gratitude.

Table of Contents

1 Introduction **1**

1.1 Skin Cancer and Diagnosis 1

1.2 Problem Statements and Motivation 2

1.3 Major Contribution of the Thesis 3

1.4 Organization of the Thesis 4

2 Background and Related Work **5**

2.1 Histopathological Image (HPI) 5

2.2 Skin HPI Understanding 6

2.2.1 The Histopathological Aspects of Human Skin 6

2.2.2 Manual Examination of the Skin Tissue 8

2.3 Review of Automated HPI Analysis 11

2.3.1 Region of Interest Segmentation 11

2.3.2 Feature Extraction 16

2.3.3 Classification 20

2.3.4 Whole Slide HPI Analysis Techniques 20

2.3.5 HPI Analysis for Skin Cancer 22

2.4 Summary 23

3 The Proposed System **24**

3.1 Challenges 24

3.1.1 Staining Variations 24

3.1.2 Computational Effectiveness 25

3.1.3 Discriminant Features Extraction 26
3.2 Overview of the Proposed System 26

4 Segmentation and Analysis of the Epidermis 28
4.1 The Proposed Technique 29
4.1.1 Selection of a Monochromatic Color Channel 30
4.1.2 Down-sampling 33
4.1.3 Segmentation of Epidermis 33
4.1.4 Determine Layout and Generate Image Tiles 35
4.2 Performance Evaluation 39
4.3 Summary 41

5 Segmentation of the Cell Nuclei 42
5.1 Introduction 42
5.2 The Proposed Technique 45
5.2.1 Hybrid Gray-scale Morphological Reconstructions 45
5.2.2 Segmentation of the nuclei using LRATS 48
5.3 Performance Evaluation 52
5.3.1 Image Data 52
5.3.2 Manual Identification of the Nuclei 52
5.3.3 Evaluation Metrics 53
5.3.4 Compare LRATS with Watershed 55
5.4 Summary 63

6 Detection of the Melanocytes 64
6.1 Introduction 64
6.2 Proposed LDED-based Technique 68
6.2.1 Segmentation of Nuclei 69
6.2.2 Local Double Ellipse Descriptor Analysis 69
6.3 Proposed RLS-based Technique 78
6.3.1 Segmentation of the Nuclei 79

6.3.2 Estimation of the Halo Regions using RLS 79
6.3.3 Detection of the Melanocytes 88
6.4 Performance Evaluation 89
6.4.1 Evaluation Metrics 89
6.4.2 Parameters Selection 91
6.4.3 Evaluation on Halo Region Estimation 92
6.4.4 Quantitative Evaluation on Detection 93
6.4.5 Qualitative Evaluation on Detection and Segmentation . . . 96
6.4.6 Comparison of LDED and RLS Complexity 97
6.5 Summary 98

7 Detection of Mitotic Cells **100**
7.1 Introduction 100
7.2 The Proposed Technique 105
7.2.1 Discriminative Image Generation 106
7.2.2 Detection and Segmentation of MC Candidates 109
7.2.3 Classification of MC Candidates 115
7.3 Performance Evaluation 118
7.3.1 Image Data 118
7.3.2 Segmentation Performance Evaluation 120
7.3.3 Detection Performance Evaluation 122
7.4 Summary 125

8 Classification of the Skin WSI **127**
8.1 Introduction 127
8.2 The Proposed Technique 127
8.2.1 The Overview of the Proposed Technique 127
8.2.2 Epidermis Area Segmentation 128
8.2.3 Nuclei segmentation 132
8.2.4 Melanocytes Detection 135
8.2.5 Features Construction: Spatial Distribution Features 137

8.2.6 Features Construction: Morphological Features 141
8.2.7 Classification 142
8.3 Performance Evaluation 143
8.3.1 Image Dataset 143
8.3.2 Performance Comparison 143
8.3.3 Computational Complexity Evaluation 146
8.4 Conclusion 146

9 Conclusions and Future Research Direction **147**
9.1 Conclusions 147
9.2 Publications 149
9.3 Future Work 150

References **152**

Appendix A Histopathological Knowledge **166**
A.1 Physiological Terms 166
A.1.1 General Terms 166
A.1.2 Four Layers in Skin Epidermis 167
A.1.3 Biological Components in Skin Tissue 168
A.2 Tissue Slide Preparation 172
A.3 Histopathological Image Acquisition 173
A.4 The Histopathological Aspects of Skin Tumors 173

Appendix B Direct least square fitting algorithm **175**

List of Tables

2.1 Related works on the whole slide histopathology image analysis . . 21

4.1 The approximate optimal linear transform $\tilde{A}$ with its R_{II} value for 8 test WSIs. 32

4.2 The quality metric R_{II} for the R, G, B, Gray, H, S, V channels of 8 WSIs. 32

4.3 Performance evaluation of the epidermis segmentation. 40

5.1 Performance evaluations of the proposed technique with other existing techniques on skin epidermis images. 58

6.1 Performance evaluation of the halo region estimation. 92

6.2 Comparison of LDED, RLS, and TM techniques in terms of processing time. 98

7.1 Comparison of the existing MC detection techniques. (NSC:number of spectral channels; TI:time information.) 104

7.2 The summary of features extracted from the candidate MC regions and the surrounding regions 116

7.3 Properties of the 10 spectral bands. 120

7.4 MCs segmentation performance evaluation. 121

7.5 The performance of the proposed technique 123

7.6 The performance comparison 124

8.1 Description of the image dataset. 143

8.2 Performance evaluations. 144

A.1 Description of three common skin cancers. 174

List of Figures

2.1 An example of H&E staining histopathological image. 6
2.2 Anatomy of normal skin. 7
2.3 Anatomy of epidermis and dermis in normal skin. 7
2.4 An example of the single cell and cell nest. 9
2.5 An example of the buckshot pattern. 9
2.6 Example of the LoG filter. 15
2.7 A histopathological image and its corresponding graph structures. . 19

3.1 Four examples of skin histopathological images captured on magnification 25X. 25
3.2 The overall schematic of the proposed CAD system. 26

4.1 The anatomy of a skin tissue. 29
4.2 The schematic for the WSI segmentation. 30
4.3 An example of the WSI. 33
4.4 Three examples of epidermis segmentation. 35
4.5 An example for determining the layout of the epidermis. 37
4.6 An illustration of the horizontal image tile and vertical image tile. . 37
4.7 An example of generating the reasonable image tiles. 38

5.1 H&E stained histopathological images. 43
5.2 The schematic for the proposed technique. 45
5.3 An example of the hybrid gray-scale morphological reconstruction. 46
5.4 Segmentation of nuclei using LRATS. 49

5.5 Final results obtained by the proposed technique. 52
5.6 Segmentation performance of the LRATS and watershed techniques. 57
5.7 Performance comparison of the nuclei segmentation techniques. . . 58
5.8 Segmentation performance comparison of the nuclei segmentation techniques in terms of nucleus area. 60
5.9 Segmentation performance comparison of the nuclei segmentation techniques in terms of nucleus perimeter. 61
5.10 Segmentation performance comparison of the nuclei segmentation techniques in terms of nucleus form factor. 62

6.1 Melanocytes in epidermis area from different skin tissues. 65
6.2 The schematic of the proposed LDED based technique. 69
6.3 An example of the mean shift segmentation. 69
6.4 The Elliptical modeling for each nucleus. 70
6.5 Illustrations of two parameters e_E and e_D for three different candidate nuclei regions. 72
6.6 The manually cropped melanocytes and other nuclei as well as the corresponding histograms. 74
6.7 Illustration of the LDED analysis. 77
6.8 The schematic of the proposed melanocyte detection technique. . . 79
6.9 Illustration of the RLS algorithm. 80
6.10 Illustration of the notation of radial center and radial line. 81
6.11 A close up example of a melanocyte with gradient map. 84
6.12 Illustration of the outer boundary point detection on a given radial line. 86
6.13 Two examples of halo-like regions estimation. 87
6.14 Examples of the estimated halo regions compared to manually labeled halo regions. 93
6.15 Ten templates used in the template matching techniques. 94

6.16 The ROC and PRC curves of the proposed techniques and the TM technique. 95
6.17 Three examples for qualitative evaluation. 96

7.1 Examples of MCs in 5 mitotic phases. 101
7.2 Three examples of the MC in a portion of a HPF image captured at 40× magnification. 102
7.3 The schematic of the DMKC technique. 103
7.4 The overall schematic of the proposed technique. 106
7.5 An example of all 10 band spectral images((a) to (j)) and the DI ((k)). 110
7.6 The schematic of module 2. 111
7.7 The example of the MC candidates detection and intact region segmentation. 111
7.8 A close up example for the non-intact candidate MC region. 113
7.9 Illustration of the local threshold method. 115
7.10 The schematic of the classification module. 115
7.11 Examples of the segmented MC regions compared to manually labeled MC regions. 121
7.12 Subjective evaluation of DMKC and the proposed technique. 125

8.1 The overall schematic of the proposed technique. 128
8.2 The anatomy of a skin tissue. 129
8.3 The schematic for epidermis area segmentation module. 129
8.4 An example of generating the image tiles. 131
8.5 Three examples of the epidermis segmentation results. 132
8.6 Example of hybrid gray-scale morphological reconstruction. nuclei segmentation result in epidermis area. 134
8.7 An example of nuclei segmentation result in epidermis area. 135
8.8 Melanocytes in epidermis area from different skin samples. 136
8.9 The schematic of the melanocyte detection technique. 136
8.10 138

8.11 Epidermis depth measurement, and construction of sub-layers for the epidermis. 139
8.12 An example of misclassified skin tissue. 145

A.1 The atlas of cytological components. 168
A.2 The atlas of melanocytes. 170
A.3 The anatomy of histopathology skin specimen. 171

List of Abbreviations

Acronyms	Definition
AT	adaptive threshold
ALR	abnormally large region
CAD	computer aided diagnosis
EM	expectation maximization
FPR	false positive rate
FVPC	follicular variant of papillary carcinoma
GAC	geometric active contour
GT	global threshold
HC	halo contour
HGMR	hybrid gray-scale morphological reconstructions
HPF	high power field
HR	high resolution
HT	hysteresis threshold
H&E	haematoxylin and eosin
LR	low resolution
LRATS	local region adaptive threshold selection
LRRS	local region recursive segmentation
MAD	mean absolute differences
NCC	normalized cross correlation
PRC	precision-recall curve
PRE	precision
RLS	radial line scanning

ROC	receiver operating characteristic
ROI	region of interest
SD	standard derivation
SEN	sensitivity
SVM	support vector machine
TM	template matching
TCA	tissue counter analysis
TPR	true positive rate
USR	under segmentation rate
VT	variational threshold
WS	watershed
WSI	whole slide image

List of Symbols

Symbols	Definition
$\mathcal{A}_{SEN}$	area-based sensitivity
$\mathcal{A}_{PRE}$	area-based precision
C^{GT}	contour of the ground truth region
C^{EST}	contour of the estimated region
N_{TP}	number of true positive
N_{FP}	number of false positive
N_{TN}	number of true negative
N_{FN}	number of false negative
N_{DO}	number of detected objects
$\mathbf{A}$	The matrix $\mathbf{A}$
$\mathbf{A}^{-1}$	The inverse matrix of $\mathbf{A}$
$\mathbf{a}$	The vector $\mathbf{a}$
$\mathbf{I}_N$	The $N \times N$ identity matrix
$\mathbf{0}_{M \times N}$	$M \times N$ all-zero matrix
$\nabla\phi$	the gradient of the function ϕ
$\lceil a \rceil$	Integer ceiling of a
$\lfloor a \rfloor$	Integer floor of a
$\|A\|$	L-1 norm of A
$\|A\|^2$	L-2 norm of A
$\frac{dx}{ds}$	Derivative of x with respect of s
$\frac{\partial\phi}{\partial s}$	Partial derivative of ϕ with respect of s
$\|B\|$	Cardinality of set B

$\overline{B}$	The complement of set B
$\{B_p\}_{p=1...Z}$	A set named B which indexed by p and contains 1 to Z elements
$\oplus$	Exclusive operator

Chapter 1

Introduction

Computer-aided diagnosis (CAD) plays an important role in emerging clinical diagnosis procedures, and provides objective measures to assist doctors in providing more accurate diagnosis, with the promise of reducing the workload of these doctors [1]. Typical applications include detection of breast cancer from mammograms [1] and segmentation of the cavity in chest X-rays [2]. Existing CAD systems have demonstrated utility for tedious tasks such as counting the malignant cells in biopsy tissue, and tasks that involve a complex combination of multiple image features. CAD can help to reduce the inter-observer or intra-observer variation [3]. Typically, CAD is an interdisciplinary technology combining artificial intelligence, digital image analysis and domain-knowledge for diseases diagnosis. With the rapid development of artificial intelligence and digital image processing techniques, CAD systems have the potential to provide precise and reproducible objective measurements which can help to greatly improve the physicians' performance.

1.1 Skin Cancer and Diagnosis

Cancer is a major cause of death all over the world. It is caused by the uncontrolled growth of abnormal cells in the body. Skin cancer is one of the most frequent types of cancer, and melanoma is the most aggressive type of skin cancer [4]. Accord-

ing to a recent article, approximately 70,000 people are diagnosed with melanoma skin cancer, and about 9,000 die from it in the United States alone every year [5]. Malignant melanoma is curable, if it is diagnosed at early stages [4]. Therefore, an early detection and accurate prognosis of malignant melanoma will definitely help to lower the mortality from this cancer. Approaches to melanoma diagnosis have dynamically evolved during the last 25 years [6]. Although there are many new emerging techniques, e.g., dermatoscopy [7] that could provide initial diagnosis, pathological examination remains the gold standard for the final diagnosis. In addition, useful prognostic information in the clinical management of the patient can also be provided by the histological examination.

1.2 Problem Statements and Motivation

Histopathology slides provide a cellular-level view of the diseased tissue, and is considered the "gold standard" in the diagnosis of diseases for almost all kinds of cancer [8]. Traditionally, histopathological slides are examined under a microscope by pathologists. The diagnostic decisions are then made based on their personal experience. However, the decisions are subjective and often lead to intra-observer and inter-observer variability [9]. To address this problem, automated computational tools which can provide reliable and reproducible objective results for quantitative analysis are needed.

With the help of whole slide histology digital scanners, glass slides of tissue specimen can now be digitized at high magnification to create the whole slide image (WSI) [10], [11]. Such high resolution images are similar to what a pathologist observes under a microscope to diagnose the biopsy. However, quantitative analysis of digitized whole slide image is time-consuming and difficult. Recently, researchers have applied sophisticated digital image analysis techniques to extract more objective and accurate prognostic clues throughout the WSI. Additionally, instead of accessing only representative regions, the computerized system can process the whole-slide and prevent sampling bias.

Due the complexity of human tissues, the architectural and morphological features in a histopathology image are totally different. Based on the whole slide image, several research groups have been developing CAD systems for the analysis and diagnosis of cancer tissues for breast cancer [12], [13], prostate cancer [14], head and neck cancer [15], cervical cancer [16], neuroblastoma [17], [18], and ovarian cancer [19]. To the best of our knowledge, there is no CAD system designed for the whole slide image of skin cancers.

The main goal of this dissertation is to develop a CAD system for digital histopathological image analysis of skin specimen of melanocytic disease, which will assist pathologists for more precise diagnosis in clinical practice. This CAD system will operate on reliable quantitative measures in skin epidermis and will provide objective and reproducible information that can be used by pathologist for diagnosis.

1.3 Major Contribution of the Thesis

- A computer-aided technique for segmentation and analysis of the epidermis area in the whole slide skin histopathological images [20] (presented in Chapter 4).
- An efficient technique for segmentation of nuclei from histopathological images [21] (presented in Chapter 5).
- Efficient techniques for melanocyte detection using local double ellipses descriptor (LDED) [22], and using radial line scanning (RLS) [23] (presented in Chapter 6).
- An efficient technique for automatic detection of the mitotic cell in multispectral stained histopathological images [24] (presented in Chapter 7).
- An efficient feature extraction and classification technique for the whole slide skin pathological image [25] (presented in Chapter 8).

1.4 Organization of the Thesis

The rest of this thesis is organized as follows: Chapter 2 presents the background knowledge of histopathology on skin tissues, together with the literature review on the topic of histopathological image analysis. Chapter 3 presents an overview of the proposed CAD system. In Chapter 4, the research on epidermis segmentation, analysis of the whole slide image, and high resolution image tile generation are presented. Chapter 5 discusses an automatic cell nuclei segmentation technique using hybrid morphological operation and local region adaptive threshold selection. Chapter 6 presents two automatic techniques, the local double ellipse descriptor (LDED) and radial line scanning (RLS) techniques, for the melanocytes detection in epidermis area. Chapter 7 presents an automatic technique for mitotic cell detection using multi-spectral images. Chapter 8 presents the classification system that utilized the features extracted from pre-segmented and detected ROIs. Future work and conclusion for the research is presented in Chapter 9, which is followed the bibliography and appendix.

Chapter 2

Background and Related Work

In this chapter we present a brief introduction to the general histopathological imagery and the skin histopathological images. We also discuss the related image analysis techniques and the state of the art techniques related to the histopathological image analysis.

2.1 Histopathological Image (HPI)

Histology is the study of cell or tissue at microscopic level, and pathology is the study and diagnosis of the disease. The histopathology is the study on the manifestations of disease via microscopic examination of tissue [26]. Specifically, in clinical settings, histopathology refers to the examination of a surgical specimen by a pathologist. The surgical specimen is typically processed and placed on a glass slide [26]. In order to obtain a digital tissue specimen image, two main procedures are needed: tissue slide preparation and digital image acquisition. The details of these two main procedures are presented in the Appendix (Sections A.2 and A.3). The image captured by a microscope is referred to as the histopathological image in this thesis.

Traditionally, the tissue specimens are stained with haematoxylin and eosin (H&E). The haematoxylin is a blue-staining dye and the eosin is a pink-staining dye. Fig. 2.1 shows an example of the H&E stained histopathological image. It

is observed that the cell nuclei have been stained as blue-purple due to the haematoxylin whereas the intra-cellular and cytoplasm are stained as bright pink due to the eosin.

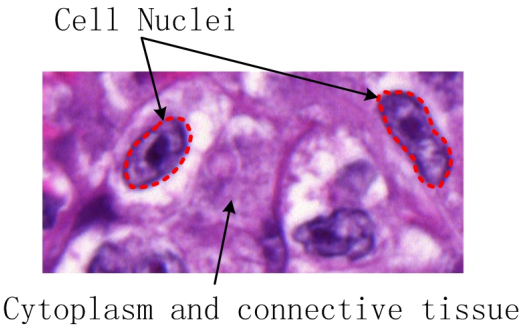

Fig. 2.1. An example of H&E staining histopathological image.

2.2 Skin HPI Understanding

In this section, the histopathological aspect of the skin specimen is described, followed by the description of the traditional skin tissue examination procedure used in dermatopathology. Definition of selected biological terms used in this section can found in Appendix A.1.

2.2.1 The Histopathological Aspects of Human Skin

It is important to note that human skin consists of three main layers: epidermis, dermis and subcutaneous tissue. An anatomy of normal skin is shown in Figure 2.2. The different layers are described below [27].

Epidermis: The epidermis is the outer layer of the two main layers of cells that builds up the skin [26]. The epidermis and dermis together form the cutis. The thickness of epidermis varies according to body site, normally in the range of 50 to 150 μm. It mainly contains keratinocytes, melanocytes, and Langerhans cells [28]. An H&E stained pathology image of normal human skin and its anatomy is shown in Fig. 2.3. Based on the maturation of keratinocytes, the epidermis can

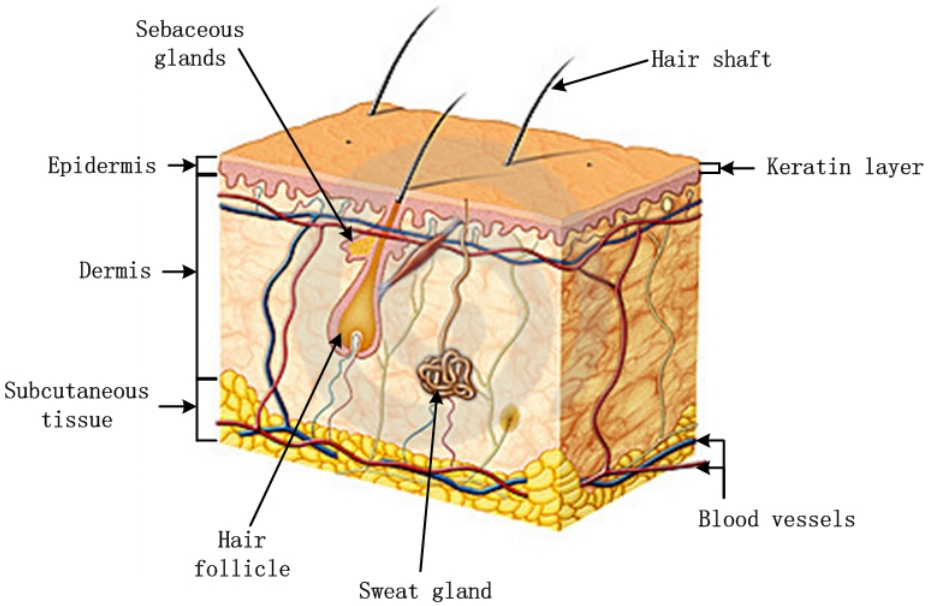

Fig. 2.2. Anatomy of normal skin.

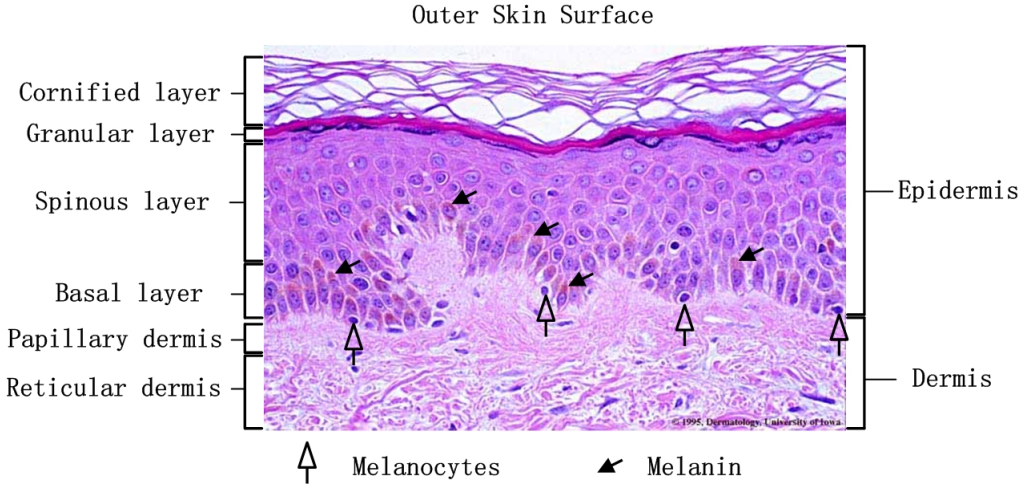

Fig. 2.3. Anatomy of epidermis and dermis in normal skin [29]. The hollow arrows and solid arrows point out the melanocytes and melanin, respectively.

be divided into four major layers: basal layer, spinous layer, granular layer and cornified layer. Note that the basal layer is the innermost layer and the cornified layer is the outermost layer.

Dermis: The dermis area is defined as the inner layer of the two main layers of cells that build up the skin [26]. The thickness of this layer is in the range of 1 to 4 mm. The dermis contains blood vessels, lymph vessels, hair follicles, and sweat glands. The dermis area can be further divided into papillary dermis and reticular dermis (see Fig. 2.3).

Subcutaneous Tissues: The subcutaneous tissue is the innermost layer of skin. It contains fat and connective tissue that holds larger blood vessels and nerves. Some cytological components in dermis and subcutaneous tissue area are explained in Appendix A.1.3. The corresponding anatomy is shown in Fig. A.3.

2.2.2 Manual Examination of the Skin Tissue

There are four main groups of features that a dermatopathologist typically use to distinguish the melanocytic nevus and melanoma for a skin specimen. These four main groups of features are described in the following.

2.2.2.1 Architectural features within epidermis

- Lesional breadth: The broader the lesion, the higher is the chance to be melanoma.
- Number of single cells and nests: The ratio of the number of the nests of the melanocytes and single melanocytes is an indicator for the diagnosis. In the case of melanoma, a large number of single cells are presented. In the case of melanocytic naevus, a large number of cell nests are presented (see Fig. 2.4 for the example).
- Scattering of melanocytes in epidermis area: In certain type of melanoma (e.g., in the early stage of superficial spreading melanoma), the atypical melanocytes radially grow throughout the epidermis, which is also known as “buckshot pattern" (see Fig. 2.5 for the example).

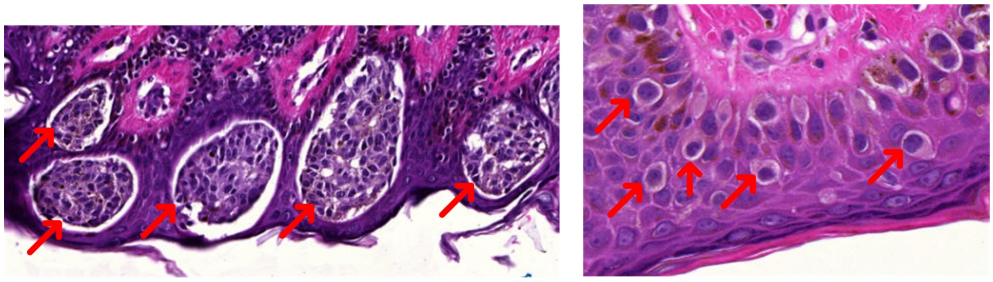

(a) (b)

Fig. 2.4. An example of the single cell and cell nest. (a) shows the nevus, where the melanocytes are forming several nest on the junction of epidermis and dermis (marked by arrows). (b) shows the epidermis area of melanoma. The single melanocytes are invading into the epidermis. These images were generated by scanning histopathological slides obtained from University of Alberta Hospital)

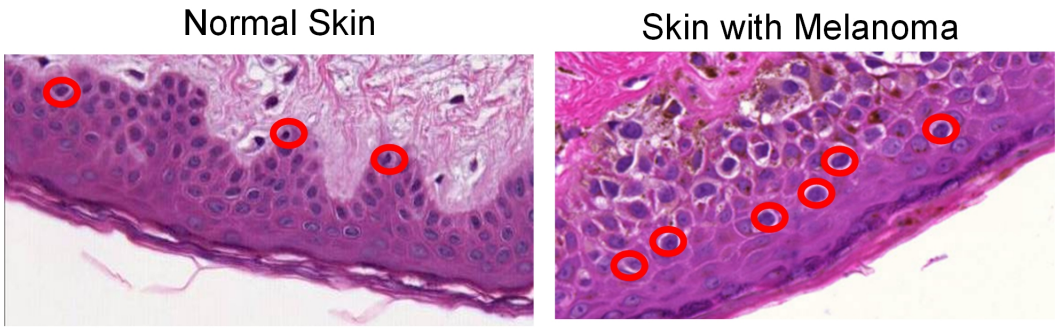

(a) (b)

Fig. 2.5. An example of the buckshot pattern. (a) shows the normal skin, where the melanocytes are lying on the junction of epidermis and dermis (melanocytes are marked with thick circles). (b) shows the epidermis area of melanoma. The melanocytes are invading into the epidermis and form the buckshot pattern (the horizontally spreading of melanocytes in epidermis area).

- Configuration of the epidermis: If the epidermis grows smooth, then more likely it is nevus or normal skin. If it grows in irregular fashion then more likely it is melanoma.
- Actinic elastosis: Generally, actinic elastosis (an accumulation of abnormal elastin inside the dermis area) are present in nevus only.

2.2.2.2 Cytological features in the epidermis/ dermis

- Size: The size of the melanocytes in the case of melanoma is larger than that in nevus and normal skin.

- Nucleus contour: The shape and the contour of the nucleus in normal and nevus skin tissue is regular, uniform and rounded, whereas it is irregular, nonuniform and not smooth in the case of melanoma.

- Prominent nucleolus: If the nucleolus occupies large area in the nucleus area, it is more likely to be melanoma.

- Hyperchromatism (excessive nuclear staining): In the case of melanoma, the stain is more intense than normal.

- Mitosis: If a large number of mitosis activities are observed in the epidermis/dermis area, it is more likely to be melanoma.

2.2.2.3 Architectural features in the dermis

- Contour of the base: For the nevus, the base of the dermis grows smoothly, whereas for the melanoma, the base of the dermis grows in irregular fashion.

- Invasion of melanocytes in dermis area: In certain type of melanoma (e.g., nodular melanoma), the melanocytes are invading into the deep dermis area.

- Maturation: In the case of melanoma, little or no maturation (i.e., the presence of all stages of cell growth) is observed. In the case of nevus, most maturation cells can be found at the deepest extent of lesions, where they often acquire fusiform contours and grow in fascicles resembling neural tissue.

Note that in biomedical setting, it is difficult to make a 100% correct judgement based on the features mentioned above, even by an experienced dermatopathologist. None of the above features is solely a marker for the diagnosis of the cancer. Traditionally, the expert knowledge and the experience of the dermatopathologist are helpful in making the diagnosis. In this thesis, I focus on the features in epidermis area.

2.3 Review of Automated HPI Analysis

In this section we present a brief review of the recent literature on histopathological image analysis.

2.3.1 Region of Interest Segmentation

One of the essential steps for diagnosis using histopathology image of a specimen is to detect and segment the cytological objects, structures and areas, for example, detection of the mitotic cells in an image [30], [31] or segmentation of the different cytological areas (e.g., different kind of cells, tubules) in a whole slide image [12]. The morphological features and architectural features of these regions/objects of interest are usually important factors to be considered by a pathologist. Numerous studies have been conducted on the detection and segmentation of different cytological components in histopathological images. In the following, we review five broad categories of techniques.

A. Threholding

Thresholding is one of the simplest but effective technique in image segmentation. However, it is well known that a single threshold usually fail in the presence of inter- and intra-object illumination variations. Therefore, various thresholding techniques have been proposed to achieve better segmentation results [12], [32]–[34]. Gurcan *et al.* [32] proposed a hysteresis threshold based technique that combines the *top-hat by reconstruction* method and watershed for the nuclei segmentation in neuroblastoma image. The hysteresis thresholding uses two thresholds in order to avoid the disconnected segmentation result while local variations are presented. Korde *et al.* proposed a global threshold based technique to segment the nuclei in the skin tissue image [33]. Petushi *et al.* proposed to use adaptive threshold for the nuclei segmentation in the breast cancer image [12]. The adaptive threshold technique computes the local threshold for each non-overlap block in the whole image using the mean intensity value. Note that the above mentioned threshold-based

techniques usually lead to under segmentation or mis-segmentation if there exist considerable intensity variations.

B. Watershed

Another popular technique for image segmentation is the watershed technique [35]. The watershed technique mimic the water flooding procedure and treat the image as a topological surface. By iteratively filling the "water" from different local minimum regions, the watershed technique can partition the image via labeling ridges where different evolving regions meet. The problem with watershed technique is that for the high texture or noisy image, the watershed technique technique will easily generate over-segmentation results. In order to tackle this problem, several marker-controlled watershed techniques are proposed [36]–[38]. In these works, the starting regions for the watershed technique are determined by the marker determination function instead of the inaccurate local minimum regions. The assumption of the marker-controlled watershed techniques is that the marker is really representing one desired object in the image. Under-segmentation and over-segmentation may also be present if the marker determination function produces inaccurate number of markers.

C. Bayesian Model

A popular category of segmentation techniques utilize the probabilistic model to classify the pixels into object and background. The Bayesian theorem is widely used in such techniques. The Bayesian theorem for posterior is defined as follows:

$$P(\omega_j|X) = \frac{p(X|\omega_j)P(\omega_j)}{p(X)} \tag{2.1}$$

where X is the feature vector (e.g., intensity, texture) of one pixel obtained from the image, ω_j, $j \in 1, ..., K$, indicates the class corresponding to the pixel, and K is the number of classes. The likelihood function $p(X|\omega_j)$ indicates the probability of certain observed features given a certain class ω_j. The prior $P(\omega_j)$ indicates the proportion of different classes present in the image. The likelihood and the prior

terms are usually determined using training samples. Given a pixel from the unseen image, the posterior probability $P(\omega_j|X)$ that a pixel belongs to class ω_j given features X can now be calculated using Eq. 2.1. By using probabilistic model to classify the pixel, Naik *et al.* [39] segmented the image into three classes: lumen, cytoplasm, and nuclei, for breast and prostate cancer diagnosis. Sertel *et al.* [40] segmented the mitosis and karyorrhexis cell from the background in neuroblastoma image. Similarly, Basavanhally *et al.* [41] used the Bayesian model to detect the lymphocytes in breast cancer image. Fatakdawala *et al.* [42] used the expectation maximization (EM) algorithm to determine the initial lymphocyte class from breast cancer histopathological image based on the posterior calculation. Note that the performance of such training-based techniques are very sensitive to the training samples.

D. Active Contour Model

A more sophisticated technique for image segmentation is the active contour technique. In the parametric active contour technique (also known as snake), a continuous curve in 2-D plane is defined by its x and y coordinates. The two coordinates are function of a parameter s, i.e., a curve is represented by $(X(s), Y(s)), s \in [0, 1]$. For example, a closed curve that has a circular shape is represented by $(cos(2\pi s), sin(2\pi s)), s \in [0, 1]$. Denote the predefined parametric curve as snake, the snake will evolve based on the energy function E_{total} defined as follows:

$$E_{total} = E_{int} + E_{ext} \tag{2.2}$$

where E_{int} is a function of the internal energy, E_{ext} is a function of the external energy. The internal energy is used to regularize the snake, i.e., to make sure that the snake is smooth. The internal energy is defined as follows:

$$E_{int} = \frac{1}{2}\int_0^1 \left[\alpha\left(\left|\frac{dX}{ds}\right|^2 + \left|\frac{dY}{ds}\right|^2\right) + \beta\left(\left|\frac{d^2X}{ds^2}\right|^2 + \left|\frac{d^2Y}{ds^2}\right|^2\right)\right] ds \tag{2.3}$$

Normally, the external energy is defined based on the magnitude of the image. Based on the energy function, the snake will evolve such that the E_{total} is minimized with respect to $X(s)$ and $Y(s)$. The calculus of variations and gradient descent can be used to solve the minimization problem [43]. After the evolution, the snake will encompass the desired ROI for the segmentation purpose.

A variant of active contour technique is called geometric active contours. In these technique, the level set approach [44] is used to evolve the geometric active contour which is represented as the intersections of an implicit surface function ϕ and the zero level plane. The evolution of the level-set function ϕ is achieved by solving the following partial differential equation:

$$\frac{\partial \phi}{\partial t} + \mathbf{F}|\nabla \phi| = 0 \tag{2.4}$$

where $\nabla \phi$ is the gradient of the implicit surface function. $\mathbf{F}$ is the speed function indicates the velocity of the contour towards the object boundary. The speed function guides the curve evolution using the image properties such as the gradient or other geometrical property such as the curve curvature. The major limitation of the active contour technique is its sensitivity to the initialization and the local intensity variations. In addition, this technique has a high computational complexity. Fatakdawala *et al.* [42] and Nait *et al.* [39] employed geodesic active contour for the lymphocytes segmentation and gland structure in the breast cancer and prostate histopathological images, respectively.

E. Seed Point Detector

For many segmentation techniques, such as watershed technique and active contour based technique, initial location (or known as seed point) of the object of interest (e.g., nuclei) is usually required. Template matching technique is a popular technique in computer vision for seed point detection [45]. Naik *et al.* [46] have used four binary elliptical templates with different major and minor axes to detect the nuclei in breast cancer histopathological images. Al-Kofahi *et al.* [47] used a multi-scale Laplacian-of-Gaussian (LoG) filter to detect the marker for individual

nuclei. The LoG filter is defined as:

$$LoG(x, y; \sigma) = \frac{\partial^2 G(x, y; \sigma)}{\partial x^2} + \frac{\partial^2 G(x, y; \sigma)}{\partial y^2} \tag{2.5}$$

where σ is the scale factor, and $G(x, y; \sigma)$ is a Gaussian kernel with zero mean and scale σ, i.e.,

$$G(x, y; \sigma) = \frac{1}{2\pi\sigma} exp(-\frac{x^2 + y^2}{2\sigma^2}) \tag{2.6}$$

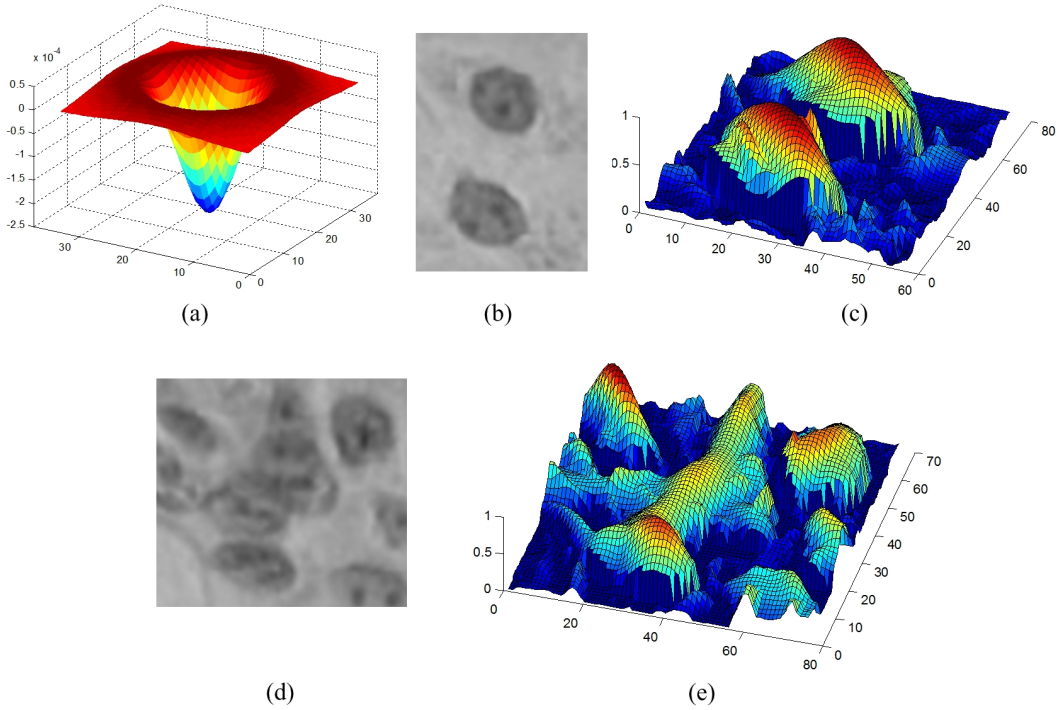

Fig. 2.6. Example of the LoG filter.(a) LoG filter with $\sigma = 6$. (b) An image contains two nuclei; (c) the response surface after apply the multi-scale LoG on the image (b). (d) An image contains clustered nuclei; (d) the response surface after apply the multi-scale LoG on the image (d). Note that the clustered nuclei are not separated from each other.

With varying scale factor σ, the multi-scale LoG approach accumulates the maximum values over the spatial domain to determine the final response surface. After the application of the multi-scale LoG to the histopathological image that contains blob-like nuclei, we can obtain higher responses near the center of the nuclei. An example of the multi-scale LoG filter for nuclei seed point detection is shown in Fig. 2.6 (b) and (c). Fig. 2.6(b) shows an original image with two nuclei, whereas

Fig. 2.6(c) shows the response surface after the application of the LoG filter. If a threshold is applied in Fig. 2.6(c), it is easy to identify the location of the two nuclei. In a similar way, Basavanhally *et al.* [41] used multi-scale Gaussian kernel to detect the initial lymphocytes in breast cancer image. It is noted that the multi-scale LoG method can provide satisfactory result when the nuclei and background are well differentiated or there are a few nuclei clustered in the image. If there are great variations in the shape of the nuclei or cluster of nuclei in a local region, the multi-scale LoG method will usually not work well. Specifically, it is difficult to sperate the nuclei since the multi-scale LoG method will obtain under-segmentation result. An example is shown in Fig. 2.6 (d) and (e), where there is a cluster of three nuclei in the middle. It is shown in Fig. 2.6(e) that the three nuclei are hardly separated in the response surface obtained by the LoG filter. The consequences of mis-interpreting two close nuclei as one may affect later important cell counting procedure which may lead to mistake grading.

2.3.2 Feature Extraction

After the detection and segmentation of the regions of interest (ROI), the features from these ROIs are used for further analysis. Generally, the useful features for disease diagnosis have been driven by the parameters the pathologist look for. For example, the pathologist may seek for the malignant cells which are hyperchromatism (excessive pigmentation) and pleomorphism (variability in the size and shape of cells and/or their nuclei). The color feature and the morphological feature (e.g., shape, size) of a cell can be used to detect malignancy. There are numerous research works on the feature extractions. The features mainly contains: morphological features, texture features, and the architectural features.

2.3.2.1 Texture features

Texture features are widely used in histopathological image analysis [48], [49]. The texture features describe the repeated patterns on the appearance, and quantitatively

measure the variation in an image. A widely used texture feature is based on the co-occurrence matrix. The gray-level co-occurrence matrix is defined as follows:

$$\mathcal{C} = \begin{bmatrix} p(1,1) & p(1,2) & \cdots & p(1,L_g) \\ p(2,1) & p(2,2) & \cdots & p(2,L_g) \\ \vdots & \vdots & \ddots & \vdots \\ p(L_g,1) & p(L_g,2) & \cdots & p(L_g,L_g) \end{bmatrix} \tag{2.7}$$

where L_g is the total number of gray levels, $p(i,j)$ is the probability of gray level i and j co-occurrent when they are adjacent pixels. The co-occurrence matrix records the spatial dependency between the gray-level pairs. The well known Haralick features [50] (e.g., contrast, correlation, energy, entropy, homogeneity, and dissimilarity) are derived from the co-occurrence matrix. These features have been used to analyze the stromal development in [17]. In [51], four of the Haralick features were used for the classification of the samples of skin tissue.

Another set of texture features is derived from the run-length matrix [52]. The gray-level run-length matrix quantifies the coarseness of the texture with a given direction in the image. By defying a gray-level run as a set of consecutive pixels with the same intensity u in a given direction θ, the element of the run-length matrix $\mathcal{R}(u,v)$ is the number of gray-level runs with a length of v and intensity u. Tosun *et al.* [53] proposed to compute the run-length matrix on the graph consisting of circular primitives representing the tissue components. The texture features derived from the graph-based run-length matrix are then used for the prostate histopathological image segmentation.

Other kinds of texture features such as local binary pattern [17] and Gabor features [14], [54] are also used for the tissue classifications.

2.3.2.2 Morphological features

The morphological features, which quantify the the shape and size of the object of interest, are very important in histopathological image analysis. The frequently

used morphological features are:

- **Area:** number of pixels in the ROI.
- **Centroid:** center of the (weighted) gravity of the ROI.
- **Elliptical features:** The features derived from the best fit ellipse [55] of the ROI. The features may include major and minor axes and the ratio between them, eccentricity, orientation, and ellipticity.
- **Perimeter:** number of pixels on the boundary of the ROI.
- **Convex hull features:** The features derived from the convex hull [56] of the ROI. It may include solidity, convex deficiency, convex area, and concavity.

The morphological features are usually combined with the texture features for the tissue type classifications [18], [57].

2.3.2.3 Architectural features

The architectural features (also known as topological features) measure the spatial arrangement and distribution of the ROIs in the histological image. The graphs are suitable structures for encoding the spatial information before the feature extraction. Basically, a graph is defined as $G = (V, E)$, where V is a set of vertices and E is a set of edges. To model the tissue states, the ROIs can be assigned as the vertices and certain type of graph can be constructed. There are many structures in the graph theory, and about 150 features can be extracted to measure the spatial relationship [49]. The Voronoi diagram and Delaunay triangulation are two widely used graph structures.

The Voronoi diagram is defined as a set of polygons $P = \{P_1, P_2, \ldots, P_m\}$, where m is the total number of the ROIs (e.g., nuclei). The polygon P_j is comprised of the pixels $\{p_q\}_{q=1,\ldots,n}$ in the image domain satisfying $d(p_q, c^j) = min_k\{\|p_q - c^k\|\}$, where c^j is the centroid of the jth ROI and the $d(a, b)$ is the distance between two pixels a and b. The Delaunay triangulation is constructed on top of the

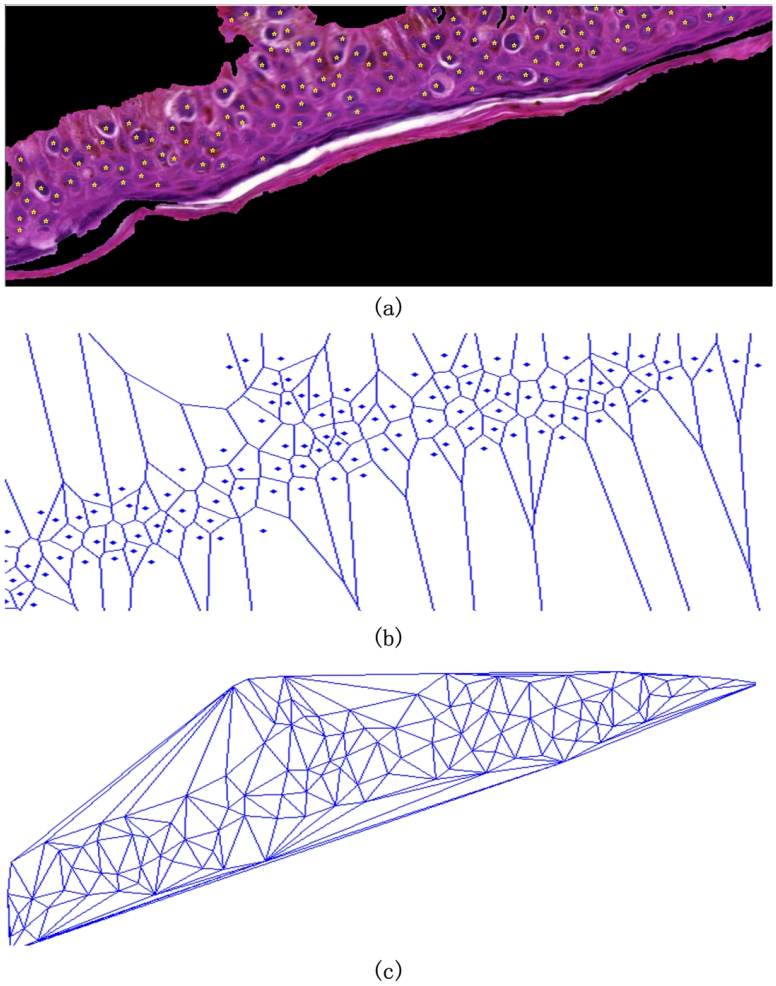

Fig. 2.7. A histopathological image and its corresponding graph structures. (a) A histopathological image with the nuclei location marked with bright stars. (b) the Voronoi diagram. (c) the Delaunay triangulation.

Voronoi diagram where the centroids of two ROIs are connected by an edge if the associated polygons share a side in the Voronoi Diagram. An example showing the Voronoi diagram, Delaunay triangulation, and minimum spanning tree for the nuclei in histopathological image is shown in Fig. 2.7.

In order to model the spatial information, Basavanhally *et al.* [41] constructed the Voronoi diagram, Delaunay triangulation, and minimum spanning tree based on the detected lymphocytes. The features derived from these graph structures are used for the breast cancer grading. Bilgin *et al.* [58] proposed a graph-based method for distinguishing different types of cells in the image. Altunbay *et al.* [59] mod-

els the spatial relationship of different tissue components by using the color graph. The Delaunay triangulation is first constructed based on the detected tissue components. The edges are assigned with different colors between the tissue components. Features are then derived from this color graph for colon cancer diagnosis.

2.3.3 Classification

One of the main goals of the histopathological image analysis is the classification of tissue types. The classification results may be influenced by many factors such as training samples, extracted features and the classifier. Many classifiers such as K-NN classifier [17], Bayesian classifier [14], support vector machine (SVM) [15], [16], [41], [54], [58], [59], Neural network [12], decision tree [12], [60] have been applied for the tissue type classification.

In order to improve the classification accuracy, an ensemble of classifiers can be used in the histopathological image analysis. A classifier combiner aggregates the prediction from individual classifiers and reduces the bias of individual classifiers [61]. Adaboost is a popular classifier combiner which combines a set of weak classifiers to make a strong one [62].

In [14], Adaboost is employed to combine a number of weak Bayesian classifiers obtained from different extracted texture features. Kong *et al.* [18] employed a weighted classifier combiner of KNN, Bayesian, and SVM classifiers to classify the tissue regions hierarchically.

2.3.4 Whole Slide HPI Analysis Techniques

The whole slide histopathological image analysis has become an attractive research topic in recent years [14], [17], [18]. The WSI is able to provide global information of a tissue specimen for quantitative image analysis. However, the automated WSI analysis is challenging since it has high computational complexity. Several techniques based on the multi-resolution framework have been proposed. Table 2.1 shows the state-of-the-art literature on the WSI analysis techniques.

TABLE 2.1
RELATED WORKS ON THE WHOLE SLIDE HISTOPATHOLOGY IMAGE ANALYSIS

Tissue Type	Reference	Dataset Info.
Breast	Petushi et al., 2006 [12]	24 H&E stained, 20X
Head and Neck	Mete et al.,2007 [15]	7 H&E stained, 20X
Cervical	Wang et al., 2009 [16]	31 H&E stained, 40X
Neuroblastoma	Sertel et al.,2009 [17]	43 H&E stained, 40X
Neuroblastoma	Kong et al., 2009 [18]	33 H&E stained, 40X
Breast	Roullier et al., 2011 [31]	H&E stained, 20X

Petushi *et al.* [12] employed gray scale conversion, adaptive thresholding and morphological operations to segment the nuclei and identify the high nuclei density regions in the invasive breast carcinoma WSIs. Classification of the tissue type is then performed based on the features extracted from pre-segmented areas using different classifiers. A classification accuracy of 68% has been reported on a database of 24 WSIs.

Mete *et al.* [15] proposed a block-based supervised technique for detection of malignant regions in histopathological head and neck slides. With the pre-defined training subimages (128×128 pixels), this technique first extracts the most prominent colors that are present in the positive and negative training samples. These colors are then clustered into several groups that are used to train the SVM. For malignancy detection in a candidate image, the color information is extracted and is classified by the pre-trained SVM. The technique provides a good performance. However, the performance may suffer from the staining color variations of the WSIs.

Wang *et al.* [16] developed an automated computer-aided technique for the diagnosis of cervical intraepithelial neoplasia. This technique first segments the epithelium using prior knowledge of the tissue distribution. Based on the measurements and features obtained from the squamous epithelium, the SVM is employed to perform the classification. This CAD technique has been reported to achieve 94.25% accuracy for four classes tissue classification on 31 digital whole slides.

Sertel *et al.* [17] developed a multi-scale CAD technique for classification of

stromal development for neuroblastoma. This technique uses texture features extracted using co-occurrence statistics and local binary patterns. A modified K-NN classifier was employed to determine the confidence resolution for the classification. The experimental results showed an overall classification accuracy of 88.4%. Kong *et al.* [18] developed a similar CAD technique for classification of the grades of neuroblastic differentiation. This technique first segments a WSI into multiple cytological components (e.g., nuclei, cytoplasm, RBCs) at each resolution level using an Expectation-maximization approach. The cytological and statistical features derived from the pre-segmented results are then fed to a multi-classifier combiner for the training. The trained classification technique is tested on 33 WSI with 87.88% accuracy.

Roullier *et al.* [31] proposed a multi-resolution graph-based analysis framework for the WSI analysis of breast cancer. The 2-means clustering is applied on the histogram of the regularized image to cluster the region of interest and background. Spatial refinement based on the discrete label regularization are used to achieve accurate segmentation around the boundary. The above steps are repeated at four different resolution images (from lower to higher). Finally, the mitosis are identified in the labeled region of interest with the domain knowledge that the mitosis are visually recognized by the red-cyan color difference.

2.3.5 HPI Analysis for Skin Cancer

Since different tissue types have different specific diagnostic features considered by the pathologists, the techniques mentioned in the Section 2.3.4 cannot necessarily be applied in the skin tissue analysis and diagnosis. A few research studies have been reported on the HPI analysis of skin cancer. Smolle [63] performed a pilot study on digital skin histopathological image analysis. A selective portion of the whole skin tissue slide is first digitized into an image. This image of the skin specimens are then divided into non-overlap blocks of equal size and shape. A set of gray level, color and Haralick texture features [50] are calculated for each image blocks. Finally, based on the extracted features, multidimensional linear discrimi-

nant and hierarchical clustering are applied to classify the images blocks into two classes: normal and malignant.

Smolle *et al.* [64] extended the block-based analysis schema where they applied tissue counter analysis (TCA) to the histologic sections of skin tumor. The basic idea of TCA is to “count" the classified image blocks in a given histological specimen. The histologic specimen is then be labeled as “benign" or “malignant", based on the relative proportion of image blocks that belong to different classes. Experimental results showed that the TCA might be a useful method for the interpretation of melanocytic skin tumors.

The above mentioned skin tissue analysis techniques only reveal the feasibility of texture and color features and TCA for classification of different type of sampled skin area from the whole glass slide. There are several limitations of these skin tissue analysis techniques [63], [64]. First, these techniques only consider the pixel-level features (i.e., texture and color features) of the sampled area. However, the object-level features, e.g., the distribution of melanocytes, are of interest to the pathologist. Second, these techniques may fail when there exists staining variation. Third, these techniques only consider a representative region within the whole glass slide, and therefore the sampling procedure requires user interactions.

2.4 Summary

In this chapter, we presented a brief introduction of the histopathological image, followed by the introduction of the skin histopathological image which is essential for understanding the image appearance. Four main groups of features that correlated to the disease outcome are also discussed. These four groups of features will be the guidelines of the quantitative image analysis. The review on the histopathological image analysis techniques is also provided in terms of different aspects: ROI detection and segmentation, feature extraction, classification, WSI analysis, and HPI analysis for skin cancer.

Chapter 3

The Proposed System

In Chapter 2, we reviewed the state of the art and described the traditional methods used by dermatopathologist to examine the skin tissue. In our research, we propose to develop a CAD system which will help the dermatopathologist in the diagnosis of the skin tissue. In this chapter, we first discuss some of the challenges on the automated analysis of the digital whole slide skin tissue image. An overview of the proposed framework is then presented.

3.1 Challenges

There are several challenges ahead. Three main challenges are discussed as follows.

3.1.1 Staining Variations

One of the difficulty for automated image analysis is the non-uniformity of staining. There are two kind of variations present: intra- and inter-images variations. Fig. 3.1 shows the epidermis area from four different digitized skin images, and include cases of nevus and melanoma. It is observed that although the color of the nuclei are all blue, the degree of blueness vary from one image to another. This is known as the inter-image variation. Another variation is intra-image variation. In Fig. 3.1, the pairs of bright arrows pointed out the intensity variations between nuclei from

the same epidermis area of skin tissue. These two kinds of variations may be due to the non-uninform absorbtion of the staining dye by different tissue components, different staining amount used during the preparation of the tissue slide or other factors, such as stains fading. These variations may hinder consistent inter- and intra-image quantitative analysis of tissue skin samples.

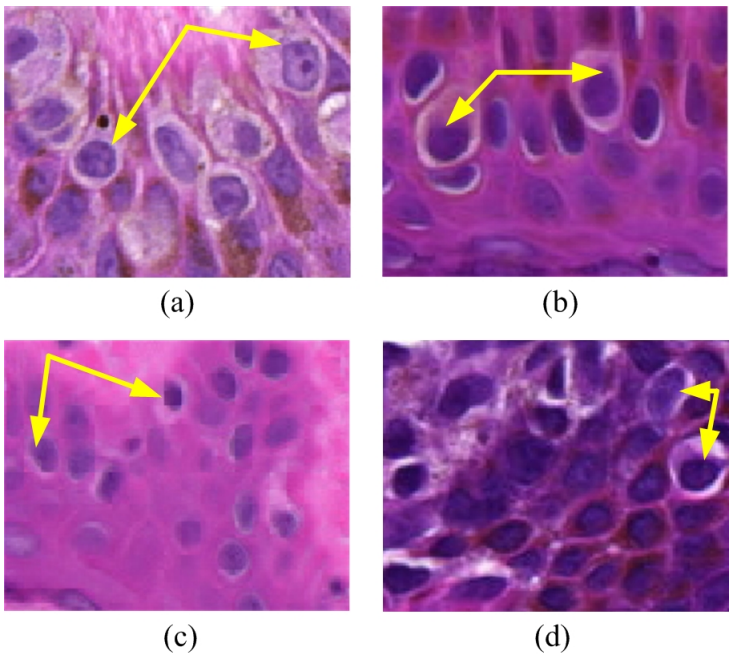

Fig. 3.1. Four examples of skin histopathological images captured on magnification 25X. These four images are sampled from the epidermis area of different skin tissues. Note the non-uniformity of the staining between images. The nuclei pointed by the bright arrows have significant intensity variation.

3.1.2 Computational Effectiveness

Wang *et al.* [16] proposed a CAD system for WSI analysis. It has been reported that the proposed CAD system may need about 3 hours to process one WSI (152,000$\times$ 41,500 pixels). However, the average examination time for one glass tissue slide by an experienced histopathologist is only about 5 minutes or less. The designed CAD system should provide a processing time on the same order to that of the manual examination. This requires us to develop an efficient technique to deal with such large amount data. Note that one virtual slide will take a large amount of storage

and computational power for processing.

3.1.3 Discriminant Features Extraction

Note that there are many sub-types of melanoma and nevus, and there is a high degree of similarity between certain types of melanotic nevus and malignant melanoma. This makes automated discrimination between the melanotic nevus and melanoma very difficult. The robust features which can represent the characteristic of the current tissue class are very important for the effectiveness of the CAD system.

3.2 Overview of the Proposed System

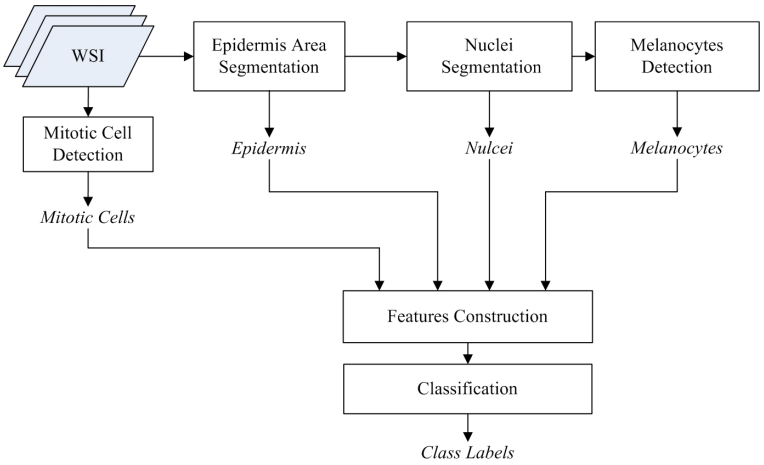

Fig. 3.2. The overall schematic of the proposed CAD system.

The schematic of the proposed system is shown in Fig. 3.2. The proposed system consists of six modules. Given a WSI, the first three cascade modules are used for the segmentation and detection of ROIs. The *epidermis area segmentation* module aims to segment the skin epidermis in the WSI. In order to reduce the processing time and perform the automated image analysis in an efficient way, we perform the segmentation at lower resolution. Once the epidermis area is segmented, the proposed system will then focus on the epidermis area and analyze the image at higher resolution. The *nuclei segmentation* module is applied to segment the ker-

atinocytes. Note that the nuclei are (which also include melanocytes) present in the epidermis area. The *melanocytes detection* module is used to detect the melanocytes from the pre-segmented nuclei. Also, the *mitotic cell detection* module is used to detect the potential mitotic cells in the WSI. Based on the pre-segmented epidermis area, nuclei, melanocytes, and mitotic cells, the *features construction* module will consider the spatial arrangement and morphological characteristics of the pre-segmented ROIs and construct the features according to the diagnostic factors used by pathologists. The last module, i.e., the *classification* module, utilizes the features to classify the tissues into three categories: melanoma, melanocytic nevus, or normal skin.

In the next five chapters, we will present all modules in details. In Chapter 4, we will discuss the epidermis segmentation and analysis. In Chapter 5, an efficient technique for cell nuclei segmentation is presented. In Chapter 6, two proposed melanocytes detection technique are presented. The mitotic cells detection technique is discussed in Chapter 7, followed by the whole slide skin image classification in Chapter 8.

Chapter 4

Segmentation and Analysis of the Epidermis[1]

The overall schematic of the CAD system [25] proposed in this thesis was shown in Fig. 3.2. In this chapter, we present the first module. This is an important step before further analysis is performed.

Unlike other types of specimen, a typical skin tissue slide consists of three main parts: epidermis, dermis and subcutaneous tissues (see Fig. 4.1, the lower image shows the manually labeled contour of the epidermis). The epidermis area is the most important observation area for the diagnosis of a skin tissue. In most cases of melanoma, the grading of the cancer can be made through the architectural and morphological features of atypical cells in the epidermis or epidermis-dermis junctional area. Therefore, segmentation of the epidermis area is an important step before further analysis is performed. Once the epidermis area is segmented, the dermis and sebaceous tissues can then be easily located.

In this chapter, we propose an efficient technique for automatic segmentation and analysis of the epidermis area in the skin WSI.

[1]A version of this chapter has been published. Cheng Lu, Mrinal Mandal. "Automated Segmentation and Analysis of the Epidermis Area in Skin Histopathological Images", *In Proc: The 34th Annual International Conference of the Engineering in Medicine and Biology Society (EMBC 2012)*. 2012, P. 5355-5359.

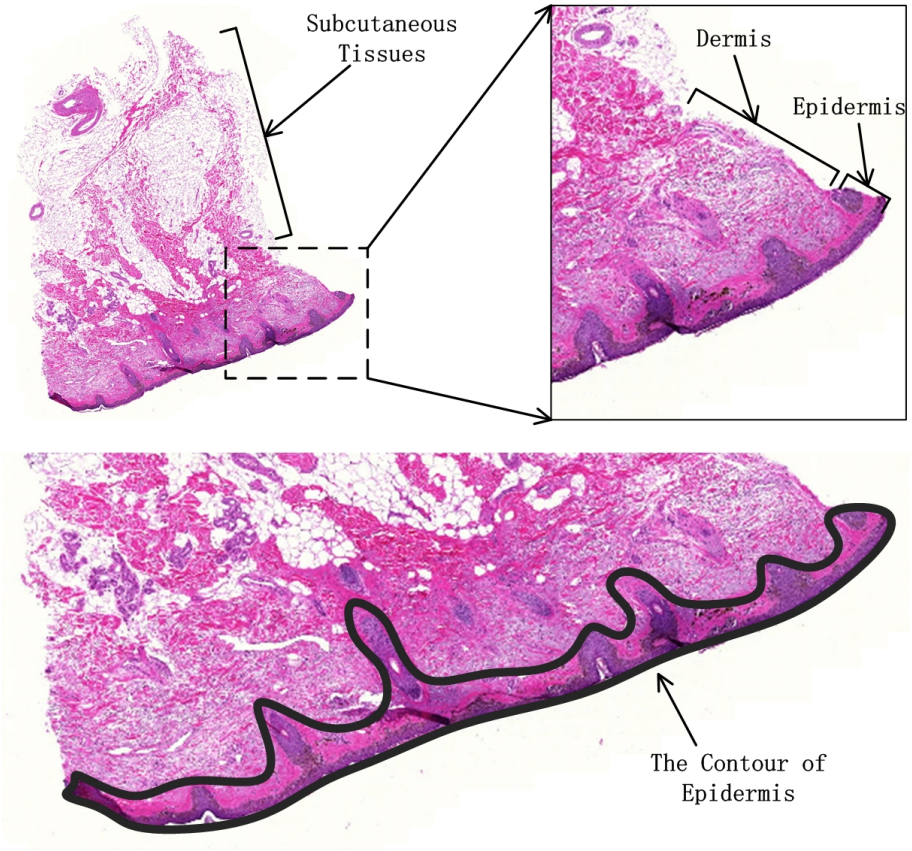

Fig. 4.1. The anatomy of a skin tissue.

4.1 The Proposed Technique

The schematic of the proposed technique is shown in Fig. 4.2. It is observed that there are four modules in the proposed technique. First, a monochromatic color channel which can provide a good discriminant information between the epidermis and dermis areas is determined. The *down sampling* module generates a LR WSI using down sampling method. The *segmentation of epidermis* module segments the LR image using a global threshold and shape analysis. In the last module, the layout of epidermis is determined, and the HR image tiles of epidermis are generated for further analysis. The details of these modules are discussed below.

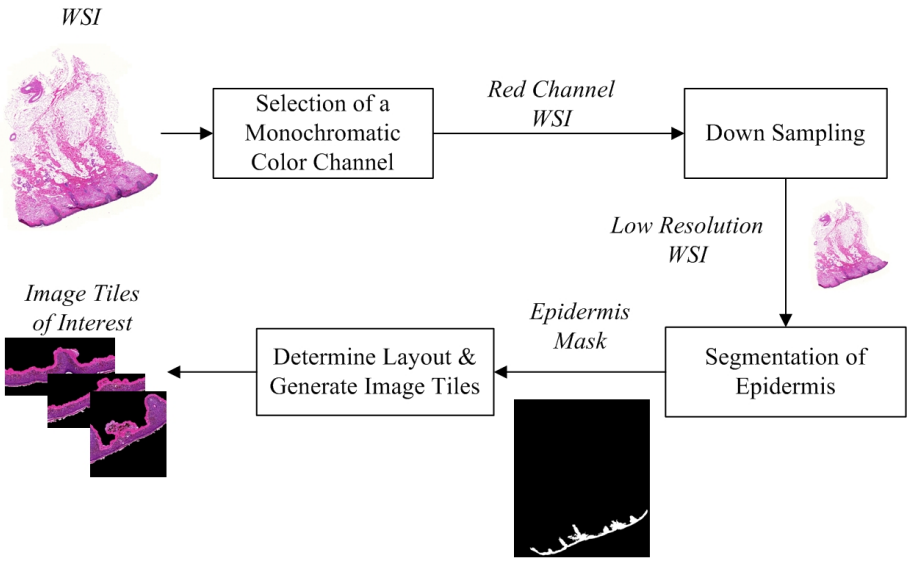

Fig. 4.2. The schematic for the WSI segmentation.

4.1.1 Selection of a Monochromatic Color Channel

In the skin tissue, the epidermis area and the dermis area are closely connected with each other (see Fig. 4.1). In order to segment the epidermis area accurately, we need to first determine a monochrome channel which can provide good distinguishable information between the epidermis and dermis areas. Note that a WSI contains $\{R, G, B\}$ three channels. To obtain a monochrome channel M, a linear transform $A = [a_1, a_2, a_3]$ is required, i.e.,

$$\begin{aligned} M &= a_1 R + a_2 G + a_3 B = [R, G, B][a_1, a_2, a_3]^T, \\ & s.t., \ a_1 + a_2 + a_3 = 1. \end{aligned} \tag{4.1}$$

Denote an image pixel by p and its gray value by $g(p)$. Denote the pixels belonging to epidermis area as class 1 (denoted as Ω_1) and the pixels belonging to the dermis area as class 2 (denoted as Ω_2). Let the mean intensity of the epidermis area, dermis area and dermis + epidermis areas be denoted as μ_1, μ_2, and μ_o respectively.

In this work, to distinguish the different classes, we use the following metric [65]:

$$R_{II} = \frac{\sigma^2_{inter}}{\sigma^2_{intra}} \tag{4.2}$$

where

$$\sigma^2_{inter} = w_1(\mu_1 - \mu_o)^2 + w_2(\mu_2 - \mu_o)^2 \tag{4.3}$$

$$\sigma^2_{intra} = \frac{w_1}{N_1} \sum_{p \in \Omega_1} (g(p) - \mu_1)^2 + \frac{w_2}{N_2} \sum_{p \in \Omega_2} (g(p) - \mu_2)^2 \tag{4.4}$$

where w_1 and w_2 are the size proportion of two classes, i.e., epidermis and dermis, respectively. N_1 and N_2 are the total number of pixels in two classes, respectively. The σ^2_{inter} and σ^2_{intra} are the inter classes and intra class variances of the pixel intensities. In this work, we assume that the monochrome channel with a maximum quality metric R_{II} provides the best discriminant information between the epidermis and dermis area. In particular, we need to find an optimal linear transform A^* which can maximize the quality metric R_{II}, i.e., $A^* = \max_{A \in \Omega_A}(R_{II})$, where Ω_A is the space of linear transform A. In this paper, we use a grid search method to find an approximate optimal linear transform $\tilde{A}$ which is described as follows.

- First, we manually label the epidermis and dermis areas for 8 different skin WSIs as the test data set.
- A set of 1-by-3 vectors which can approximately cover the space of the linear transform A, denoted as $\tilde{\Omega}_A$, is initialized. The grid step for each variable, i.e., a_1, a_2, and a_3, in the linear transform is 0.05.
- For each possible linear transform $A \in \tilde{\Omega}_A$, the quality metric R_{II} is calculated.
- The linear transform A that corresponds to the maximum quality metric R_{II} is recorded as the approximate optimal linear transform $\tilde{A}$.

All the approximate optimal linear transforms $\tilde{A}$ for the 8 test WSIs with corresponding quality metric R_{II} are presented in Table 4.1. The 8 WSIs are labeled as WSI1, WSI2, $\cdots$,and WSI8, respectively.

TABLE 4.1
THE APPROXIMATE OPTIMAL LINEAR TRANSFORM $\tilde{A}$ WITH ITS R_{II} VALUE FOR 8 TEST WSIS.

	WSI1	WSI2	WSI3	WSI4	WSI5	WSI6	WSI7	WSI8
$\tilde{A}$	$[1, 0, 0]$	$[1, 0, 0]$	$[0.9, 0.1, 0]$	$[0.95, 0.05, 0]$	$[0.85, 0.15, 0]$	$[1, 0, 0]$	$[0.9, 0.1, 0]$	$[0.95, 0.05, 0$
R_{II}	0.36	0.53	0.37	0.53	0.53	0.45	0.25	0.24

TABLE 4.2
THE QUALITY METRIC R_{II} FOR THE R, G, B, GRAY, H, S, V CHANNELS OF 8 WSIS.

	WSI1	WSI2	WSI3	WSI4	WSI5	WSI6	WSI7	WSI8
R	**0.36**	**0.53**	**0.34**	**0.51**	**0.49**	**0.45**	**0.22**	**0.23**
G	0.06	0.11	0.25	0.14	0.21	0.22	0.04	0.03
B	0.10	0.21	0.10	0.27	0.20	0.21	0.03	0.01
Gray	0.11	0.20	0.33	0.32	0.33	0.34	0.09	0.07
H	0.03	0.03	0.07	0.22	0.05	0.05	0.05	0.04
S	0.07	0.11	0.26	0.19	0.24	0.23	0.07	0.05
V	0.35	0.50	0.29	0.49	**0.49**	0.41	0.19	0.21

It is observed that the coefficient associated with the red channel, i.e., a_1, is 1 or close to 1 for all the test WSIs. In other words, the red channel of the RGB color image can provide good distinguishable information between the epidermis and dermis area. Based on such observation, in this work, we choose the red channel as the monochrome channel for latter processing since it is ready to be used without further calculation, even though it may not be always the optimal one. This is further validated with results shown in Table 4.2 and Fig. 4.3. Table 4.2 shows the quality metric R_{II} of the R, G, B channels from RGB color model, the gray channel computed using transform $A_{gray} = [0.299, 0.587, 0.114]$, and H, S, V channels from the HSV color model [66] for the 8 test WSIs. It is noted that the R channel achieve the largest quality metric R_{II} compared to the other channels. The V channel from the HSV color model also provides good discriminating information.

Fig. 4.3 provides a visual evaluation example, where the RGB color image with R, G, B, gray, H, S, V channels of the WSI1 skin histopathological image are shown. It is observed that in the red channel and V channel image (shown in Fig. 4.3(b) and (j), respectively), the epidermis area is easily distinguishable from its neighboring

dermis area. The corresponding quantitative results are shown in Table 4.2.

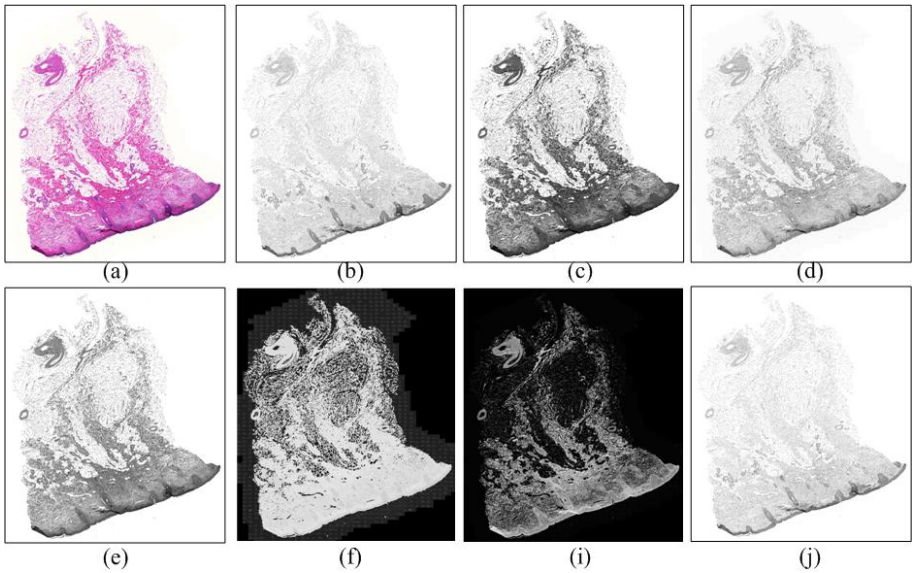

Fig. 4.3. An example of the WSI. (a) Original H&E stained color image. (b), (c), and (d) shows the R, G, and B channel of the image, respectively. (e) shows the gray channel image. (f), (i), (j) shows the H, S, V channels.

4.1.2 Down-sampling

Based on the discussion in Section 4.1.1, given a high resolution WSI I_h with size $r \times c$, we only use the red channel for the latter processing. We employ down-sampling [67] to create a low resolution image I_l with size $(r/k) \times (c/k)$, where k is a down sampling factor. (In order to reduce the aliasing, a low pass filter is usually applied to the image before the down sampling.) In this work we have used k=32, which can reduce a 2.2×10^9 pixel image to a 2.15×10^6 pixels LR image.

4.1.3 Segmentation of Epidermis

As explained in Section 4.1.1, the red channel is chosen for the segmentation. It is observed in Fig. 4.3(b) that the epidermis area has darker intensity value compared to the remaining part of a WSI (see Fig 8.3). Therefore, we can use a simple thresholding method combined with the shape analysis to segment the epidermis area. The thresholding method groups the pixels into two classes: foreground and

background, based on the pixel values. Specifically, let τ be a selected threshold for the segmentation. The classification of pixel p with gray value $g(p)$ is then done as follows:

$$p = \begin{cases} foreground, & if\ g(p) \leq \tau \\ background, & if\ g(p) > \tau \end{cases} \tag{4.5}$$

In our problem, the foreground corresponds to the epidermis area. We apply Otsu's thresholding [68] method to determine the optimal threshold for segmentation.

Before the thresholding, the white background (e.g., the pixels with gray value greater than 240) are removed in order to estimate more accurate result. Three examples of the threshold results on different skin tissues are shown in Fig. 4.4(b), (e), and (h). Note that the epidermis areas are segmented as well as other low intensity components, such as hair follicles, blood vessels and other unrelated tissues. We label all the regions in the binary image via 8-connected criterion [66] and denote all the 8-connected regions as $\{\mathcal{C}_i\}_{i=1...n}$, where n is the total number of the regions. A typical image may result in several hundred candidate regions. A further test is required to eliminate the unrelated false regions.

In order to eliminate the false regions, we use two criteria: area and the shape. We first assume that the epidermis area is greater than a predefined threshold T_{area}. We set $T_{area} = \mathcal{N} \times 0.5\%$, where $\mathcal{N}$ is the total pixel number of the skin tissue, and the fraction 0.5%, determined based on the domain prior and experiment results, represents the portion of the epidermis area in the WSI. Secondly, from the observation, the epidermis area is generally a long and narrow region. This shape feature can be captured by the major axis length (l_1) to minor axis length (l_2) ratio of a best fit ellipse [55].

Given a 8-connected region $\mathcal{C}_i$, we use the above mentioned two criteria based on the domain knowledge to determine if it is epidermis or other tissue components.

$$\mathcal{C}_i = \begin{cases} epidermis, & if\ \ A(\mathcal{C}_i) \geq T_{area}\ \ and\ \ l_1/l_2 \geq T_l \\ others, & otherwise \end{cases} \tag{4.6}$$

where $A(\cdot)$ is the area operator, $A(\mathcal{C}_i)$ represents the area of region $\mathcal{C}_i$. Threshold

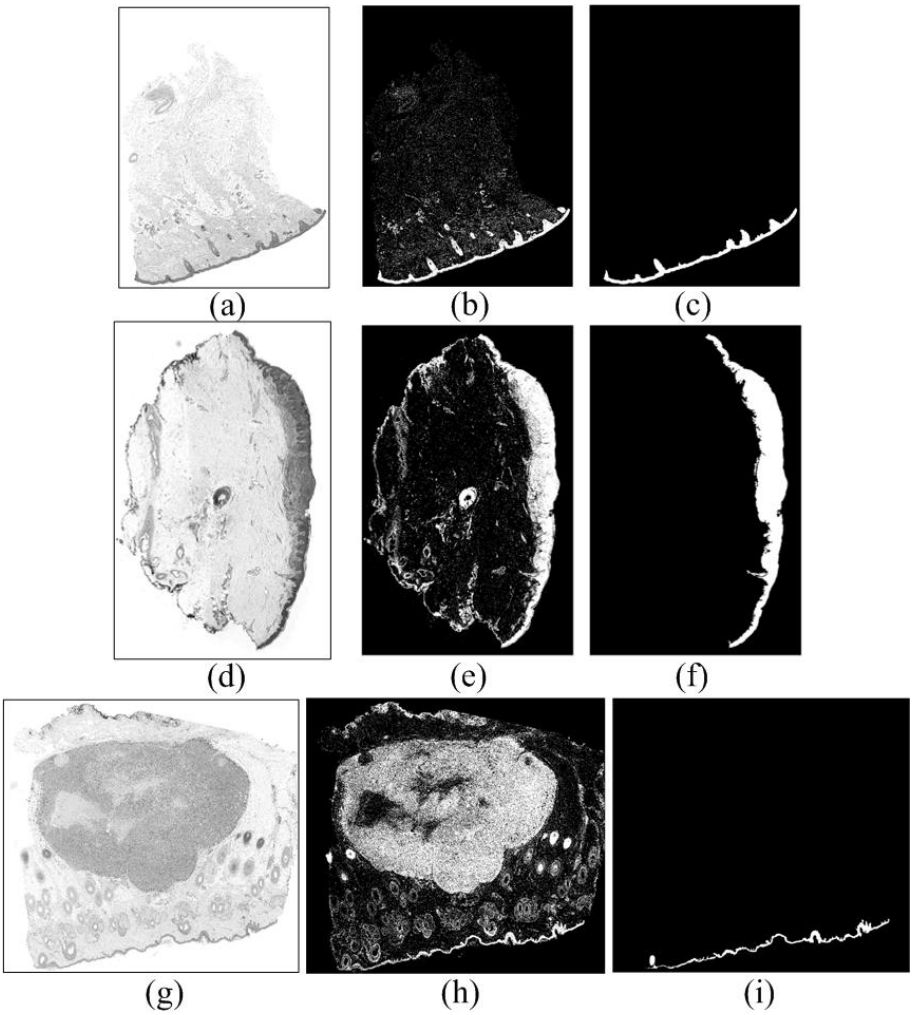

Fig. 4.4. Three examples of epidermis segmentation. (a), (d), and (g) are the original red channel image; (b), (e), and (h) show the results after thresholding; (c), (f), and (i) show the final binary mask for epidermis.

T_l is set to 4 empirically to make sure that the epidermis is long and narrow.

Finally, the holes inside the region are filled to generate the mask for the epidermis. Three examples of the binary masks for the epidermis are shown in Fig. 4.4(c), (f), and (i). Note that the undesirable regions are removed.

4.1.4 Determine Layout and Generate Image Tiles

The epidermis mask is now available for further processing. In this section, we divide the epidermis region into several image tiles. These image tiles will be used for further analysis at high resolution. The reason behind dividing the epidermis is

two-fold:

- Accuracy analysis. The binary mask of the epidermis is obtained from the low resolution image I_l based on the global threshold and shape analysis as the local intensity variants may incur inaccuracy of segmentation results (usually under segmentation). By analyzing the epidermis mask locally, it is expected that we can achieve better segmentation and analysis results.

- Efficient computation. Normally, the epidermis area which taking about 1% to 10% of the whole image. That means about 22 - 220 mega pixels need to be manipulated for a $20mm^2$ tissue, which will take a considerable amount of computational resources. By dividing the rough epidermis mask into image tiles, we can use the parallel computation technique [69] to distribute the processing load into each node which will greatly help to do the computation in an efficient way.

First, we need to divide the whole image into non-overlapping image blocks. A grid G_l which indicates the non-overlap blocks are defined. The grid has the same size as that of the LR image I_l, and the width and height of the block are denoted as b_w and b_h, respectively. We set $b_w = 2000/k$ and $b_h = 1000/k$, remind that k is the down sampling factor for the high resolution image I_h. This grid is overlapped onto the binary image as shown in Fig. 4.5(a). Note that we are only interest in the image blocks which contain the epidermis mask.

In the manual examination of the epidermis, a pathologist usually takes into consider the tissue structure and cytological features vertically across the epidermis. In the computerized image analysis, it is also reasonable to analyze the cytological components vertically across the epidermis. The idea is shown in Fig. 4.6. A horizontal image tile that consists of several blocks is shown in Fig. 4.6(b). In contrast, Fig. 4.6(c) shows an image tile consisting of several blocks generated vertically. It is clear that the image tile obtained vertically in this example preserves all the sub-layer information of the epidermis very well. On the other hand, it is difficult to analyze the image tile shown in Fig. 4.6(b) since it provides only

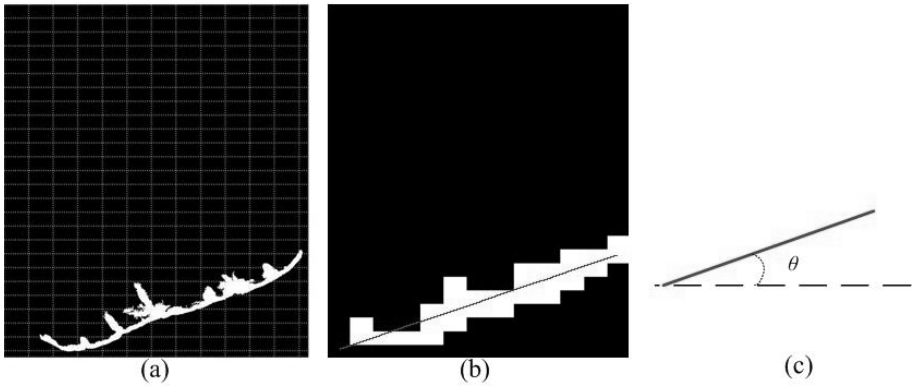

Fig. 4.5. An example for determining the layout of the epidermis. (a) shows the grid on to the binary image; (b) shows the blocks which contains the rough epidermis area (white blocks) as well as the fitted line (red solid line) based on the coordinates of the value 1 in $\mathcal{L}$; (c) illustrates the acute angle θ between the fitted line and the referenced horizontal line.

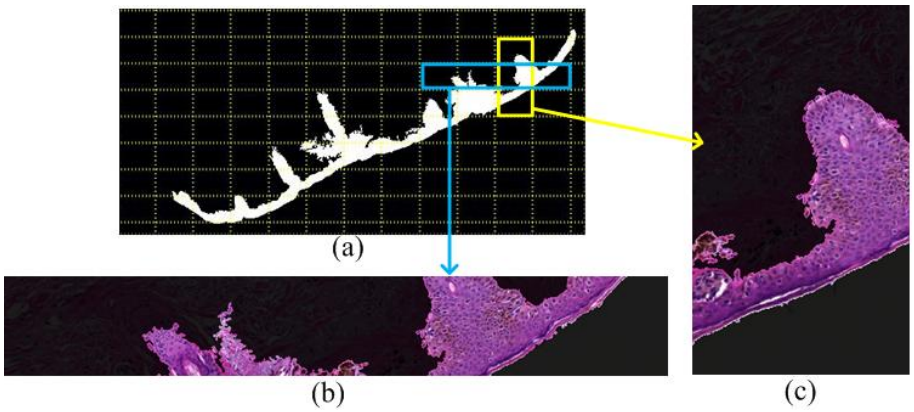

Fig. 4.6. An illustration of the horizontal image tile and vertical image tile. (a) shows the lower portion of Fig. 4.5(a). Note the blue rectangle that points to (c) represents an image tile obtained horizontally whereas the yellow rectangle that points to (c) represents an image tile obtained vertically. The image tile is consisted of several image blocks.

partial information from different location of the epidermis. Since the epidermis in this example is lying horizontally, it is easy to note that generation of the image tile vertically provides intact information rather than generation of the image tile horizontally.

Based on the discussion above, in this work, we propose to generate reasonable image tiles for further analysis. In order to do that, the layout of the epidermis mask should be first determined. Generally, the skin tissues on the glass slides have two different layouts: horizontal or vertical. In order to determine the layout, we

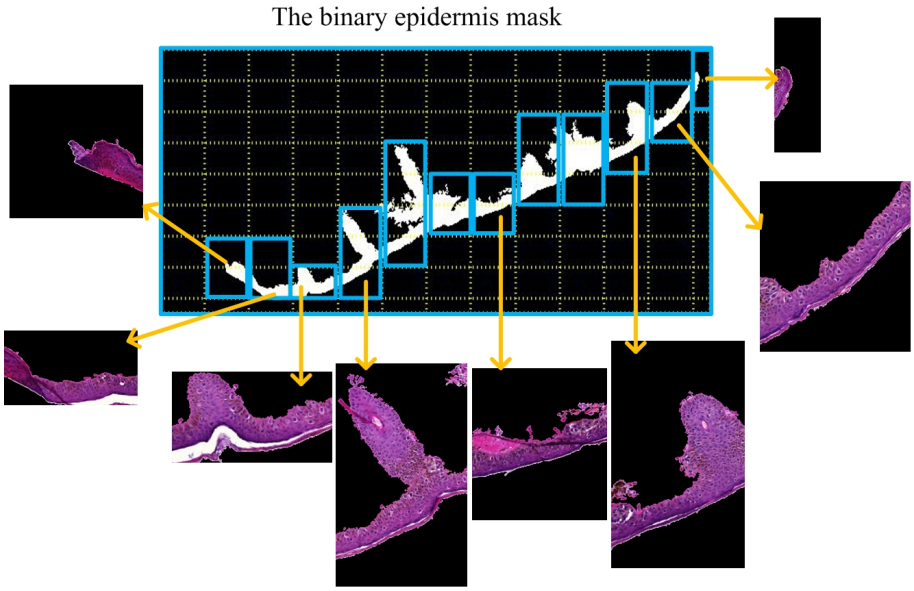

Fig. 4.7. An example of generating the reasonable image tiles. Note the layout of the epidermis is horizontal in this example, so the image tiles are generated vertically. The rectangles indicate the generated image tiles for further processing. Some of the snapshot of the image tiles are present.

calculate a matrix $\mathcal{L}$ as follows:

$$\mathcal{L}(u,v) = \begin{cases} 1, & if \ \sum_{i=(u-1)b_h+1}^{ub_h} \sum_{j=(v-1)b_w+1}^{vb_w} \mathcal{B}(i,j) \geq T_b \\ 0, & if \ \sum_{i=(u-1)b_h+1}^{ub_h} \sum_{j=(v-1)b_w+1}^{vb_w} \mathcal{B}(i,j) < T_b \end{cases} \tag{4.7}$$

where $\mathcal{B}$ is the binary image. u, v and i, j are indices for the 2-D matrix $\mathcal{L}$ and binary image $\mathcal{B}$, respectively. Threshold $T_b = 0.1 \times b_w \times b_h$ considers the noise effect. After calculating the matrix $\mathcal{L}$, we use first order polynomial fitting to determine the fitted line. This is shown in Fig. 4.5(b), where the white blocks correspond to the value 1 in $\mathcal{L}$ while black blocks correspond to the value 0. The solid line across the white blocks is the fitted line based on the coordinates of the value 1 in $\mathcal{L}$. The layout of the epidermis can now be determined by the acute angle θ between the fitted line and the referenced horizontal line which defined as follows:

$$Layout = \begin{cases} horizontal, & if \ 0^\circ \leq \theta \leq 45^\circ \\ vertical, & if \ 45^\circ < \theta \leq 90^\circ \end{cases} \tag{4.8}$$

The idea for determining the layout based on the angle θ is illustrated in Fig. 4.5(c), where the dash line represents the referenced horizontal line.

Based on the layout of the epidermis, we can now generate the image tiles for further analysis. If the layout is vertical, we generate the image tiles by stitching the image blocks with epidermis mask horizontally. On the other hand, if the layout is horizontal, we generate the image tiles by stitching the image blocks with epidermis mask vertically. An example is illustrated in Fig. 8.4. Note that the grid G_l for the LR image should be mapped to the HR image domain in order to generate the HR image tiles.

4.2 Performance Evaluation

We have evaluated the proposed technique on 33 different skin WSIs. These images are captured from different skin tissue samples which contain normal, nevus, and melanoma. These images are captured under 40X magnification on Carl Zeiss MIRAX MIDI Scanning system.

In the evaluation, the manually labeled epidermis areas (pixel-level contour of the epidermis) are treated as the ground truths. We define GT as the ground truth region of the epidermis, SEG as the segmented region obtained by the proposed technique. Three area-based evaluation metrics: sensitivity ($\mathcal{A}_{SEN}$), specificity ($\mathcal{A}_{SPE}$), precision ($\mathcal{A}_{PRE}$) are defined as follows:

$$\mathcal{A}_{SEN} = \frac{|GT \bigcap SEG|}{|GT|} \times 100\% \tag{4.9}$$

$$\mathcal{A}_{SPE} = \frac{|\overline{GT} \bigcap \overline{SEG}|}{|\overline{GT}|} \times 100\% \tag{4.10}$$

$$\mathcal{A}_{PRE} = \frac{|GT \bigcap SEG|}{|SEG|} \times 100\% \tag{4.11}$$

where $|\cdot|$ is the cardinality operator. We also use another evaluation metric:

mean absolute distance (MAD) which is defined as follows:

$$MAD(C^{GT}, C^{SEG}) = \frac{1}{M}\sum_{i=1}^{M}[min||C_i^{GT} - C_j^{SEG}||] \tag{4.12}$$

where C^{GT} and C^{SEG} are the contour of the ground truth region and segmented region, respectively. $||\cdot||$ is the L-1 norm operation. C_i^{GT} and C_j^{SEG} represent the ith pixel and the jth pixel on the contour of the ground truth region and segmented region, respectively. M is the total number of pixels on the contour of the ground truth region.

TABLE 4.3
PERFORMANCE EVALUATION OF THE EPIDERMIS SEGMENTATION.

	$\mathcal{A}_{PRE}$	$\mathcal{A}_{SPE}$	$\mathcal{A}_{SEN}$	MAD (pixels)
Red channel	86.27%	99.25%	99.80%	3.72
V channel	85.92%	98.70%	96.00%	5.99
Gray channel	2.25%	82.69%	33.33%	8754

The performance of the epidermis segmentation technique on the red channel, V channel, and Gray channel images for 33 test WSIs are shown in Table 4.3. It is observed that the proposed technique provides a good performance on both red channel and V channel images since these two channels provide good discriminant information as discussed in Section 4.1.1. The proposed segmentation technique if applied on the gray channel image generates a poor performance because in the gray channel image the epidermis and dermis areas are hard to differentiate by using a threshold. It noted that other monochromatic color channels (discussed in Section 4.1.1) also have poor performance (the results are not shown here).

The average processing time for segment the epidermis area for an image with 2800×3200 pixels is about 2.43 seconds. All experiments were running on a 2.4 GHz Intel Core II Duo CPU with 3GB RAM using MATLAB 7.04.

4.3 Summary

This chapter presents the segmentation and analysis of the WSI. In order to perform an effective segmentation, a monochromatic color channel is first determined. By using the pre-determined monochromatic channel, a hybrid technique based on global threshold and shape analysis is employed to segment the epidermis from the WSI. We also discuss how to generate the HR image tiles of the epidermis for further analysis. Experimental results show that the proposed technique provides a good performance. The proposed technique is an important pre-requisite procedure towards the automated skin histopathological image analysis since the epidermis area is the key area to be examined. Further quantitative analysis, e.g., melanocytes detection in the epidermis, will be carried out based on this work.

Chapter 5

Segmentation of the Cell Nuclei[1]

In Chapter 4, I presented a technique for the segmentation and analysis of the epidermis, which is the first module of the proposed CAD system (see Fig. **??**). The first module generates the high resolution image tiles of interest, i.e., the epidermis area, for further analysis. In this chapter, we focus on the segmentation of the nuclei in the epidermis area. The segmentation of cell nuclei plays an essential role in quantitative histopathological image analysis [49]. The size, color/intensity, distribution, and other cytological features of the cell nuclei provide important diagnosis information. The proposed segmentation technique can also be used for segmentation of lymphocytes and other types of nuclei in histopathological images.

5.1 Introduction

Microscopic analysis of haematoxylin and eosin (H&E) stained section forms the backbone of most diagnoses rendered by anatomical pathologists. Among other parameters, evaluation of cell nuclei plays an important role in the histopathological examination and analysis. Anatomical pathologists, especially cytopathologists, give special attention to parameters like size, shape, contours and presence or ab-

[1]A version of this chapter has been published. Cheng Lu, Muhammad Mahmood, Naresh Jha, Mrinal Mandal. "A Robust Automatic Nuclei Segmentation Technique for Quantitative Histopathological Image Analysis ", *Analytical and Quantitative Cytology and Histopathology*. 2012, P. 296-308.

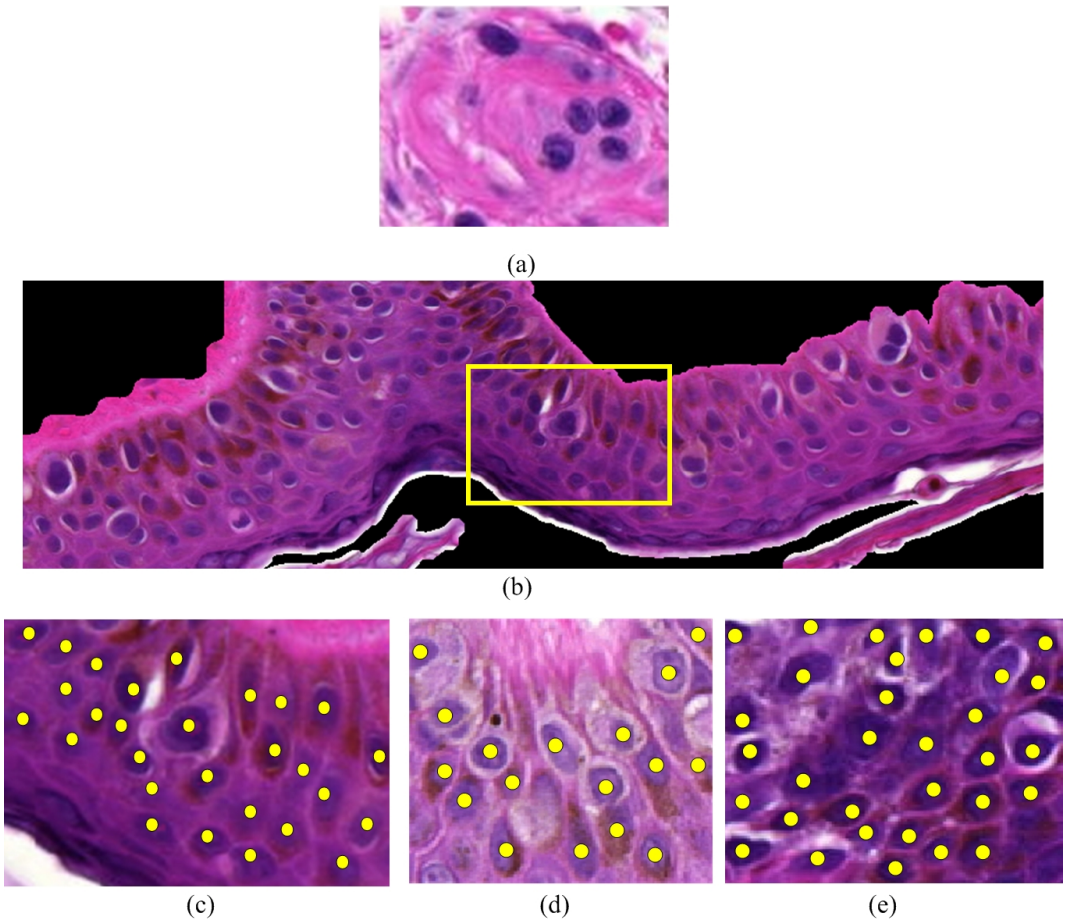

Fig. 5.1. H&E stained histopathological images. (a) A H&E stained histopathological images (captured at 30× magnifications). (b) the image of the epidermis area (captured at 20× magnifications). (c) is an image cropped from the rectangle area of (b). (d) and (e) are two other H&E stained image (captured at 30× magnifications) from the skin epidermis. Note the inter- and intra-image variation of color. The bright dots indicate the location of nuclei.

sence of nucleoli and mitotic figures in nuclei. The morphological features and the distribution of the cell nuclei have great diagnostic value and play a very important role in determining the malignant nature of a lesion. Recently, in the environment of very efficient image based computer models, many computer aided image analysis techniques have been proposed to evaluate and analyze cell nuclei (e.g. karyometric analysis [33]). In these computerized quantitative histopathological image analysis, the segmentation of cell nuclei is the first major step [49], [70]. The accuracy of the automated segmentation technique employed is critical in obtaining good and efficient diagnostic performance.

Traditionally, the histopathological sections for microscopic analysis are primarily stained with H&E. These sections allow anatomical pathologists to assess a wide range of specimens obtained from biopsies and surgical procedures. Further studies (such as special stains, immunohistochemical stains and other ancillary studies) can be employed to augment the diagnoses; however, H&E stained slides still play the most important role in histopathological evaluation. In order to further enhance the microscopic analysis, many computer aided image analysis techniques have been proposed. However, certain obstacles and limitations still exist in achieving a good result. Fig. 5.1(a) shows one example of an H&E stained histopathological image. In this image, the cell nuclei are stained as blue-purple due to haematoxylin, whereas, the cell membranes and cytoplasmic contents are stained as pink since its contents absorb the staining dye eosin. In this image, the nuclei (i.e., foreground) and the cytoplasmic contents (i.e., background) have acceptable discrimination. However, a wide variety of reasons (e.g., tissue fixation, staining method employed, specimen type, etc.) may lead to non-uniform staining variations and complex backgrounds. Intra- and inter-image variations exist and color/intensity values of the foreground and background may appear similar. Fig. 5.1(b)-(e) show examples of H&E stained histopathological images of cutaneous epidermis. In Fig. 5.1(b) non-uniform staining variation exists, i.e., the color/intensity value of cytoplasm around the rectangular area is lower than the other areas. For better visualization, a magnified version of the rectangular region is shown in Fig. 5.1(c). Two

Fig. 5.2. The schematic for the proposed technique.

other images captured from the epidermis are shown in Fig. 5.1(d) and (e). The ground truth nuclei are indicated with bright dots in Fig. 5.1(c)-(e). The presence of staining variations (intra- and inter-image) and similar backgrounds can pose as obstacles for accurate segmentation of the nuclei in histopathological images.

In this chapter, we propose an effective technique for segmentation of nuclei from histopathological images. Our technique tries to overcome limitations and obstacles usually faced in accurate nuclei segmentation and aim to provide superior performance.

5.2 The Proposed Technique

The schematic for the proposed technique is shown in Fig. 5.2. There are two modules. The hybrid gray-scale morphological reconstructions (HGMR) module is used to reduce the undesired intensity variation in the image. Following that, the local region adaptive threshold selection module (LRATS) is next used to segment the nuclei.

5.2.1 Hybrid Gray-scale Morphological Reconstructions

Due to the staining imperfection and variations, the appearance of the nuclei is generally not homogenous. In order to reduce the influence from undesirable variations within the nuclei region, the HGMR is used to enhance the image. The steps of HGMR are described below.

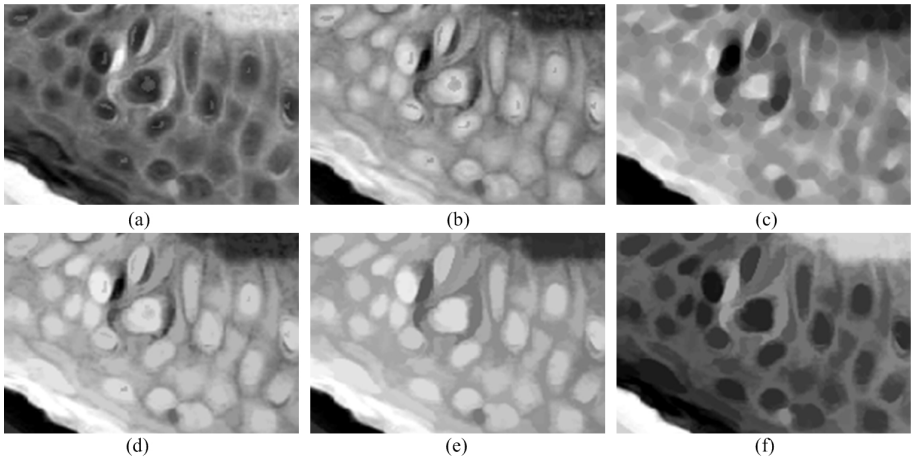

Fig. 5.3. Illustration of the hybrid gray-scale morphological reconstruction. (a) original red channel image. (b) complement of (a). (c) erosion image using $\bar{R}_e = \bar{R} \ominus S$. (d) image after opening-by-reconstruction. (e) image after closing-by-reconstruction. (f) complement of (e).

5.2.1.1 Complement of the Image

Since the nuclei regions appear darker, we first calculate the complement of the image R, assuming an 8-bits image, as follows:

$$\bar{R}(x, y) = 255 - R(x, y) \tag{5.1}$$

where (x, y) is the coordinate.

5.2.1.2 Opening-by-Reconstruction

In order to enhance the nuclei regions, the *opening-by-reconstruction* operation [66] is performed on the image $\bar{R}$ as follows:

$$\bar{R}_{obr} = \mathfrak{R}(\bar{R}_e, \bar{R}) \tag{5.2}$$

where $\mathfrak{R}$ is the morphological reconstruction operator [66], $\bar{R}_e = \bar{R} \ominus S$ ($\ominus$ is the erosion operator), and S is the structure element. We define the structure element as blob-like elements mainly because the nuclei regions have blob-like shape. The radius of the element is empirically set to 3 pixels for the 30X magnification image. As a result, the structure element S is a 7×7 rectangular function with tapered

corners. This is expressed as follows:

$$S = \begin{bmatrix} 0 & 0 & 1 & 1 & 1 & 0 & 0 \\ 0 & 1 & 1 & 1 & 1 & 1 & 0 \\ 1 & 1 & 1 & 1 & 1 & 1 & 1 \\ 1 & 1 & 1 & 1 & 1 & 1 & 1 \\ 1 & 1 & 1 & 1 & 1 & 1 & 1 \\ 0 & 1 & 1 & 1 & 1 & 1 & 0 \\ 0 & 0 & 1 & 1 & 1 & 0 & 0 \end{bmatrix}. \tag{5.3}$$

5.2.1.3 Closing-by-Reconstruction

In order to reduce the noise further, the closing-by-reconstruction is performed on $\bar{R}_{rbo}$ as follows:

$$\bar{R}_{obrcbr} = 255 - \mathfrak{R}(R_{obr} \ominus S, R_{obr}) \tag{5.4}$$

where $R_{obr} = 255 - \bar{R}_{obr}$.

5.2.1.4 Complement of the Image

This step calculates the complement of $\bar{R}_{obrcbr}$ in order to map the image into the original intensity space, i.e., $R'(x, y) = 255 - \bar{R}_{obrcbr}(x, y)$.

Fig. 5.3 presented the intermediate results obtained by the HGMR module of the proposed technique. Fig. 5.3(a) is an original H&E stained image contains several nuclei. Fig. 5.3(b) shows the complement image of Fig. 5.3(a). The eroded image obtained by applying erosion on Fig. 5.3(b) is shown in Fig. 5.3(c). The result of the *open-by-reconstruction* is shown in Fig. 5.3(d). Comparing Fig. 5.3(d) and Fig. 5.3(b), the nuclei regions have been enhanced. The result of the *closing-by-reconstruction* is shown in Fig. 5.3(e). It shows the intensity within the nuclei regions is more homogenous compared to that in Fig. 5.3(d). By comparing Fig. 5.3(a) and Fig. 5.3(f), it is observed that the HGMR is able to make the nuclei regions more homogenous for the subsequent nuclei segmentation operations.

5.2.2 Segmentation of the nuclei using LRATS

Following HGMR, segmentation of nuclei is performed using the local region adaptive threshold selection (LRATS) module. The two steps involved are described as follows.

5.2.2.1 Initial Segmentation

We apply adaptive thresholding [66] for the initial segmentation of the image R'. We first divide the image into several small non-overlapping blocks. The mean intensity of each block is chosen as the local threshold (T_{Local}) for the segmentation. Assuming that the intensity of nuclei regions is lower than the background, we segment the image R' into foreground (represented by 1) and background (represented by 0) and obtain a binary image R^b as follows:

$$R^b(x,y) = \begin{cases} 1, & if\ R'(x,y) \leq T_{Local} \\ 0, & otherwise \end{cases} \tag{5.5}$$

By labeling the 8-connected component in the binary image R^b, we have the initial nuclei regions, denoted by $\{H_q\}_{q=1...n}$, where n is the number of potential nuclei regions. However, one potential problem identified is the presence of under-segmented regions mainly due to the local intensity variations. The under-segmentation problem is resolved by using a finer segmentation module explained in the next section.

5.2.2.2 Finer Segmentation for Local Regions

In order to decompose the under-segmented regions, we incorporate two domain specific knowledge: 1) the nuclei are elliptical shape objects; 2) the size of the nuclei region is within a predefined range [A_{min}, A_{max}]. The predefined range is determined from one pre-labeled image. We label a region as an abnormally large region (ALR), H_r, if its area $A(H_r)$ is greater than A_{max}. An ALR is considered as an under-segmented region and is further divided into sub-regions by minimizing a

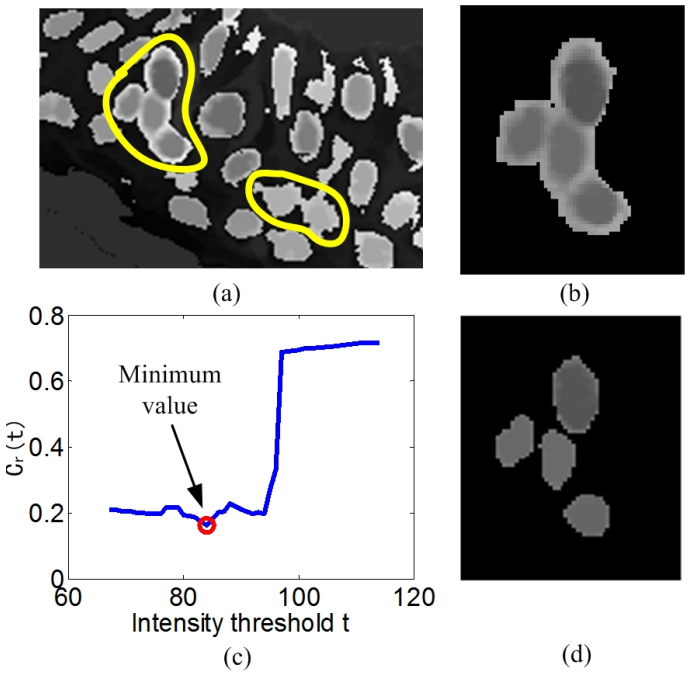

Fig. 5.4. Segmentation of nuclei using LRATS. (a) the initial segmentation image corresponding to Fig. 5.3(f). (b) is a magnified ALR from (a). (c) is the plot of the cost function. (d) is the subregions segmented by the optimal threshold τ_r.

cost function. This is achieved as follows.

(i) The dynamic range of the gray value in the ALR is first determined by assessing the highest and the lowest gray value of the ALR, and the dynamic range be denoted as $[D_l, D_u]$.

(ii) Select a threshold $t = D_u - j - 1$, where j is the iteration number. Based on the threshold t, the ALR is segmented and the corresponding binary image B_t is obtained as follows:

$$B_t(x,y) = \begin{cases} 1, & if\ g(x,y) < t \\ 0, & if\ g(x,y) \geq t \end{cases} \tag{5.6}$$

where $g(x,y)$ is the gray value of the ALR.

(iii) Assume that the binary image B_t includes K disconnected regions, denoted by $L_k, 1 \leq k \leq K$. The point set of a region L_k and the point set of the corresponding best fitted ellipse is denoted by $\mathcal{S}(L_k)$ and $\mathcal{E}(L_k)$, respectively. The ellipticity

penalty parameter Φ_E for region L_k is calculated as follows:

$$\Phi_E(L_k) = \frac{|\mathcal{S}(L_k) \triangle \mathcal{E}(L_k)|}{|\mathcal{E}(L_k)|} \tag{5.7}$$

where $\triangle$ is the symmetric difference between two sets, $|\cdot|$ is the cardinality of a point set. The best fitted ellipse for a region L_k is computed using the direct least square fitting algorithm [55]. Note that $\Phi_E(L_k) = 0$ if region L_k is an ideal ellipse.

For region L_k with area $A(L_k)$, the area penalty parameter Φ_A is calculated as follows:

$$\Phi_A(L_k) = \begin{cases} 0, & if\ A_{min} \leq A(L_k) \leq A_{max} \\ \frac{A_{min} - A(L_k)}{0.5(A_{min} + A_{max})}, & if\ \ 0 < A(L_k) < A_{min} \\ \frac{A(L_k) - A_{max}}{0.5(A_{min} + A_{max})}, & if\ \ A(L_k) > A_{max}. \end{cases} \tag{5.8}$$

The penalty parameters Φ_E and Φ_A correspond to the two domain specific knowledge, i.e., the shape and the size of nucleus.

(iv) After calculating the two penalty parameters Φ_E and Φ_A for all K disconnected regions in the binary image B_t, a cost function $C_r(t)$ is calculated for the current threshold t as follows:

$$C_r(t) = \frac{1}{K} \sum_{k=1}^{K} [\Phi_E(L_k) + \Phi_A(L_k)] \tag{5.9}$$

Intuitively, the cost function $C_r(t)$ is the accumulated penalty for all the K disconnected regions $\{L_k\}_{k=1...K}$ at threshold t for ALR H_r. If the segmented regions are close to the elliptical shapes and the segmented areas are within the predefined range [A_{min}, A_{max}], $C_r(t)$ will have a small value.

(v) For each possible threshold $t \in [D_l, D_u]$, we repeat the steps (ii) to (iv) to calculate the cost function $C_r(t)$.

(vi) Determine the optimal threshold τ_r for the ALR H_r by minimizing the cost function $C_r(t)$:

$$\tau_r = \arg_t \min[C_r(t)],\ t \in [D_l, D_u] \tag{5.10}$$

The B_{τ_r} is the segmented result corresponding to the optimal threshold τ_r. For each ALR, the optimal threshold τ_r is determined to decompose the ALR into subregions.

Finally, the morphological opening based on blob-like structure is performed to remove tiny objects that are unlikely to be nuclei and smooth out all the regions.

Fig. 5.4 presented the intermediate results obtained by the LRATS module of the proposed technique. Fig. 5.4(a) shows the segmented image obtained by applying initial segmentation on the image in Fig. 5.3(f). For better visualization, we superimpose the original image onto the binary image. The results show that most of the nuclei are segmented correctly. However, due to the local intensity variation, there are a few under-segmented regions (highlighted by the solid bright contours in Fig. 5.4(a)). Fig. 5.4(b) shows an ALR from Fig. 5.4(a) where under-segmentation is present. Fig. 5.4(c) is the cost function value computed using Eq. B-4. The minimum value is pointed out with an arrow. The optimal threshold is $\tau_r = 84$. Fig. 5.4(d) shows the subregions $\{L_{k,r}\}_{k=1...4}$ corresponding to the optimal threshold τ_r. It is observed that the cost function value is significantly decreased when the intensity threshold is $t \approx 95$. When the threshold is $t \approx 95$, the ALR broken into many sub-regions and the corresponding area penalty parameter is equal to zero. As a result, the value of the cost function are only determined by the ellipticity penalty parameter. The final result of the nuclei segmentation corresponding to Fig. 5.4(a) is shown in Fig. 5.7(e).

Three examples of the final results obtained by the proposed technique are shown in Fig. 5.5. The first row shows three original H&E stained images whereas the second row shows the corresponding segmentation results (the white regions indicate the nuclei regions and the dots indicate the manually labeled nuclei locations). It shows that most of the nuclei regions are recovered by the proposed technique and only a few nuclei regions are missed in images where significant intensity variations are present.

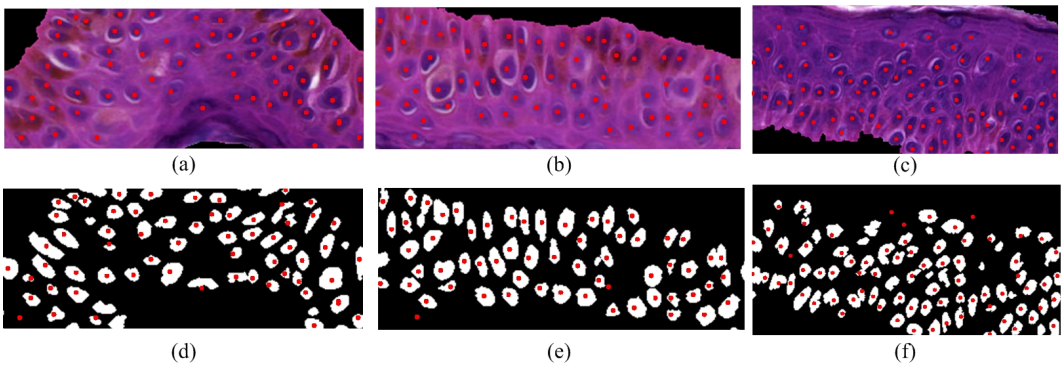

Fig. 5.5. Final results obtained by the proposed technique. (a), (b), and (c) show the original H&E stained images (original magnification at 30×, the images are shrink in order to fit the chapter). The manually labeled nuclei locations are shown as red dots on the image. (d), (e), and (f) show the final segmentation results (binary images where the white regions indicate the nuclei regions) corresponding to (a), (b), and (c), respectively. The manually labeled nuclei locations are also shown on the images for comparison purpose.

5.3 Performance Evaluation

5.3.1 Image Data

In this study, we used a set of 30 different cutaneous histopathological images. The images are of the entire thickness of epidermis with image having a size of 512×512 pixels. In these images, the background and foreground are similar in terms of the color/intensity, however, some staining variations can be observed. The histological sections used for image acquisition are prepared from formalin-fixed paraffin-embedded tissue blocks of skin biopsies. The sections prepared are about 4μm thick each and are stained with H&E using automated stainer. The skin biopsies used contained normal skin, melanocytic nevi, and melanomas. These digital images were captured under 30X magnification on Carl Zeiss MIRAX MIDI Scanning system (Carl Zeiss Inc., Germany).

5.3.2 Manual Identification of the Nuclei

In order to evaluate the performance provided by this new technique, the locations of nuclei and the boundaries of nuclei are manually labeled with the help of an inter-

active computer program (developed using MATLAB 7.1, MathWorks Inc., Natick, MA). In the nuclei location manual labeling procedure, a marker that indicates one nucleus are recorded by the user mouse clicking operation in the computer program. Three examples of the markers with the images are shown in Fig. 5.1(b)-(e), where the bright dots indicate the manually labeled markers for the presence of nuclei. These manually identified locations are treated as the reference for the nuclei detection performance evaluation. In total, there are 3381 manually marked nuclei in 30 test images.

In the manual nuclei boundary labeling procedure, the contour of a nucleus representing the boundary is recorded by the user mouse clicking operation in the computer program. Two examples of the nuclei contours with the images are shown in Fig. 5.6(d), where the dotted contours indicate the manually labeled boundaries for the presence of nuclei. These manually identified boundaries are treated as the reference for the nuclei segmentation performance evaluation. Since it is time-consuming and tedious to label the boundaries for all 3381 nuclei, 110 randomly selected nuclei boundaries are labeled and will be used in the nuclei segmentation performance evaluation.

5.3.3 Evaluation Metrics

The main objective of the evaluation is to determine if the segmented regions obtained by the proposed technique are consistent with the manually labeled ones. The nuclei segmentation results are provided with a binary image, where white regions indicate the nuclei regions. We perform two kinds of evaluations: the nuclei detection evaluation and nuclei segmentation evaluation.

5.3.3.1 Detection Performance Metrics

For the detection performance evaluation, we calculate the centroid of each segmented region obtained by the technique. A segmented nuclei region is counted as correctly detected if its centroid is localized within a range of 5 pixels of the

manually labeled nucleus location.

We define N_{ML} as the total number of manual labeled nuclei locations, N_{DO} as the total number of detected nuclei, N_{TP} as the number of true-positives, (i.e., correctly detected objects compared to the manually labeled nuclei locations), N_{FP} as the number of false-positives. (i.e., falsely detected objects compared to the manual labeled nuclei locations), and N_{US} as the number of nuclei that are under-segmented.

The performance is evaluated with respect to the precision (PRE), sensitivity (SEN), and under-segmentation rate (USR) which are defined as follows:

$$PRE = \frac{N_{TP}}{N_{DO}} \times 100\% \tag{5.11}$$

$$SEN = \frac{N_{TP}}{N_{ML}} \times 100\% \tag{5.12}$$

$$USR = \frac{N_{US}}{N_{TP}} \times 100\% \tag{5.13}$$

The evaluation metric USR indicates cases where multiple nuclei are clubbed into a large region and result in degrade segmentation performance. A small USR value indicates less under-segmentation in the result, which is a desirable outcome.

5.3.3.2 Segmentation Performance Metrics

For the segmentation performance evaluation, we compare the area, perimeter, and form factor of the nuclei obtained by the automatic technique and the manually labeled ones using the Bland-Altman plot [71], [72]. The form factor is defined as follows:

$$F = \frac{4\pi A}{P^2} \tag{5.14}$$

where A and P represent the area and the perimeter of a nucleus, respectively.

The Bland-Altman plot is widely used in comparing two measurements in terms of the agreement. In the Bland-Altman plot, the x-axis shows the average values of the two measurements, whereas the y-axis shows the difference of the two measurements. Mathematically, given a sample S, and its two measurements $\tilde{S}_1$ and $\tilde{S}_2$, we

have a data point in the Bland-Altman plot which defined as follows:

$$S(x,y) = \left(\frac{\tilde{S}_1 + \tilde{S}_2}{2}, (\tilde{S}_1 - \tilde{S}_2) \right). \tag{5.15}$$

In our evaluation, we set the limits of agreement as the bias(mean)$\pm$1.96 standard deviation of the difference between two measurements.

5.3.3.3 Implementation and Parameters Setting

The HTWS technique first employs the *top-hat by reconstruction* operation to reduce the background signal in the image. The hysteresis threshold method is then used to perform the segmentation. The hysteresis threshold method uses two thresholds in order to avoid the disconnected segmentation results where local variations are present. In the end, the watershed method [35] is used to reduce the under-segmentation. For the HTWS technique, we first evaluate the performance using only the hysteresis technique (HT). We then evaluate the whole HTWS technique which uses the watershed method after the HT.

In the HT, the upper and lower (gray value) thresholds are set to 100 and 80 respectively. In the evaluation, we apply the watershed method on the ALR selected by a predefined area threshold. In the GT technique, the global threshold is set to $0.3 \times G_H$ where G_H is the highest gray value in the image. The AT technique computes the local threshold for each non-overlap block in the whole image using the mean intensity value. In the AT technique, the window size is set to 40 $\times$ 40 pixels. For all the compared techniques, we selected the parameters such that the best segmentation result is achieved. For our proposed technique, the window size for the initial segmentation is set to 40 $\times$ 40 pixels and the range of size of the nuclei regions is set to $A_{min} = 100$ and $A_{max} = 500$.

5.3.4 Compare LRATS with Watershed

We compare the segmentation performance of the LRATS module of our proposed technique and the widely used watershed segmentation method for nuclei segmen-

tation [32]. Fig. 5.6 shows an example for the performance comparison. An original red channel image is shown in the Fig. 5.6(a). Following the initial segmentation by using a threshold, we obtain the binary segmented image shown in Fig. 5.6(b). Due to the complex background, the initial segmentation result includes some background regions that have low intensity value. We are primarily concerned about the ALR that is shown in Fig. 5.6(c). In Fig. 5.6(d), the red channel image (after HGMR) is super imposed onto the binary image for better visualization. In this ALR, two nuclei regions exist and they are indicated by the two dotted contours. The pixels outside the two dotted contours belong to the background. If we apply the watershed method on this ALR, we obtain an over segmentation result as shown in Fig. 5.6(e). In the watershed method, the local regional minimums are first determined as the basins for the segmentation [66]. The incorrect number of local regional minimums will lead to the over segmentation. However, even though we know the exact number and the location of the nuclei in this ALR, we still obtain inaccurate result. This is illustrated in Fig. 5.6(f). Fig. 5.6(f) presents the result obtained using the marker-control watershed method, where the markers for the two nuclei are specified by human interaction. Note that the number of the segmented regions is correct, i.e., two segmented regions are obtained from the original ALR. However, in each region, there still exists the background region that does not belong to the nucleus. On the other hand, the segmented regions obtained by the proposed LRATS are accurate and do not contain redundant regions that belong to the background (see Fig. 5.6(g)). This illustrates the effectiveness of the proposed LRATS compared to the watershed method.

5.3.4.1 Detection Performance Comparison

The detection performance comparison of the threshold-based techniques is shown in Table 5.1 (using the evaluation metrics introduced in Section 5.3.3). It shows that the HT technique results in a high *USR* (about 49%). This is mainly due to local cell clustering in epidermis with intensity variations. In order to reduce the under-segmentation, the watershed method is applied on the ALR in the HTWS

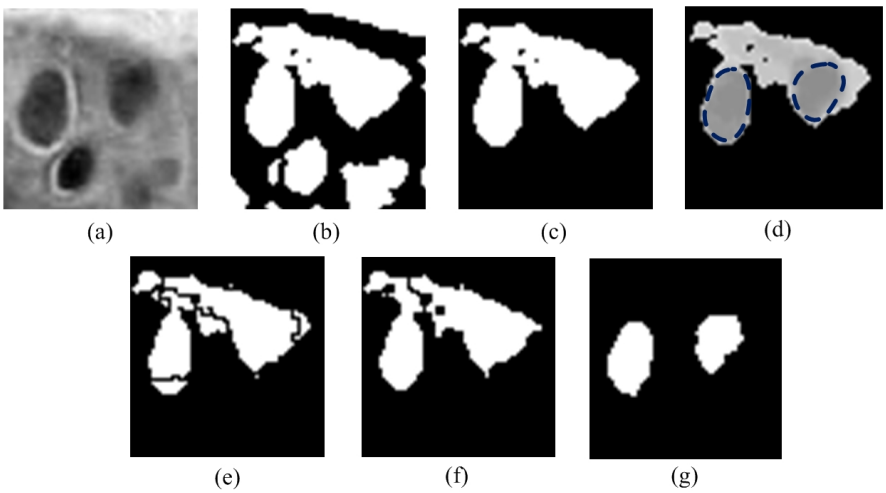

Fig. 5.6. Segmentation performance of the LRATS and watershed techniques. (a) the original image. (b) the binary image after threshold. (c) the ALR. (d) the red channel image (after HGMR) super imposed onto the binary image. (e) the segmentation result after applying the watershed. (f) the segmentation result after applying the marker-control watershed. (g) the segmentation result after applied the LRATS. Note that the dotted contours in (d) indicate the reference nuclei boundaries.

technique. The corresponding performance is shown in the third row of Table 5.1. *USR* of the HTWS is reduced to 9.85%. However, due to the intensity variation, the watershed method leads to over segmentation and the *PRE* is very low (25.98%).

In the case of GT, as it uses a single threshold it misses most of the nuclei regions that have higher intensity values. This results in a very low SEN (48.98%). The AT technique uses local thresholds to perform the nuclei segmentation and achieves better SEN than the HT, HTWS and GT techniques. However, it still cannot separate the clustered nuclei regions which results in high USR at 35.11%. The VT technique calculates a smooth threshold surface that encourages the intersection with the image surface at the edge. The VT technique provides high SEN (87.31%) and relatively low USR (14.74%). However, it leads to low PRE (66.17%), which is mainly due to the complex background. Our proposed technique achieves the lowest *USR* (5%), which reflects the effectiveness of the LRATS module for segmenting the ALR. Also, our proposed technique has the highest SEN (about 88%) and a high *PRE* (about 80%) compared to other techniques.

Fig. 5.7 illustrates the subjective performance comparison of the nuclei segmentation techniques. In the subjective performance comparison, the segmenta-

TABLE 5.1
PERFORMANCE EVALUATIONS OF THE PROPOSED TECHNIQUE WITH OTHER EXISTING TECHNIQUES ON SKIN EPIDERMIS IMAGES.

Techniques	N_{ML}	$PRE(\%)$	$SEN(\%)$	$USR(\%)$
HT [32]	3381	71.00	69.30	49.04
HTWS [32]	3381	25.98	71.16	9.85
GT [33]	3381	84.66	48.98	22.28
AT [12]	3381	80.34	80.12	35.11
VT [73]	3381	66.17	87.31	14.74
Proposed	**3381**	**80.02**	**88.11**	**5.34**

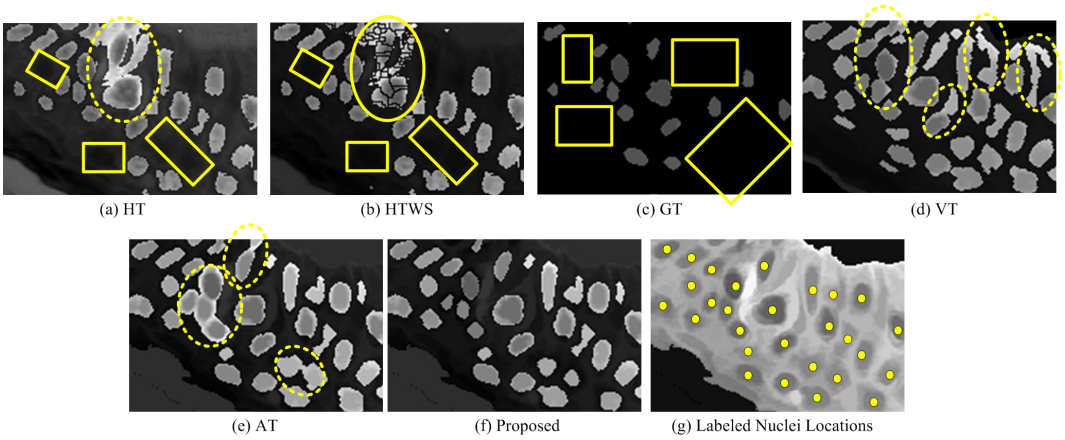

Fig. 5.7. Performance comparison of the nuclei segmentation techniques. The segmentation results are shown as brighter regions in each image. The bright dots in (g) indicate the manually labeled nuclei locations. The under-segmentation is indicated by the dotted ellipse whereas the miss detection of nuclei are indicated by the solid rectangles.

tion results (shown as brighter regions) are compared to the manually labeled nuclei locations. A segmentation result that provides intact nuclei regions and less under-segmentation regions is desired. The original image is shown in Fig. 5.1(b). The segmentation results obtained by the HT [32], HTWS [32], GT [33], VT [73], AT [12] and our proposed technique are shown in Fig. 5.7(a)-(f), respectively. The red channel image is super imposed onto the segmentation result for better visualization.

The HT technique produces under-segmentation that is indicated by the dotted ellipse in Fig. 5.7(a). Also, some of the nuclei are not detected by the HT technique (e.g., in the regions indicated by the solid rectangles). In the HTWS technique,

the watershed method is applied to the ALR that is indicated by the dotted ellipse in Fig. 5.7(a). The corresponding result is shown in Fig. 5.7(b). It is clear that the region is breaking into several small regions that lead to over segmentation. In Fig. 5.7(c), the GT technique misses many of the nuclei regions (indicated by the solid rectangles). The main reason appears to be that GT technique considers only one global threshold and the nuclei regions that have higher intensity are missed. In Fig. 5.7(d), the result obtained by the VT technique includes many background regions due to the complex background (indicated by the dotted ellipses in Fig. 5.7(d)). The AT technique uses different thresholds depending on local characteristics and appears to provide a better performance. However, under-segmentation still exists (shown in the three dotted ellipses in Fig. 5.7(e)). It appears that our proposed technique reduces the under-segmentation successfully while keeping all the nuclei segmented (shown in Fig. 5.7(f)).

5.3.4.2 Segmentation Performance Comparison

In this subsection, we present the segmentation performance of the automatic techniques and compare it with the manually labeled nuclei regions using the Bland-Altman plot. The automatic techniques includes the existing techniques for nuclei segmentation (i.e., the HTWS, GT, and AT technique) and the proposed technique. The automatic segmented nuclei measurements obtained by the automatic techniques compared to the manually labeled ones in terms of the area, perimeter, and the form factor are shown in Fig. 5.8, Fig. 5.9, and Fig. 5.10, respectively. These results show that the measurements of the automatic segmented nuclei obtained by the proposed technique are more consistent with the manually labeled ones (with smaller mean values and standard derivation (SD) compared to that of other existing techniques).

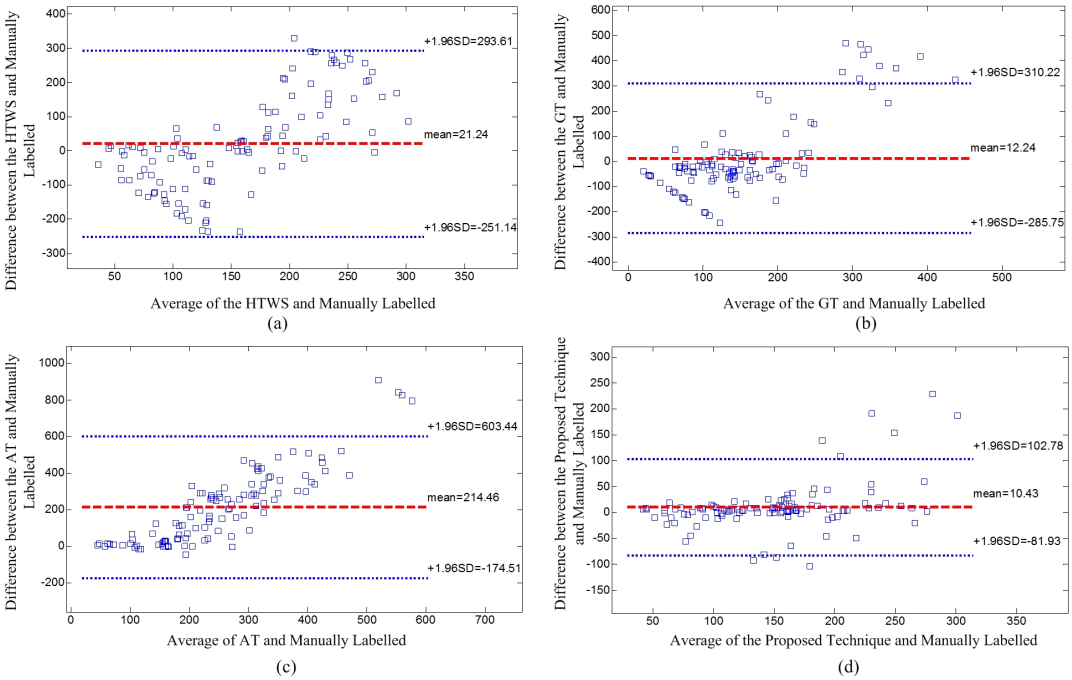

Fig. 5.8. Segmentation performance comparison of the nuclei segmentation techniques in terms of nucleus area. (a) Bland-Altman plot of 110 nuclei areas obtained by the HTWS and the manually labeled ones. (b) Bland-Altman plot of 110 nuclei areas obtained by the GT and the manually labeled ones. (c) Bland-Altman plot of 110 nuclei areas obtained by the AT and the manually labeled one. (d) Bland-Altman plot of 110 nuclei areas obtained by the proposed technique and the manually labeled ones. The mean of the difference is shown as the thick dash line whereas the limits of agreement (mean $\pm$ 1.96 SD of difference) are shown as the dotted lines.

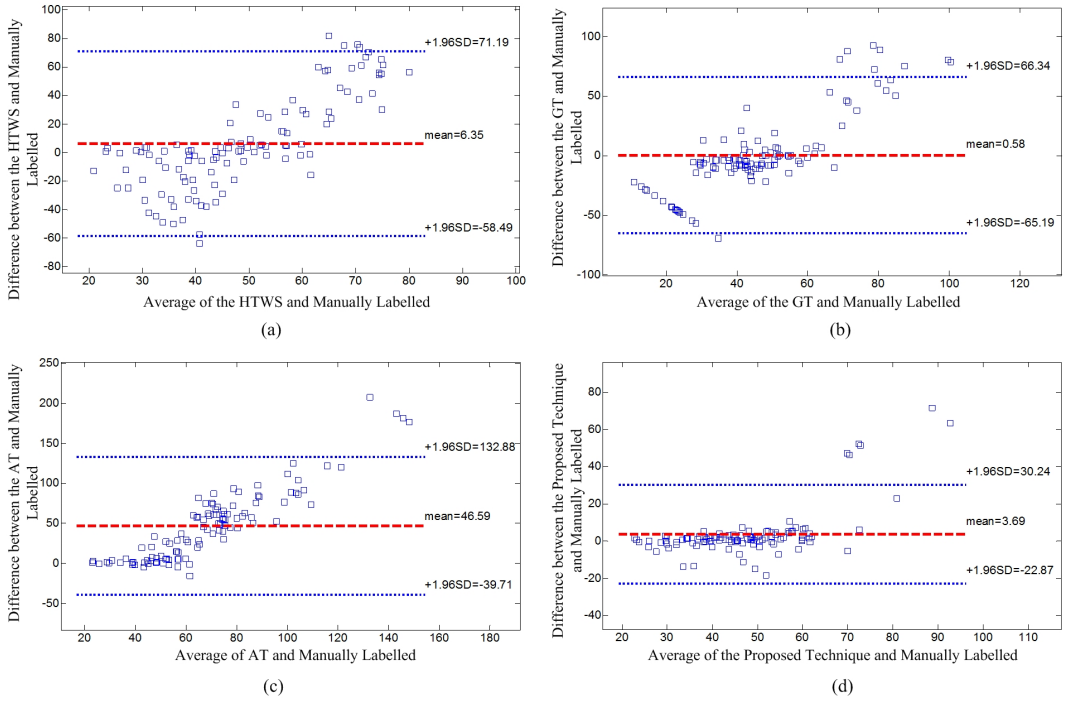

Fig. 5.9. Segmentation performance comparison of the nuclei segmentation techniques in terms of nucleus perimeter. (a) Bland-Altman plot of 110 nuclei perimeters obtained by the HTWS and the manually labeled ones. (b) Bland-Altman plot of 110 nuclei perimeters obtained by the GT and the manually labeled one. (c) Bland-Altman plot of 110 nuclei perimeters obtained by the AT and the manually labeled ones. (d) Bland-Altman plot of 110 nuclei perimeters obtained by the proposed technique and the manually labeled ones.

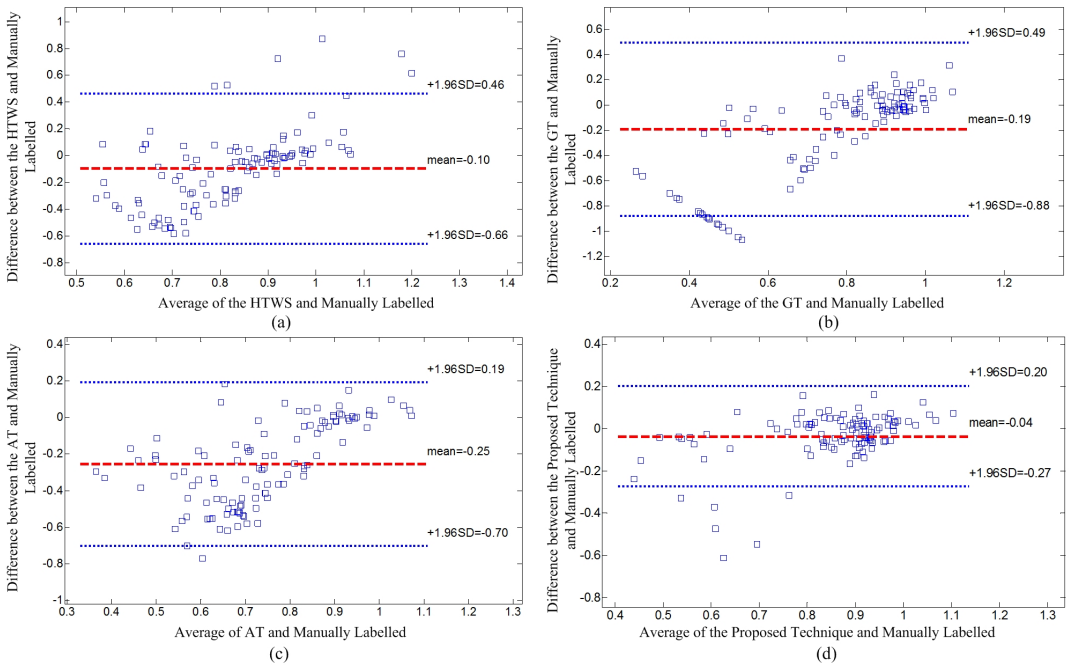

Fig. 5.10. Segmentation performance comparison of the nuclei segmentation techniques in terms of nucleus form factor. (a) Bland-Altman plot of 110 nuclei form factors obtained by the HTWS and the manually labeled ones. (b) Bland-Altman plot of 110 nuclei form factors obtained by the GT and the manually labeled one. (c) Bland-Altman plot of 110 nuclei form factors obtained by the AT and the manually labeled ones. (d) Bland-Altman plot of 110 nuclei form factors obtained by the proposed technique and the manually labeled ones.

5.4 Summary

In summary, this chapter presents a novel computer-aided technique for segmentation of the nuclei in histopathological images. The intra-object variations are first reduced by using the hybrid morphological reconstructions. A novel threshold selection algorithm for local regions is then used to segment the nuclei. By incorporating the domain specific knowledge, this technique reduces the under-segmentation of the nuclei and provides a superior performance compared to the existing techniques. The evaluation on H&E stained histopathological skin epidermis images (containing more than 3300 nuclei) shows the effectiveness of the technique. Although, the technique has been evaluated for the nuclei segmentation in skin histopathological images, it can be applied to nuclei segmentation in other organs.

Chapter 6

Detection of the Melanocytes[1]

In melanoma diagnosis, the segmentation and detection of the melanocytes in the epidermis area is an important step before the diagnosis is made. If the melanocytes can be found correctly, architectural and cellular features (e.g. size, distribution, location) can then be used to grade or determine the malignancy of the melanocytic skin tissue. In this chapter, we present the detection of the melanocytes in the skin epidermis area.

6.1 Introduction

In the epidermis area of skin, a normal melanocyte is typically a cell with a dark nuclei, lying singly in the basal layer of epidermis. However, in a melanoma or nevus, the melanocytes grow abnormally, and can be found in the middle layer of the epidermis. The digitized histopathological image we used in this work is stained with haematoxylin and eosin (H&E). Three examples of the skin epidermis image are shown in Fig. 6.1(a), (b), and (c). The cell nuclei are observed as dark blue whereas the intra-cellular material and cytoplasm are observed as bright pink. Note

[1]A version of this chapter has been published. Cheng Lu, Muhammad Mahmood, Naresh Jha, Mrinal Mandal. "Detection of Melanocytes in Skin Histopathological Images using Radial Line Scanning", *Pattern Recognition*. Volume 46, Issue 2, 2013, P. 509-518. Cheng Lu, Muhammad Mahmood, Naresh Jha, Marinal Mandal. "Automated Segmentation of the Melanocytes in Skin Histopathological Images", *IEEE Journal of Biomedical and Health Informatics* . Vol. 17, NO. 2, 2013, P. 284-296.

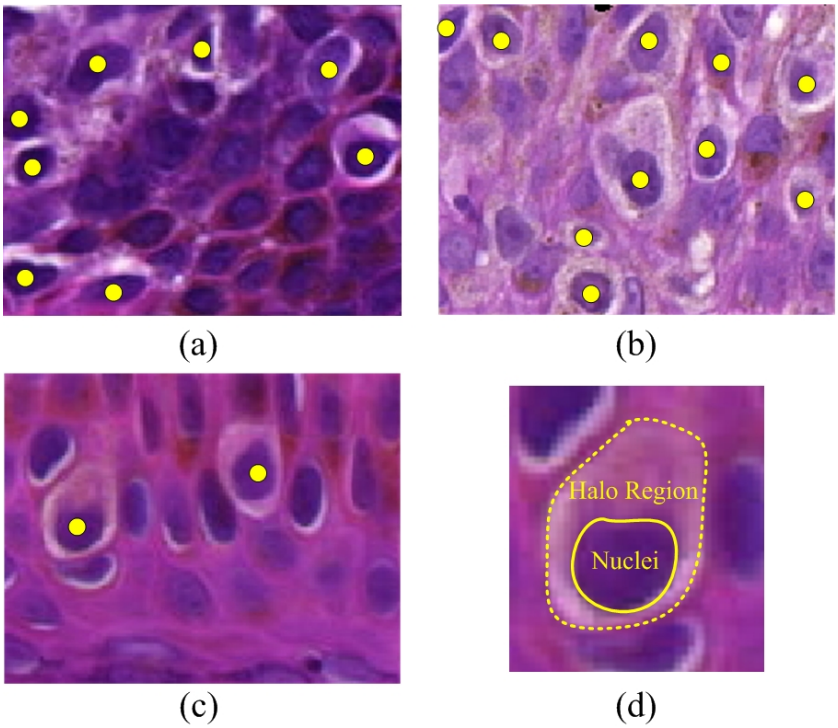

Fig. 6.1. Melanocytes in epidermis area from different skin tissues. Inter- and intra-image variations are observed in terms of the color. These images are sampled from the skin digitized slide under 30X magnification. In (a), (b), and (c) The bright seed points indicate the location of melanocytes whereas other nuclei are keratinocytes. (d) is a close up image of a melanocyte.

that the bright seed points indicate the location of melanocytes whereas other nuclei are the keratinocytes. It is noted that there exist inter- and intra-image color variations due to nonuniform absorption of the stain, and different handling procedure or other factors, e.g., stains fading. The high similarity between the melanocytes and other cytological components make it difficult to perform consistent quantitative analysis. It is observed that the differences between melanocytes and other keratinocytes are the surrounding region. In the case of melanocyte, it appears to lie in a brighter halo-like region and retracted from other cells, due to the shrinkage of cytoplasm [74]. One close up example of the melanocyte is shown in Fig. 8.8(d), where the outer dotted contour represents the halo region and the inner solid contour represents the nuclei. In contrast, the other keratinocytes are closely contact with the cytoplasm and it has no or little brighter area. The brighter halo-like region of the melanocyte is an important pattern for differentiation of the melanocytes and

other nuclei.

A lot of work has been conducted on the segmentation or detection of various biological components in a histopathological image using image processing techniques such as thresholding [12], [32] and watershed [75]. Gurcan *et al.* [32] proposed a hysteresis threshold based technique for the nuclei segmentation in neuroblastoma image. The technique first employs morphological operations to reduce the background signal. The hysteresis thresholding was then used to perform the segmentation. Petushi *et al.* [12] proposed to use adaptive threshold-based technique for the nuclei segmentation in the breast cancer image. With the assumption that the nuclei are bright objects in a relatively uniform dark background, Chen *et al.* [76] proposed the use of global threshold and watershed technique to segment the cancer cell nuclei in time-lapse microscopy. These threshold-based techniques typically fail when considerable intensity variations are present in the images. Nattkemper et al. [77] proposed a fluorescent lymphocytes detection technique using trained artificial neural networks. By incorporating the color, texture and shape information present in an image, Naik et al. [46] proposed to segment the nuclei using the Bayesian classifier. Sertel et al. [40] computed the probability map of karyorrhexis cells based on the estimated likelihood function, and the cell nuclei are then segmented using thresholding. Although these techniques have been reported to provide good performance, the performance is sensitive to the training samples. The histopathological images used in this chapter contain inter- and intra-image intensity variations due to the the staining imperfection. Also, because of the natural biological features of the skin epidermis, the foreground and the background objects have similar intensity values. Therefore, many of the above techniques seem unsuitable for our scenario.

In the melanocytes segmentation, the main difficulty is how to differentiate the melanocytes and keratinocytes in the skin epidermis area. These two kinds of cells have similar intensity and nuclei size. A similar problem has been addressed by Basavanhally et al. [41] in breast cancer diagnosis where the lymphocyte nuclei are differentiated from the cancer cell nuclei in H&E stained histopathological im-

ages. In their work, the two kinds of cells (cancer cell and lymphocytes) are differential based on the domain knowledge such as the nuclei size, intensity of the nuclei and spatial proximity. However, in skin histopathological images, the size of melanocytes are very similar to that of other keratinocytes. Due to the inter- and intra-image variations, the intensity value of the melanocytes and other keratinocytes are very close to each other. Therefore, the domain knowledge used in breast cancer detection [41] will not work well in the case of melanocytes detection.

There is another closely related work in the literature where all the nuclei are segmented in the skin epidermis area [33]. In this work, a threshold is calculated based on the assumption that cell nuclei covers approximately the darkest 20% of the pixel in the image. The pixels whose values are less than the threshold are labeled as nuclei regions. Morphological operations are then used to refine the segmented result. However, this global threshold based technique only works under the assumption that there is no intensity variations in the image, and usually generates under-segmentation results (many of the nuclei are grouped together). Also, there is no attempt to differentiate the melanocytes and keratinocytes.

Template matching technique is a popular technique in computer vision for pattern detection. Naik et al. [46] have used four binary elliptical templates with different major and minor axes to detect the nuclei in breast cancer histopathological images. It is observed in Fig. 8.8 that the melanocytes typically have low intensity values while its spatial surrounding space has brighter intensity values. It may be possible to detect the melanocytes using template matching technique with templates that have round darker heart encompassed by a brighter ring. However, several difficulties need to be addressed. First, the size of the template is hard to decide due to the size variations of the melanocytes even under the same magnification level. In the case of skin cancer, the melanocytes are larger than that in the case of normal skin or nevus skin. Secondly, the intensity level of the template is hard to determine. Therefore, it is difficult to decide a 'good' template to match the melanocyte patterns.

In order to address the above mentioned problems, we propose two novel tech-

niques to segment and detect the melanocytes in the skin epidermis area in this chapter. The first technique is based on the local double ellipses descriptor (LDED). The second technique is based on the radial line scanning (RLS). Unlike the existing techniques which usually assume relatively uniform background, the proposed techniques consider the inter- and intra-image variations due to the staining imperfection. Also, the proposed technique can provide good detection performance on histopathological images where the background is complex and has similar appearance with the foreground (i.e., the melanocytes). Furthermore, the proposed technique models the natural biological features, i.e., the shape and the distribution of intensity, as the parameters which make the technique robust. To our best knowledge, this is the first automated technique for joint segmentation and detection of the melanocytes in histopathological image of skin tissue. This technique operates on reliable quantitative measures and provides objective and reproducible information complementary to that of a pathologist. Such quantitative analysis of melanocytes is important for clinical applications, as well as for research purpose.

6.2 Proposed LDED-based Technique

In this section, we present the proposed LDED based technique which is primarily based on the local feature space analysis. The schematic of the proposed technique is shown in Fig. 6.2 which consists of two main steps. In the first step, we segment the candidate nuclei regions in the epidermis area using the technique shown in Chapter 4 [21]. In the second step, a novel descriptor, named local double ellipse descriptor (LDED), is proposed to perform the quantitative analysis. This descriptor builds two ellipsoid models based on the segmented candidate regions. The LDED then measures the local feature information using two well-defined parameters which incorporate the biological pattern of the melanocytes. The location of the melanocytes can then be identified by the LDED. The steps in the proposed technique are now presented in detail in the following.

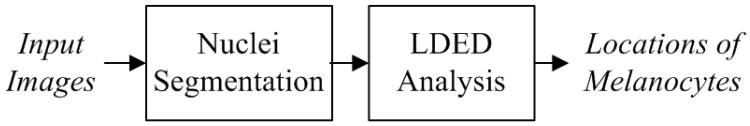

Fig. 6.2. The schematic of the proposed LDED based technique.

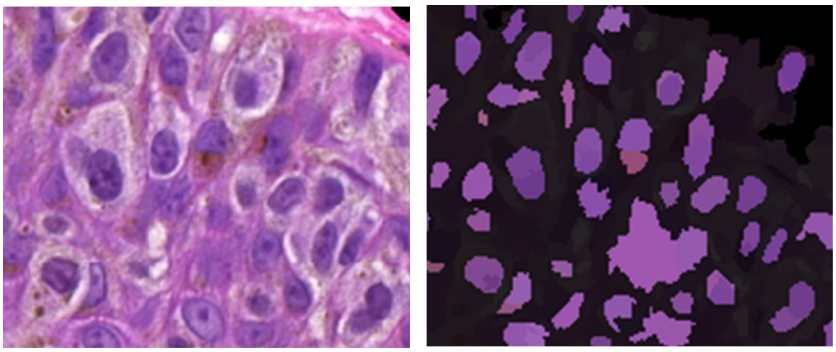

Fig. 6.3. An example of the mean shift segmentation. (a) The original image; (b) the segmented image obtained by the adaptive threshold technique [21].

6.2.1 Segmentation of Nuclei

Before performing the LDED analysis, we first segment all the nuclei in the image. Considering the intensity variations, an adaptive threshold technique is applied to segment the nuclei regions (described in Chapter 4 and [21]). Fig. 6.3 shows an example of the original image, and the segmented image.

6.2.2 Local Double Ellipse Descriptor Analysis

In this section, a novel descriptor, LDED, which is based on a double ellipsoidal model, is proposed. The LDED utilizes the candidate regions $\{N_p\}_{p=1...K}$ and its surrounding local features to discriminate the melanocytes and other cytological components. The details of the LDED analysis are presented in the following sub-sections.

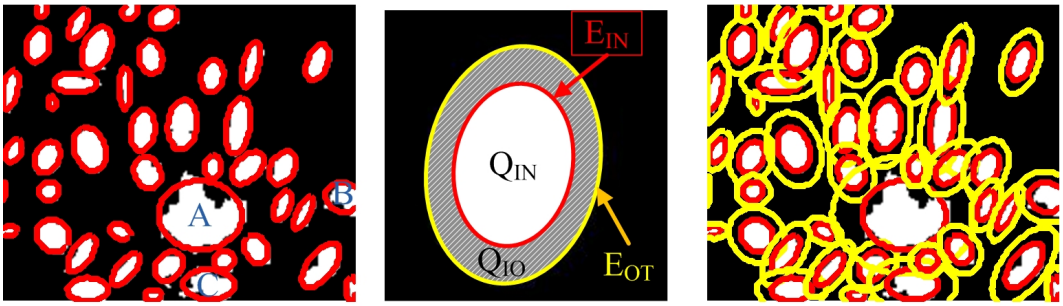

(a) (b) (c)

Fig. 6.4. The Elliptical modeling for each nucleus. (a) The original single Elliptical model on Fig. 6.3(b). (b) Illustration of the LDED (c) Double Elliptical model on Fig. 6.3(b).

6.2.2.1 Construction of the elliptical model

At first, an ellipse is fitted based on the boundary points of a candidate region N_p using the direct least square fitting algorithm [55] (see Appendix B). Fig. 6.4(a) shows the ellipses obtained by fitting the boundary points of the image shown in Fig 6.3(b). It is observed in Fig. 6.4(a) that most of the nuclei are fitted well with ellipses. However, there are a few regions (for example, the regions labeled as A, B, and C in the figure) that have irregular shapes and can not be fitted well by an ellipse. These regions needed to be eliminated for efficient nuclei detection.

6.2.2.2 Construction of the Double Ellipse Descriptor

Note that by the above mentioned elliptical model, we can measure the shape of the nuclei region. However, in order to capture the local information of the nuclei region, we need to build another Elliptical model that have larger capturing range. Let E_{IN} denote the above mentioned elliptical model, and henceforth referred to as the inner elliptical model. We now build another Elliptical model E_{OT}, named outer/enlarged elliptical model, such that it has the same centroid position with that of E_{IN}, but has larger minor and major axes. The outer elliptical model is proposed to capture the surrounding local information of the current candidate nuclei region. Typically the enlarged major and minor axes have a factor of 1.4 (the enlargement factor decides the local range of the measurement). Fig. 6.4(c) shows the formation

of outer elliptical model around the inner Elliptical model for each nucleus region N_p. Denote the points set inside the inner Elliptical model as Q_{IN}, the points set inside the outer Elliptical model as Q_{OT}, and the points set between the inner and outer Elliptical model as Q_{IO}, i.e., $Q_{IO} = Q_{OT} - Q_{IN}$. The Q_{IN}, Q_{IO} and Q_{OT} constitute the LDED as shown in Fig. 6.4(b). The Q_{IN} is shown in Fig. 6.4(b) as the white area, Q_{IO} is the shadow area between E_{IN} and E_{OT}, and Q_{OT} is the area consisting of Q_{IN} and Q_{IO}. The Q_{IO} can measure the surrounding area of the candidate nuclei. Based on the defined LDED, we now discuss two measurements in the following.

6.2.2.3 Detection of the Nuclei using Ellipticity Parameter

As shown in Fig. 6.4(a), a few false positives, i.e., the regions which are not true nuclei, are expected to be present in the candidate regions $\{N_p\}_{p=1...K}$. Based on the assumption that a nuclei typically has an elliptical shape, we can filter out the false positives by using the ellipticity of a region with the inner elliptical model. It is possible to detect the false positives by thresholding $||\mathbf{D}\hat{\mathbf{a}}||^2$ obtained using Eq. B-7 (see Appendix). However, in this chapter, we propose to use another measure which is visually more intuitive to detect the false positives. Denote S as the set of pixels in a candidate region N_p. A parameter which measures the ellipticity, e_E, is defined as follows:

$$e_E \equiv 1 - \frac{|S \oplus Q_{IN}|}{|Q_{IN}|} = \frac{|S \cap Q_{IN}|}{|Q_{IN}|} \tag{6.1}$$

where $\oplus$ is the exclusive OR operation, and $|\cdot|$ is the cardinality of a point set. Note that a region with a high ellipticity parameter e_E will have a closer match to an the elliptical shape, and is likely to be a nucleus. On the other hand, a region with a low ellipticity parameter e_E indicates that this region contains noisy connecting component (either concave or convex component), and is not likely to be a true nucleus region.

Three examples with different ellipticity parameters e_E are shown in the first two columns of Fig. 6.5. In Fig. 6.5 (b), (f), and (j), the candidate regions are

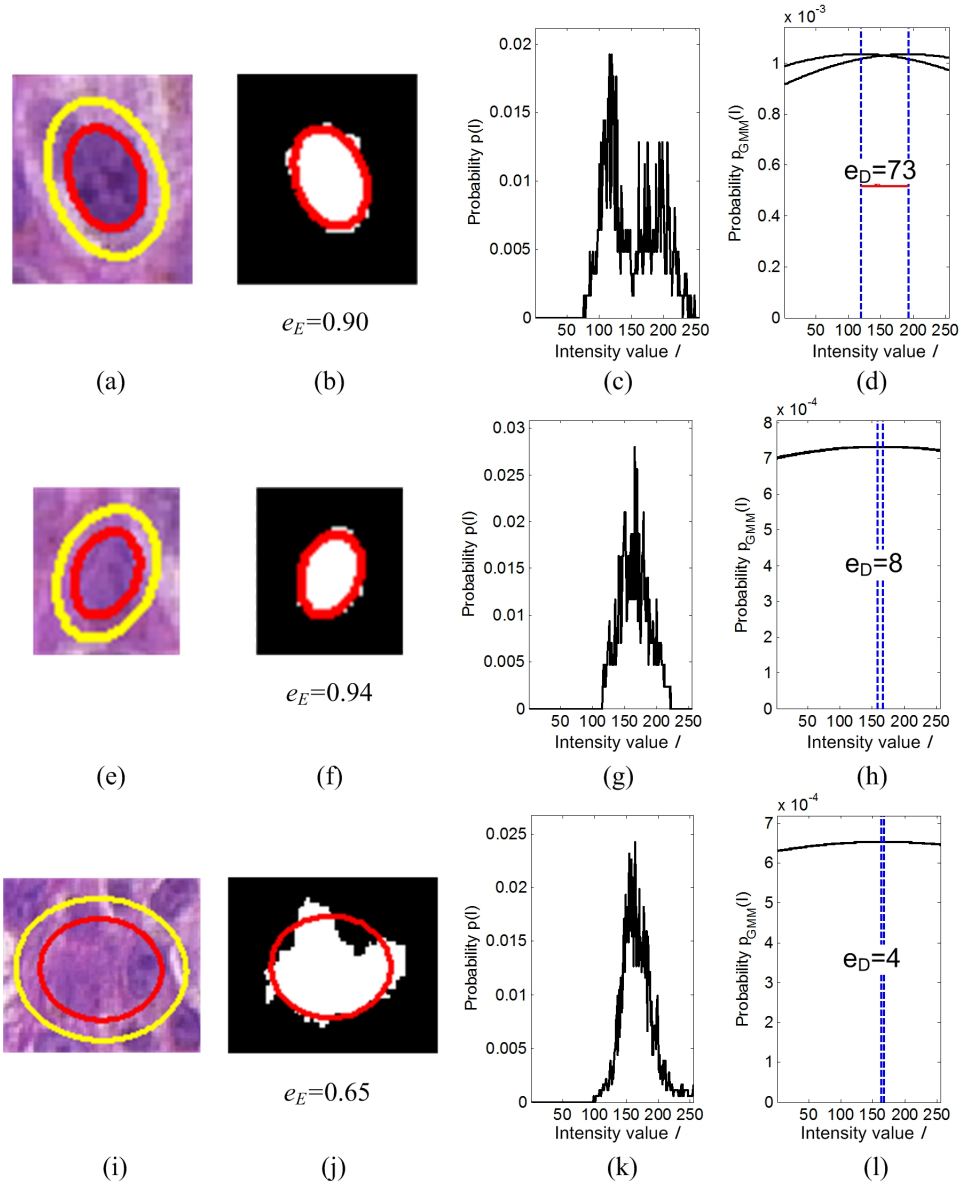

Fig. 6.5. Illustrations of two parameters e_E and e_D for three different candidate nuclei regions. (a), (e), and (i) show three candidate nuclei regions with their corresponding LDED overlapped. (b), (f), and (j) show the ellipticity parameters provided by the inner Elliptical model E_{IN}. (c), (g), and (k) show the pdf of the intensity values set obtained by the outer Elliptical model E_{OT}. We used the red channel intensity from the color RGB image in this chapter. (d), (h), and (l) are the correspondence GMM estimated from (c), (g), and (k), respectively. The Gaussian model is draw by the solid black line and the center of each Gaussian model is indicated by the dash line. The parameter e_D for these three cases are 73, 8 and 4, respectively. Note that the first row shows a case of melanocyte, the second row shows a case of other nuclei, the third row shows a case of nosy component which is not a nucleus.

represented by white pixels. The ellipse represents the inner Elliptical model E_{IN}. The e_E value indicates the corresponding ellipticity parameters. Note that the candidate regions shown in Fig. 6.5(b) and (f) are true nuclei regions with high values of e_E ($e_E = 0.90$ and $e_E = 0.94$, respectively). In contrast, the candidate region shown in Fig. 6.5(j) is a false nuclei region with a low value of e_E (e_E=0.65). In other words, using this parameter we can eliminate the false nuclei regions. A segmented region N_p corresponds to a nucleus if the following condition is satisfied:

$$e_E^{N_p} \geq \tau_E \tag{6.2}$$

where $e_E^{N_p}$ is the ellipticity parameter for region N_p calculated using Eq. 6.1, and τ_E is a pre-selected threshold. Let us assume that the above test is satisfied by K' regions, i.e., there are K' nuclei in the image. Let these regions denoted by $\{N'_p\}_{p=1...K'}$.

6.2.2.4 Detection of the Melanocytes

After the nuclei detection, the task is now to distinguish the melanocytes from other nuclei. Note that in the epidermis skin image, a normal melanocyte is typically a small cell with a dark nuclei, lying singly in the basal of epidermis. In digitized image, it appears to lie in a clear space and retracted from other cells, due to the shrinkage of cytoplasm [74]. As for the atypical melanocytes, the nuclei becomes larger and has irregular contour, but the pattern is the same. This pattern can be easily observed in Fig. 6.6(a) and (b). Note that we focus on the red channel of the RGB color image for LDED analysis in this chapter. It is observed that the nuclei of the melanocytes prefer to have low intensity value while its spatial surrounding space presents higher intensity value. It is shown in the histogram that there are two distinct modes present. The centers of these two modes lie around intensity value 110 and 175. On the other hand, in the case of other nuclei (shown in Fig. 6.6(c) and (d)), it is difficult to find the two distinct modes and the histogram usually is uni-modal.

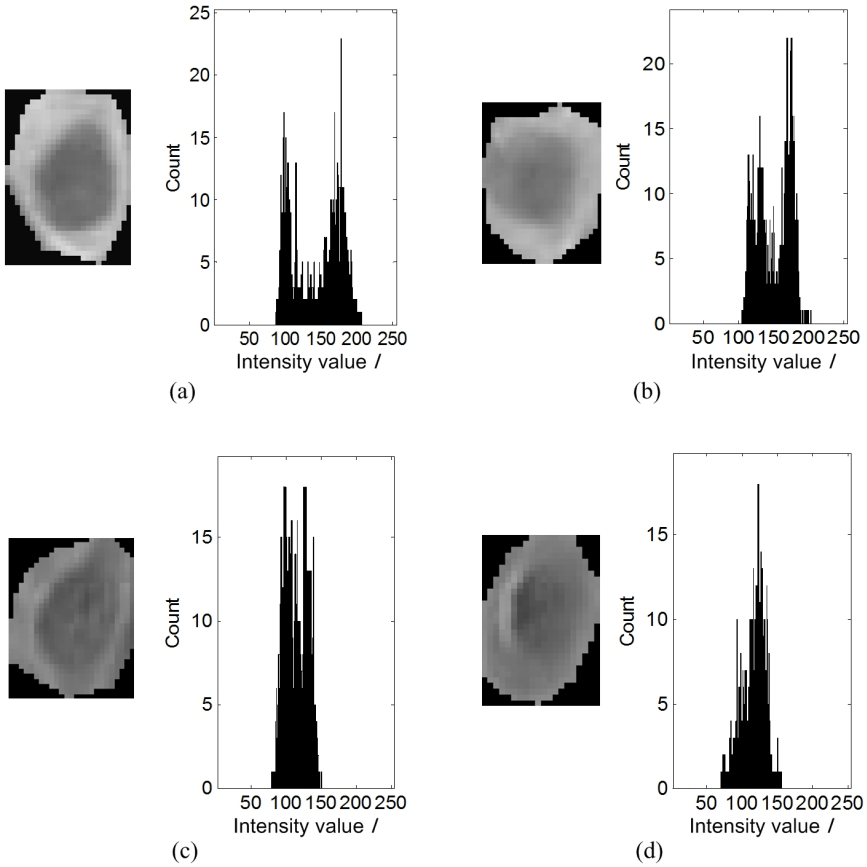

Fig. 6.6. The manually cropped melanocytes and other nuclei as well as the corresponding histograms. (a) and (b) show two typical melanocytes; (c) and (d) show two other nuclei. Note that the images are obtained from the red channel of the color image. The horizonal axis is the gray value whereas the vertical axis is the counting number of corresponding intensity value in red channel.

Based on the histogram patterns shown in Fig. 6.6, we propose a novel method to distinguish the melanocytes and other keratinocytes. The basic idea is that we first model the underlying probability density function (*pdf*) as a two univariate Gaussian mixture model (GMM). The distance of the two Gaussian modes is then used to distinguish the melanocytes and other keratinocytes.

Denote the pixel intensity set inside the outer Elliptical model E_{OT} for the candidate nuclei region N_p as I^{N_p}. Let the means and covariances of this two Gaussian mixture model be denoted as μ_i and σ_i^2 ($i = 1, 2$), respectively. Denote I as an observed sample, which is a pixel intensity value observed from the intensity set I^{N_p}. The *pdf* of the intensity value is expressed as follows:

$$p(I|\theta) = \sum_{i=1}^{2} P(\omega_i) p(I|\omega_i, \theta_i) \tag{6.3}$$

where θ represents the set of four unknown parameters $(\mu_1, \mu_2, \sigma_1^2, \sigma_2^2)$. The two modes, denoted by classes ω_1 and ω_2, indicate the Gaussian distribution corresponding to the current observed sample I. $P(\omega_i)$ is the *prior* probability for the two Gaussian modes in the GMM, and $p(I|\omega_i, \theta_i)$ is the class *conditional probability* which follows the Gaussian distribution as follows:

$$p(I|\omega_i, \theta_i) = \frac{1}{\sqrt{2\pi\sigma^2}} exp(-\frac{(I-\mu_i)^2}{2\sigma^2}). \tag{6.4}$$

In order to estimate the parameters set θ, we evaluate the log likelihood of the observed intensity values in the intensity set I^{N_p} as follows:

$$L(\theta) = log \prod_{j=1}^{n} p(I_j|\theta) = \sum_{j=1}^{n} log[\sum_{i=1}^{2} P(\omega_i) p(I_j|\omega_i, \theta_i)] \tag{6.5}$$

where n is the total number of intensity values in the intensity set I^{N_p}, I_j is the jth intensity value. Note that finding the maximum likelihood with respect to the parameters θ using Eqn. 6.5 is difficult as we cannot find a closed form solution for it. The parametric Expectation Maximization (EM) algorithm is used to estimate the parameter. In EM algorithm, a modified log likelihood function $\widetilde{L}(\theta)$ is calculated

by introducing the *posteriori* $P(\omega_i|I_j,\theta_i)$ as follows:

$$\widetilde{L}(\theta) = \sum_{j=1}^{n}\sum_{i=1}^{2} P(\omega_i|I_j,\theta_i) log P(\omega_i) p(I_j|\omega_i,\theta_i). \tag{6.6}$$

The objective now is to find the parameter set θ that will maximize $\widetilde{L}(\theta)$. In EM algorithm this is done iteratively where each iteration consists of two steps: expectation (E) step and maximization (M) step. In the E-step, the *posteriori* probability is estimated using the Bayes rule with a given parameter set θ as follows:

$$P(\omega_i|I_j,\theta_i) = \frac{P(w_i)p(I_j|\omega_i,\theta_i)}{\sum_{k=1}^{2} P(w_k)p(I_j|\omega_k,\theta_k)}. \tag{6.7}$$

In the M-step, the parameters that maximize the log likelihood function in Eq. 6.6 are estimated as follows:

$$\mu_i = \frac{\sum_{j=1}^{n} P(\omega_i|I_j,\theta_i) I_j}{\sum_{j=1}^{n} P(\omega_i|I_j,\theta_i)} \tag{6.8}$$

$$\sigma_i^2 = \frac{\sum_{j=1}^{n} P(\omega_i|I_j,\theta_i)(I_j-\mu_i)^2}{\sum_{j=1}^{n} P(\omega_i|I_j,\theta_i)} \tag{6.9}$$

$$P(\omega_i) = \frac{1}{n}\sum_{j=1}^{n} P(\omega_i|I_j,\theta_i) \tag{6.10}$$

The EM algorithm recursively repeats the expectation and the maximization steps until $\widetilde{L}(\theta)$ converges [78]. The estimated GMM represents the underlying pdf of the intensity values retrieved by the outer elliptical model. Based on the estimated GMM, the following parameter is proposed to distinguish the melanocytes and other nuclei:

$$e_D = |\mu_1 - \mu_2|. \tag{6.11}$$

Note that the parameter e_D computes the mean difference of the estimated GMM. Intuitively, if the underlying distribution of the I^{N_p} is a distinct bi-modal distribution, the parameter e_D has a large value. On the other hand, if the underlying distribution of the I^{N_p} is a uni-modal distribution, the parameter e_D has a small value.

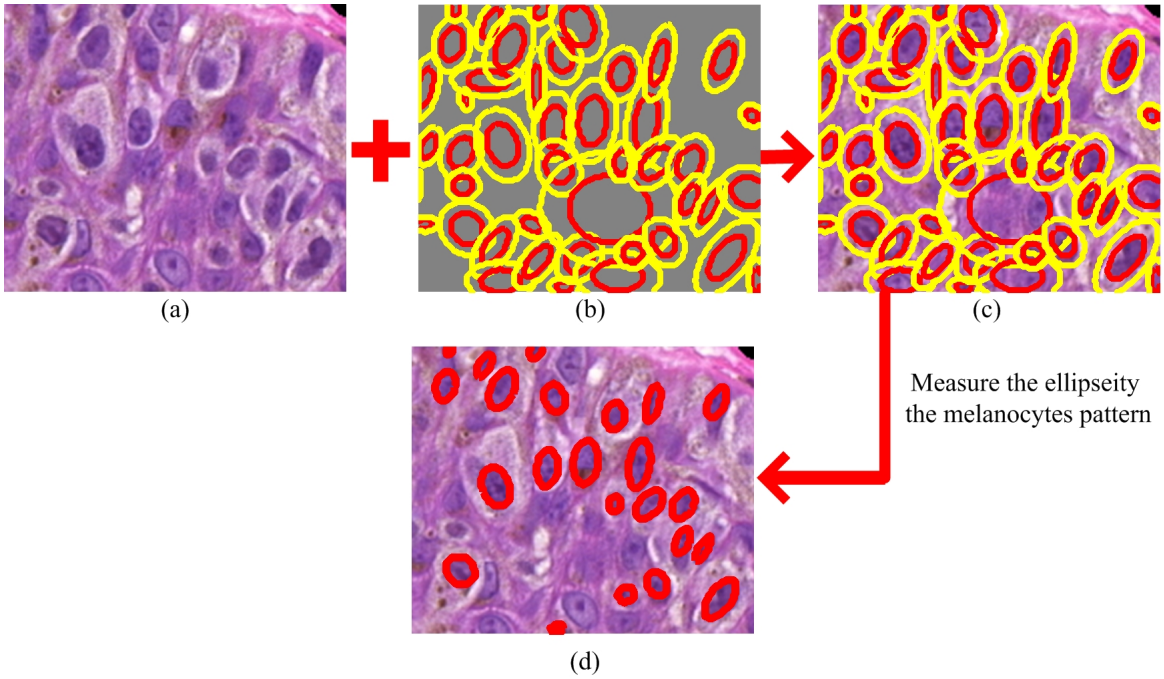

Fig. 6.7. Illustration of the LDED analysis. (a) Original image. (b) All the LDEDs. (c) LDEDs overlap onto the original image to perform the analysis. (d) Detection of the melanocytes using the analysis on two parameters e_E and e_D. The detected melanocytes are label as red ellipses.

Basically, this parameter measures the local intensity features of the nuclei regions and will serve as an important factor in identifying the melanocytes from other candidate regions. Three examples of computing the parameter e_D are shown in the Fig. 6.5. Three candidate nuclei regions with the overlapped LDEDs are shown in Fig. 6.5(a), (e), and (i). The corresponding *pdfs* of the intensity sets obtained by the outer Elliptical model E_{OT} are shown in Fig. 6.5(c), (g), and (k), respectively. The corresponding GMM estimated using the EM algorithm are shown in Fig. 6.5(d), (h), and (l), respectively. It is observed that for the true melanocyte (shown in the first row), the two estimated Gaussian modes are distinctly apart from each other, and result in a high value of e_D ($e_D = 73$). For the non-melanocytes regions (shown in the second and third rows of Fig. 6.5), the modes in the GMM overlap and we obtain a low value of e_D ($e_D = 8$ and $e_D = 4$ as shown in Fig. 6.5(h) and (l), respectively).

Using the parameter e_D measured by the LDED, we can now detect the melanocytes from the candidate nuclei regions $\{N'_p\}_{p=1...K'}$. A segmented region N'_p corresponds

to a melanocyte if the following condition is satisfied:

$$e_D^{N_p'} \geq \tau_D \tag{6.12}$$

where $e_D^{N_p'}$ is the parameter of region N_p' calculated using Eq. 6.11, and τ_D is the threshold for e_D.

Algorithm 1 The algorithm for LDED analysis

Input: Candidate nuclei regions set $\{N_p\}_{p=1...K}$.
Initialization: $\{M_p\}_{p=1...O} = \emptyset$.
for each region N_p **do**
  Construct double elliptical model.
  Calculate parameter e_E using Eq. 6.1.
  Calculate parameter e_D using Eq. 6.8 and Eq. 6.11 via EM algorithm.
  if $e_D^{N_p} \geq \tau_D$ and $e_E^{N_p} \geq \tau_E$, **then**
    Assign current region to the melanocyte regions set, $N_p \rightarrow \{M_p\}_{p=1...O}$.
  end if
end for
Output: Melanocyte regions set $\{M_p\}_{p=1...O}$.

Note that the ellipticity parameter e_E serves as an indicator of the nuclei region, while the second parameter e_D serves as an indicator for the melanocytes. From experiments, it has been found that $\tau_E \approx 0.8$ and $\tau_D \approx 34$ provides good performance. The algorithm for the LDED analysis is shown in Algorithm 2. An illustration of the LDED analysis is shown in Fig. 6.7. The original image is shown in Fig. 6.7(a) whereas the formation of the LDED is shown in Fig. 6.7(b). Fig. 6.7(c) illustrates the LDED superimposed on the original image, and the two parameters are measured. The final melanocytes detection result is shown in Fig. 6.7(d). It is observed that the technique could find all the melanocytes in the image.

6.3 Proposed RLS-based Technique

The schematic of the proposed RSL based technique for melanocytes detection is shown in Fig. 8.9. It is observed that there are three modules. At first, the nuclei in the image are segmented using an adaptive thresholding technique which incor-

porates the domain knowledge. In the second module, the halo region is estimated for each pre-segmented nuclei region by using the radial line scanning (RLS) algorithm. Finally, the melanocytes are detected based on the estimated halo region and the pre-segmented nuclei region. Details of these three modules are presented in the following.

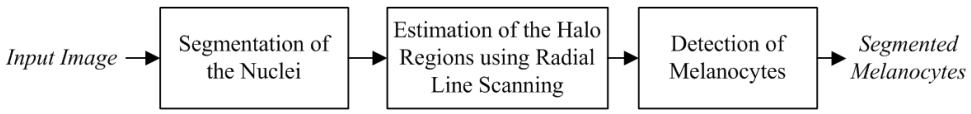

Fig. 6.8. The schematic of the proposed melanocyte detection technique.

6.3.1 Segmentation of the Nuclei

Before performing the melanocytes detection, we first segment all the nuclei in the image. Considering the intensity variations, an adaptive threshold technique is applied to segment the nuclei regions (described in Chapter 4 and [21]). Fig. 6.9(a) shows an original image containing three nuclei, and the melanocyte is label with letter 'M'. In Fig. 6.9(b), the segmented nuclei regions are shown as the white regions in a binary image.

6.3.2 Estimation of the Halo Regions using RLS

After the segmentation of nuclei, we are now ready to detect the melanocytes from the pre-segmented nuclei. In order to capture the 'Mpattern', we propose the RLS algorithm, which makes use of the radial lines originating from the centroid of a nuclei. The RLS algorithm consists of four steps. The first step is to initialize the radial center and radial lines for each nuclei regions. These radial lines will be used for measuring the information from the image in order to estimate the halo region. The second step generates the gradient map of the image, which provides the edge information for the radial lines. In the third step, the halo region of each nuclei is estimated based on the gradient information measured by the radial lines.

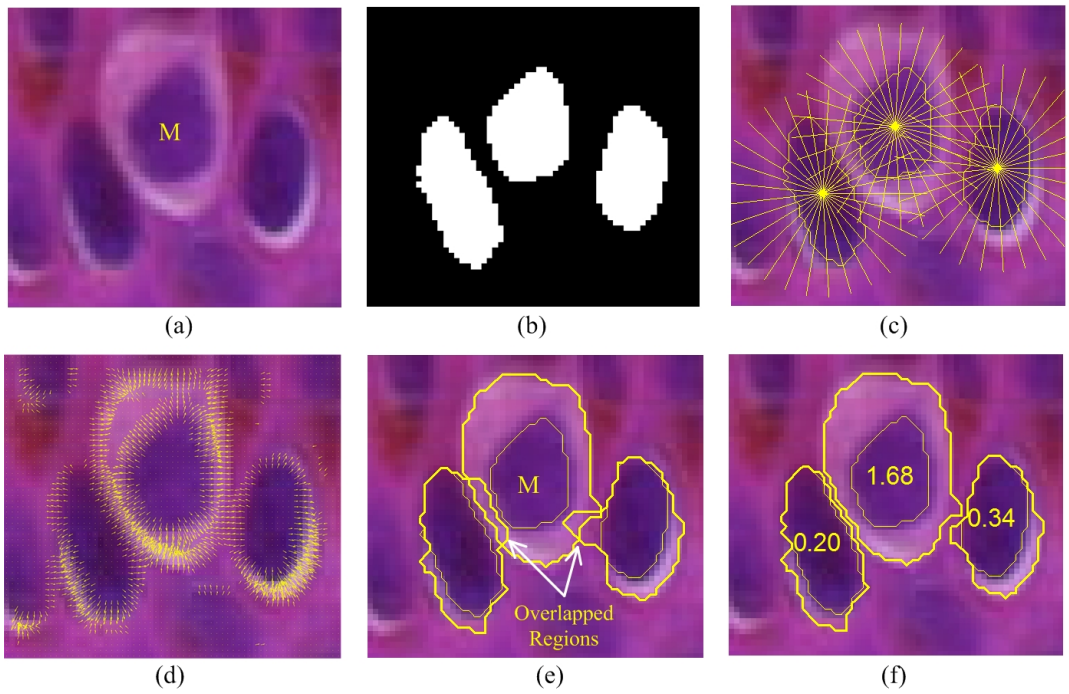

Fig. 6.9. Illustration of the RLS algorithm. (a) is the original image with three nuclei regions where the melanocyte is indicates with letter 'M'. (b) shows the segmented nuclei regions. (c) shows the radial lines for each nuclei region (nuclei regions are shown with thick contours). (d) shows the suppressed smoothed gradient map. (e) shows the estimated halo regions without resolving the overlap. (f) shows the overlap resolved results of (e). The value of the parameter R_{HN} discussed in Section 6.3.3 is shown inside the nuclei region as well.

In the final step, the overlapping region problem is resolved. These four steps are described in the following.

6.3.2.1 Initialization of Radial Center and Radial Lines

In this step, we first calculate the centroid of each pre-segmented nuclei. Let the centroid coordinate be denoted by (C_x, C_y). Using the centroid as a radial center, a set of radial lines with different radial angles are calculated as follows:

$$\theta_i = \frac{2\pi}{k}(i-1), i = 1 \ldots k \tag{6.13}$$

where k indicates the number of radial lines. An illustration of the radial center (C_x, C_y) and its radial lines $\theta_i, i = 1 \ldots k$ is shown in Fig. 6.10(a). Note that the nuclei contour is shown as the thick solid contour whereas the dotted circle

indicates the maximum range of the radial line (denoted as R_{max}). The solid point in the center indicates the radial center (C_x, C_y) and a set of 16 radial lines are shown as the thick solid lines. In this chapter, the radial lines are denoted by its radial angle θ. For example, the first and second radial lines θ_1 and θ_2 are shown in the Fig. 6.10(a) and the radial angles for these two radial lines are 0 and $\pi/8$, respectively. Denote the nuclei boundary point at given radial angle θ_i as $b(\theta_i)$. In Fig. 6.10(a), $b(\theta_1)$ and $b(\theta_2)$ indicate the nuclei boundary point on given radial lines θ_1 and θ_2, respectively.

Note that R_{max} specifies the maximum range of the radial line and it is identical for all the radial lines, i.e., $R_{max}(\theta_i) = R_{max}$. In Fig. 6.10(a), the maximum range R_{max} of a radial line is labeled.

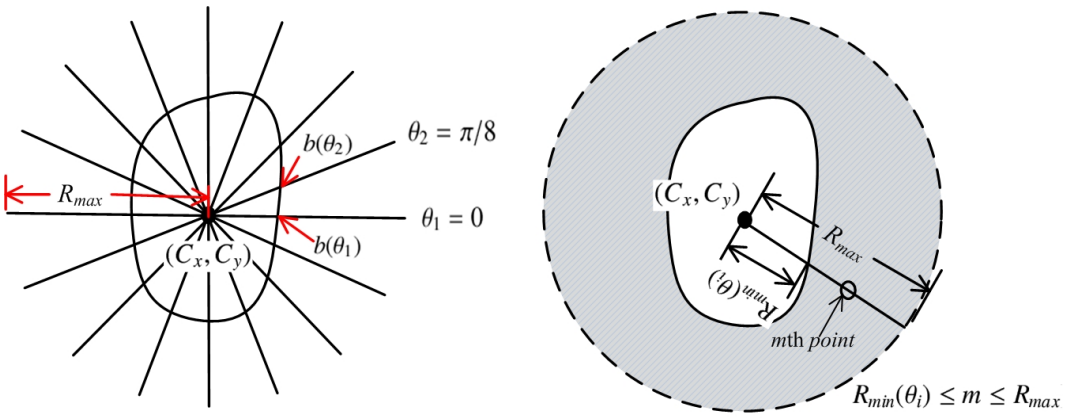

Fig. 6.10. Illustration of the notation of radial center and radial line.

A radial line consists of R_{max} points and is index from 1 to R_{max}. We define a valid scanning range for each radial line in order to reduce the computational time. We define $R_{min}(\theta_i)$ as the distance from the radial center to the nuclei boundary point $b(\theta_i)$. Note that the minimum valid scanning range maybe different for each radial line. Now, let m be the index of the point on the radial line, and the valid scanning range of the index should range from $R_{min}(\theta_i)$ to R_{max}, i.e., $R_{min}(\theta_i) \leq m \leq R_{max}$. An illustration of the above mentioned notation is shown in Fig. 6.10(b). Note that one of the radial lines is shown as a thick solid line.

The hollow point on the radial line represents the mth valid scanning point in the range of $[R_{min}(\theta_i), R_{max}]$. The shadow region shown in Fig. 6.10(b) indicates the valid scanning range. The radial centers and radial lines for Fig. 6.9(a) is shown in Fig. 6.9(c). These radial lines will be used later to measure the information from the image.

6.3.2.2 Gradient Map Generation

In the proposed technique, we estimate the halo region for each nuclei by analyzing the image features on the pre-initialized radial lines. The gradient is a very useful feature in the image that can help to estimate the halo region, and hence in this step, we generate the gradient map for the latter analysis. Denote the image as I and its 2-D coordinates as (x, y). In order to reduce the noise, a smooth image I_s is obtained by convolving the image with a Gaussian kernel $G_\sigma(x, y) = \sigma^{-1/2} e^{-(x^2+y^2)/4\sigma}$. In other words, $I_s(x, y) = G_\sigma(x, y) * I(x, y)$. The gradient magnitude map $\mathcal{G}_m$ and the gradient direction map $\mathcal{G}_d$ are then generated using the following equations:

$$\mathcal{G}_m(x, y) = ||\nabla I_s(x, y)|| = \sqrt{\left(\frac{dI_s(x, y)}{dx}\right)^2 + \left(\frac{dI_s(x, y)}{dy}\right)^2}, \tag{6.14}$$

$$\mathcal{G}_d(x, y) = arctan(\frac{dI_s(x, y)}{dy} / \frac{dI_s(x, y)}{dx}). \tag{6.15}$$

To suppress the weak gradients, the following equation is used:

$$\mathcal{G'}_m(x, y) = \begin{cases} \mathcal{G}_m(x, y), & if\ \mathcal{G}_m(x, y) \geq mean(\mathcal{G}_m(x, y)) \\ 0, & otherwise \end{cases} \tag{6.16}$$

$$\mathcal{G'}_d(x, y) = \begin{cases} \mathcal{G}_d(x, y), & if\ \mathcal{G}_m(x, y) \geq mean(\mathcal{G}_m(x, y)) \\ 0, & otherwise \end{cases} \tag{6.17}$$

Eq. 6.16 and Eq. 6.17 suppress the gradients whose magnitude are less than the mean gradient magnitude. The gradient map $\mathcal{G}'(x, y)$ is shown in Fig. 6.9(d) where

the gradient (shown as arrows) is super imposed on the image.

6.3.2.3 Estimation of the Halo Regions

The melanocytes can be distinguished from other keratinocytes based on their bright halo-like regions. In this step, we use the radial lines and the pre-computed gradient map to detect the boundary points for the halo regions estimation. On each radial line with radial angle θ_i, there are two kinds of boundary point: the inner boundary point and outer boundary point. We assume that the inner boundary point are located at the boundary of the pre-segmented nuclei. Therefore, in this section, we aim to detect the outer boundary point, denoted as $BP(\theta_i)$, for the halo region. All the outer boundary points $\{BP(\theta_i), i = 1, \ldots, k\}$ will then form the outer halo contour which can constrain a halo region. In Fig. 8.8(d), the dotted contour corresponds to the outer boundary contour that consists of outer boundary points whereas the solid contour corresponds to the inner boundary contour that consists of inner boundary points. Ideally, for the melanocytes, the halo-like regions surrounding the nuclei are segmented by the detected outer boundary points; whereas for the other keratinocytes, the detected outer boundary points only encompass the nuclei themselves, i.e., the outer boundary points are equal to the inner boundary points since there is no halo region.

Before introducing how to estimate the boundary points of the halo region, let us first analyze the gradient information around the halo region of a typical melanocyte (see Fig. 6.11). It is observed that the gradient map (shown as small arrows) is superimposed onto the image where the gradient magnitude is represented by the length of the arrow and the gradient direction is represented by the direction of the arrow. Because the intensity of the halo region is higher than the neighboring regions, the gradient directions point towards the halo region both from the nuclei and from the outer region. The dotted contour indicates the ground truth halo region's outer contour which consists of several outer boundary points. It is noted that the outer boundary points should have gradient direction that opposite to the radial line. For a given radial line with radial angle θ_i, we denote the gradient direction of

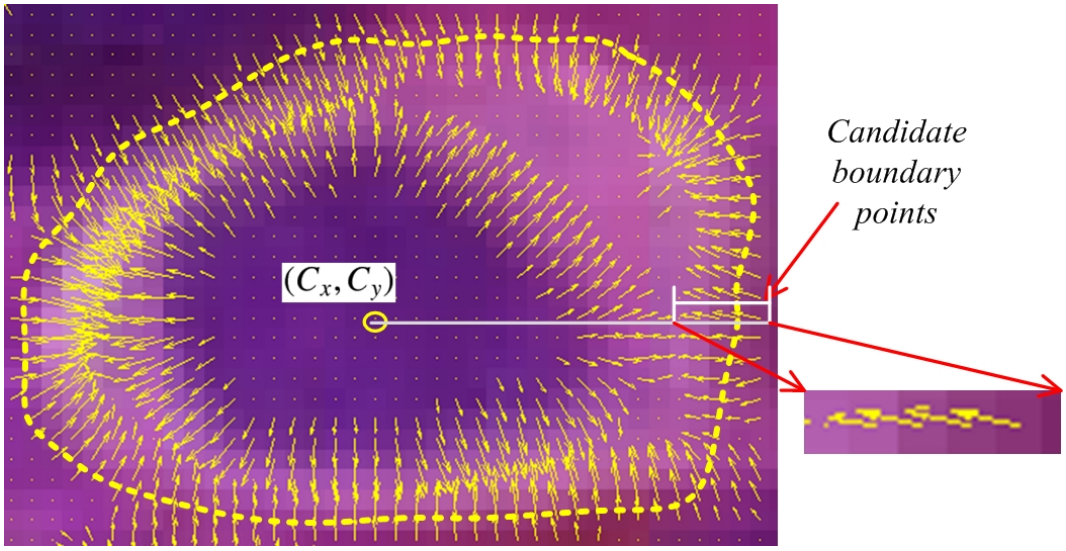

Fig. 6.11. A close up example of a melanocyte with gradient map. The gradient map (shown as small arrows) is superimposed onto the image. The dotted contour indicates the ground truth halo region's outer contour. An enlarged version of the boundary is shown in the small image on the right.

a outer boundary point for the halo region as $BP_{\mathcal{G}'_d}(\theta_i)$. Based on the characteristic of the gradient direction, we assume that the angle difference between $BP_{\mathcal{G}'_d}(\theta_i)$ and the radial angle of a radial line should satisfy the following condition:

$$\frac{\pi}{2} < |\theta_i - BP_{\mathcal{G}'_d}(\theta_i)| < \frac{3\pi}{2}. \tag{6.18}$$

In an ideal case, the gradient direction and the radial angle are strictly opposite, i.e., $|\theta_i - BP_{\mathcal{G}'_d}(\theta_i)| = \pi$. In order to allow the variations, we assume that $BP_{\mathcal{G}'_d}(\theta_i)$ to be $\theta_i \pm \pi/2$, or satisfies Eq. 6.20. In Fig. 6.11, a radial line with radial angle $\theta_1 = 0$ is shown. On this radial line, the candidate outer boundary points are labeled.

Let $\mathcal{G}'_m(\theta_i, m)$ and $\mathcal{G}'_d(\theta_i, m)$ represent, respectively, the gradient magnitude and direction on the mth point of the radial line θ_i. Based on the above analysis, a outer boundary point is expected to maximize the following cost function:

$$\mathcal{C}(\theta_i, m) = |cos[\alpha(\theta_i, m)]| + \mathcal{G}'_m(\theta_i, m), R_{min}(\theta_i) \leq m \leq R_{max} \tag{6.19}$$

where $\alpha(\theta_i, m)$ is the angle difference between gradient direction and the direction

of the radial line, which is defined as follows:

$$\alpha(\theta_i, m) = |\theta_i - \mathcal{G}'_d(\theta_i, m)|. \tag{6.20}$$

For each radial line, the outer boundary point for the potential halo region is calculated using the following equation:

$$BP(\theta_i) = \begin{cases} arg_m max\{\mathcal{C}(\theta_i, m)\}, & if\ \exists m, \frac{\pi}{2} < \alpha(\theta_i, m) < \frac{3\pi}{2} \\ R_{min}(\theta_i), & Otherwise \end{cases} \tag{6.21}$$

Eq. 6.21 examining the gradient information (the direction and the magnitude) of each point on the radial line. If there exist one or more points satisfying $\frac{\pi}{2} < |\alpha(\theta_i, m)| < \frac{3\pi}{2}$, the one with maximum cost function value $\mathcal{C}(\theta_i, m)$ is estimated as the outer boundary point for the current radial line. If there is no point (on the radial line) satisfying $\frac{\pi}{2} < |\alpha(\theta_i, m)| < \frac{3\pi}{2}$, we choose the point corresponding to the minimum valid range as the estimated outer boundary point.

The idea of the outer boundary point estimation using Eq. 6.21 is further explained in Fig. 6.12. In Fig. 6.12(a), six blocks are shown which represent six pixels/points that comprise the valid range of a radial line θ_i (in this case $\theta_i = \pi/2$). We denote each block, from bottom to the top, as the 1st to 6th pixels on the radial line. On each pixel, we have corresponding gradient information which are represented by the arrows. Note that the gradient direction is indicated by the direction of the arrow whereas the gradient magnitude is indicated by the length of the arrow. It is observed that the 3rd, 5th, and 6th pixel satisfies the condition $\frac{\pi}{2} < |\alpha(\theta_i, m)| < \frac{3\pi}{2}$. These pixels are the candidate outer boundary points on the current radial line. In order to determine the final outer boundary point, the cost function value $\mathcal{C}(\theta_i, m)$ is calculated (as shown in Eq. 6.19). The pixel corresponding to the maximum cost function value will be chosen as the outer boundary point. In Fig. 6.12(a), the outer boundary point $BP(\theta_i)$ is the 5th pixel. Fig. 6.12(b) shows another case, where there is no pixel whose gradient satisfy the condition $\frac{\pi}{2} < |\alpha(\theta_i, m)| < \frac{3\pi}{2}$

in Eq. 6.21. In this case, the outer boundary point $BP(\theta_i)$ is the 1st pixel, i.e., the pixel corresponding to the minimum valid range $R_{min}(\theta_i)$.

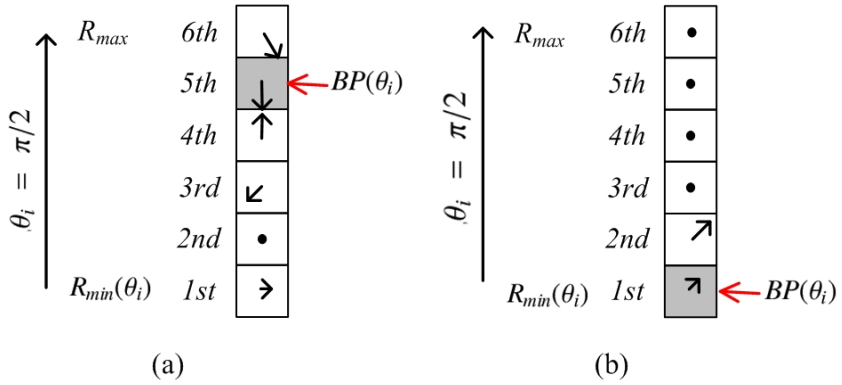

Fig. 6.12. Illustration of the outer boundary point detection on a given radial line.

By using the Eq. 6.21, we can estimate accurate halo regions for the melanocytes while reducing the influence of noise. After estimating the outer boundary point on each radial line using the Eq. 6.21, for each nuclei region, the potential halo contour (HC) is estimated by the boundary points as follows:

$$HC = \left\{(x_{BP(\theta_i)}, y_{BP(\theta_i)})\right\}, i = 1, \ldots, k \tag{6.22}$$

$$x_{BP(\theta_i)} = C_x + BP(\theta_i) \times \cos(\theta_i) \tag{6.23}$$

$$y_{BP(\theta_i)} = C_y + BP(\theta_i) \times \sin(\theta_i) \tag{6.24}$$

The estimated halo contours (shown as thick contours) for Fig. 6.9(a) is shown in Fig. 6.9(e) where the contours are superimposed onto the original image. Note that the region within the halo contours excluding the nuclei regions are the halo regions we are looking for. Two more examples of the halo region estimation are shown in Fig. 6.13 (a) and (c), where the melanocytes are label with letter 'M' in the figure.

6.3.2.4 Resolving the Overlapped Regions

In the skin epidermis, the melanocytes and other kind of nuclei are usually clustered with each others. It is observed that in Fig. 6.9(a), two keratinocytes and one

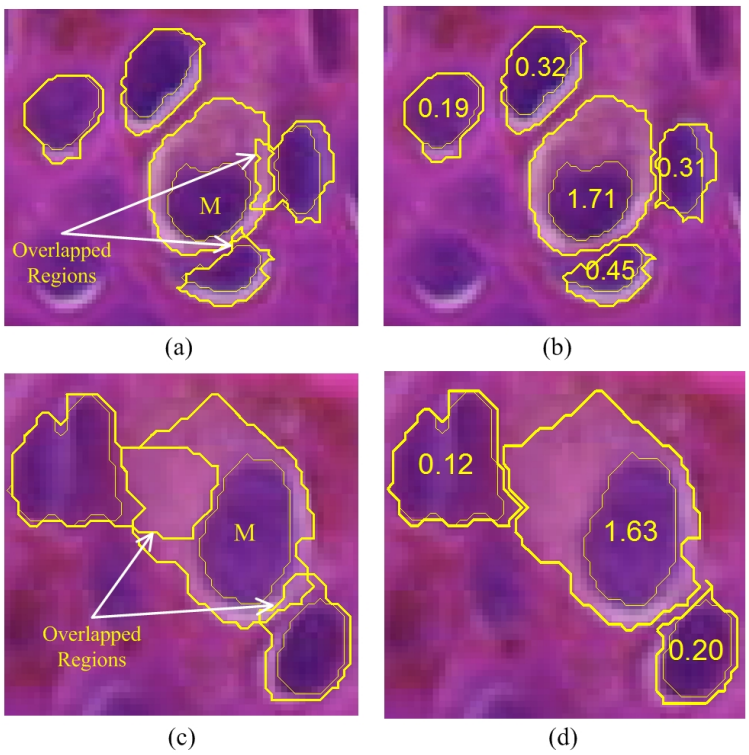

Fig. 6.13. Two examples of halo-like regions estimation. (a) and (c) show the estimated halo regions without resolving the overlap. The nuclei of melanocytes are labeled with letter 'M'. (b) and (d) are the overlap resolved results of (a) and (c), respectively. The value of the parameter R_{HN} discussed in Section 6.3.3 is shown inside the nuclei region as well.

melanocyte (the middle one) are very close to each other. Such proximity will lead to the overlapping of the estimated halo regions (as shown in Fig. 6.9(e)). Such overlapping will result in erroneous detection in the latter processing. Note that the overlapping is due to the spatial closeness of the other nuclei and the halo region. The gradient information of the halo region is falsely captured by the neighboring keratinocytes which are not melanocytes. Generally, the estimated halo regions of the melanocytes have smooth boundaries and larger area compared to that of the other nuclei whereas the estimated halo regions of the other nuclei have non-smooth boundaries (see Fig. 6.9(e), Fig. 6.13(a) and Fig. 6.13(c)). Given an estimated halo contour HC, denote $A(HC)$ and $S(HC)$ as the area inside HC and the smoothness measure of the HC. The smoothness of the HC is calculated as:

$$S(HC) = \frac{1}{k}\sum_{i=1}^{k} |\frac{dBP(\theta_i)}{d\theta_i}|. \tag{6.25}$$

Therefore, the ratio of the boundary smoothness and the area (RSA), i.e., $RSA = \frac{S(HC)}{A(HC)}$, is used as a criterion to resolve the overlapped regions. Specifically, for all the estimated halo regions, we first check if there are overlapped. Assume that two estimated halo regions are overlapped and denote these two estimated halo regions as HC_a and HC_b, respectively. The overlapped region is denoted as $HC_{a \bigcap b} = HC_a \bigcap HC_b$. We resolve the overlap by using the equation as follows:

$$HC_a = \begin{cases} HC_a, & if \ \frac{S(HC_a)}{A(HC_a)} > \frac{S(HC_b)}{A(HC_b)} \\ HC_a - HC_{a \bigcap b}, & Otherwise \end{cases} \tag{6.26}$$

$$HC_b = \begin{cases} HC_a - HC_{a \bigcap b}, & if \ \frac{S(HC_a)}{A(HC_a)} > \frac{S(HC_b)}{A(HC_b)} \\ HC_b, & Otherwise \end{cases} \tag{6.27}$$

Intuitively, for the two halo regions that are overlapped, the one with a higher RSA value will take over the overlapped region whereas the other will lose the the overlapped region. The result of the overlapped region resolving for Fig. 6.9(e), Fig. 6.13(a) and Fig. 6.13(c) are shown in Fig. 6.9(f), Fig. 6.13(b) and Fig. 6.13(d), respectively. It is observed that the melanocytes correctly take over the overlapped regions which reflect the effectiveness of the proposed method.

6.3.3 Detection of the Melanocytes

As described in Section 6.1, the melanocytes generally have associate large halo regions whereas the other nuclei have no such large halo regions. Some halo region estimation results obtained by the RLS algorithm can be observed in Fig. 6.9(f), Fig. 6.13(b) and Fig. 6.13(d). Based on this observation, we can now use the ratio of the estimated halo region area and the nuclei area, denote it as R_{HN}, as a parameter to differential the melanocytes and other nuclei. The ratio R_{HN} is calculated as follows:

$$R_{HN} = \frac{A_{HR}}{A_{NR}} \tag{6.28}$$

where A_{HR} and A_{NR} are the areas of the halo and nuclei regions, respectively. For the melanocyte detection, we select the nuclei regions as the melanocytes if its

R_{HN} value is greater than a predefined threshold $T_{R_{HN}}$. In Fig. 6.9(f), Fig. 6.13(b) and Fig. 6.13(d), the corresponding parameter R_{HN} for each nuclei region is show inside the nuclei region. It is observed that the true melanocytes regions have larger R_{HN} values compare to the other nuclei regions.

6.4 Performance Evaluation

We have evaluated the proposed techniques on 40 different skin histopathology images of epidermis which contains 341 melanocytes. These images are captured under 30× magnification on Carl Zeiss MIRAX MIDI Scanning system.

6.4.1 Evaluation Metrics

6.4.1.1 Evaluation Metrics for Melanocyte Detection

In the melanocytes evaluation, the melanocytes manually identified by an expert are treated as the ground truths positives for the performance evaluation. The other keratinocytes identified by a pathologist are treated as the ground truths negatives. The number of positives and negatives are denoted as N_P and N_N, respectively. We also denote N_{DO} as the total number of detected objects, N_{TP} as the number of true-positives, N_{FP} as the number of false-positives, N_{TN} as the number of true-negative, N_{FN} as the number of false-negative. The true positive rate (TPR, also known as recall rate) and false positive rate (FPR) are defined as follows:

$$TPR = \frac{N_{TP}}{N_{TP} + N_{FN}} \times 100\% \tag{6.29}$$

$$FPR = \frac{N_{FP}}{N_{FP} + N_{TN}} \times 100\% \tag{6.30}$$

The precision rate (PRE) is defined as follows:

$$PRE = \frac{N_{TP}}{N_{DO}} \times 100\% \tag{6.31}$$

6.4.1.2 Evaluation Metrics for Halo Region Estimation

In the RLS based technique, we need to estimate the halo region. The performance of the halo region estimation is crucial for the latter melanocyte detection procedure. For the halo region estimation evaluation, we randomly selected a set of 50 melanocytes and 50 other keratinocytes as the test set. We then manually labeled the boundaries of the halo region of these cells. These manually labeled boundaries are treated as the ground truth and will be compared with the estimation of the halo regions obtained by the proposed RLS technique.

We define GT as the ground truth halo region for each nuclei, EST as the estimated halo region obtained by the proposed RLS technique. Two area-based evaluation metrics: sensitivity ($\mathcal{A}_{SEN}$), precision ($\mathcal{A}_{PRE}$) are defined as follows:

$$\mathcal{A}_{SEN} = \frac{|GT \bigcap EST|}{|GT|} \times 100\% \tag{6.32}$$

$$\mathcal{A}_{PRE} = \frac{|GT \bigcap EST|}{|EST|} \times 100\% \tag{6.33}$$

where $|\cdot|$ is the cardinality operator. We also use another boundary-based evaluation metric: mean absolute distance (MAD) which is defined as follows:

$$MAD(C^{GT}, C^{EST}) = \frac{1}{M}\sum_{i=1}^{M}[min||C_i^{GT} - C_j^{EST}||] \tag{6.34}$$

where C^{GT} and C^{EST} are the contour/boundary of the ground truth region and estimated region, respectively. C_i^{GT} and C_j^{EST} represent the ith pixel and the jth pixel on the contour of the ground truth region and estimated region, respectively. M is the total number of pixels on the contour of the ground truth region.

6.4.2 Parameters Selection

6.4.2.1 Parameter Selection for the LDED based technique

To obtain good performance, two parameters that will be used in the proposed LDED based technique need to be selected appropriately. These parameters are τ_E and τ_D (τ_E is for the ellipticity measure and τ_D is the distance of two fit Gaussian models). In order to calculate the parameter τ_E and τ_D, two of the images are selected. In these two images, 50 melanocytes are manually labeled, and the value of e_E and e_D for each melanocyte is calculated. We then performed the trail-and-error test, the parameter τ_E and τ_D which achieved the best PRE and SEN are selected as the parameter τ_E and τ_D for the proposed technique (specifically, $\tau_E = 0.8$ and $\tau_D = 34$). These two parameters are then used for the performance evaluation on the remaining images.

6.4.2.2 Parameter Selection for the RLS based technique

To obtain good performance, two parameters that will be used in the proposed RLS based technique need to be selected appropriately. These parameters are R_{max} (the maximum range of the radial line), and $T_{R_{HT}}$ (the predefined threshold for discrimination of the melanocytes and other nuclei). For the parameter R_{max}, we chose a set of 20 manually labeled melanocytes and measure the distances from the centroid to the boundary points in each melanocyte. Let the maximum distance be denoted by $dist_{max}$, we then chose the R_{max}=2*$dist_{max}$. Based on the biological knowledge, the size of the nuclei in skin epidermis should fall within a desired range. The choice of the R_{max} is to ensure that the radial line can reach all the melanocytes and the surrounding halo regions. For determining the parameter $T_{R_{HT}}$, two images are selected and the nuclei and their halo regions within these images are manually labeled. In addition, the value of R_{HN} is calculated for each nucleus. We then perform the trail-and-error test, i.e., we use a set of possible values for $T_{R_{HT}}$ (from the minimum value of all the R_{HN} to the maximum value of all the R_{HN} in the test images) to calculate the PRE and chose the value that achieves the best PRE as the

parameter $T_{R_{HT}}$. The determined value of R_{max} (R_{max}=35), and $T_{R_{HT}}$ ($T_{R_{HT}}$=0.8), are then used for the evaluation.

6.4.3 Evaluation on Halo Region Estimation

Since we use the ratio of the estimated halo region area and the nuclei area, R_{HN} defined in Eq. 8.5, as a criterion for the melanocyte detection, the estimation of the halo region of the nuclei is important for the proposed RLS based technique. In this section, we evaluate the performance on the estimation of halo region.

The halo region estimation performance is shown in Table 6.1. The average value of all the three evaluation metrics for melanocytes and other nuclei are shown in the second row and the third row of Table 6.1, respectively. It is observed that the proposed RLS technique is able to estimate the halo region of the nuclei correctly. This is expected to provide a good performance in the melanocytes detection.

TABLE 6.1
PERFORMANCE EVALUATION OF THE HALO REGION ESTIMATION.

	$\mathcal{A}_{SEN}$	$\mathcal{A}_{PRE}$	MAD
Melanocytes	84.69%	93.80%	1.51 pixels
Other keratinocytes	86.29%	96.16%	0.72 pixels

A few examples of the estimated halo regions for the melanocytes (the first row) and other nuclei (the second row) are shown in Fig. 6.14. In each image, the interested nuclei are put in the middle of the images and their halo regions are shown as the contours. The dotted contours represent the estimated halo regions obtained by the proposed RLS technique whereas the solid contours are the manually labeled halo regions. In the case of melanocytes (Fig. 6.14(a)-(d)), the halo regions are much larger than the nuclei regions. In the case of other keratinocytes (Fig. 6.14(e)-(h)), the estimated halo regions are very close to the nuclei boundary, which is desired since there is little or no halo region for other keratinocytes. The proposed RLS technique is able to estimate the halo region correctly, with minor distortions compared to the manually labeled halo region (see Fig. 6.14(a)-(c), (e)-(h)). These

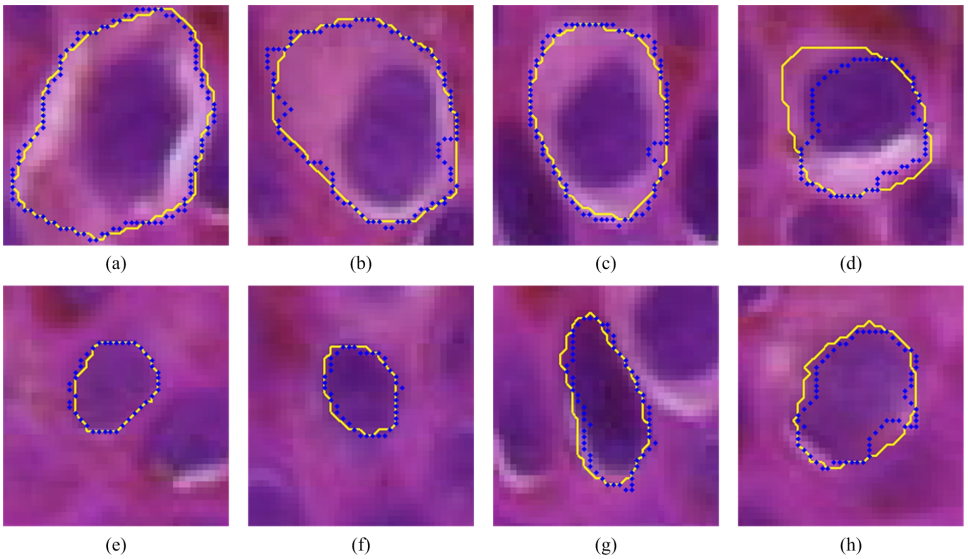

Fig. 6.14. Examples of the estimated halo regions compared to manually labeled halo regions for melanocytes and other keratinocytes. The first and second row show the melanocyte examples and other keratinocytes examples, respectively. The dotted contours represent the estimated halo regions obtained by the proposed RLS technique whereas the solid contours are the manually labeled halo regions.

minor distortions will not degrade the final melanocytes detection performance since we will use the region ratio criterion R_{HN} (described in Eq. 8.5) to differentiate the melanocytes and other keratinocytes. In Fig. 6.14(d), due to the staining variation, a considerable amount of the halo region cannot be recovered by the proposed RLS technique. This might lead to a miss detection of this melanocyte since the region ratio R_{HN} will have a small value.

6.4.4 Quantitative Evaluation on Detection

Since this is the first technique to solve the melanocytes segmentation problem, there is no other equivalent technique in the literature that can be compared with the two proposed techniques. Therefore, we compare the proposed techniques with a possible alternative technique, known as template matching (TM). Note that the TM technique is a widely used technique for pattern detection in medical imaging [45], [46]. A set of 30 templates are designed to capture the ”MPattern” and selected 10 templates are shown in Fig. 6.15. The templates are designed according

to 30 manually selected melanocytes. Note that we design 30 templates with different sizes in terms of the template size (15×15, 20×20 , and 25×25 pixels), center heart radii (8, 9, 10, 11, and 12 pixels), and the ring thickness (2, and 3 pixels), in order to create the variations. The intensity for the heart of the template and the ring of the template are assigned according to the mean value on the corresponding regions in the 30 samples of manually selected melanocytes. In the TM implementation, each template is first applied on the image by using the normalized cross correlation (NCC) [79]. Denote the NCC output of the ith template as O_i, and the 2-D coordinate in the image as (u, v). The potential pixel (u, v) belong to the melanocyte region $J_i(u, v)$ obtained from the ith template is as follows:

$$J_i(u,v) = \begin{cases} J_i(u,v) & if\ O_i(u,v) \geq 0.80 \\ 0 & otherwise \end{cases} \tag{6.35}$$

The accumulated map O_{acc} for all 30 templates are calculated as follows:

$$O_{acc} = \sum_{i=1}^{30} \sum_{(u,v)\in\Omega} J_i(u,v) \tag{6.36}$$

where Ω represents the image domain. The final result is a binary image which is determined using a threshold T_{TM} on O_{acc}.

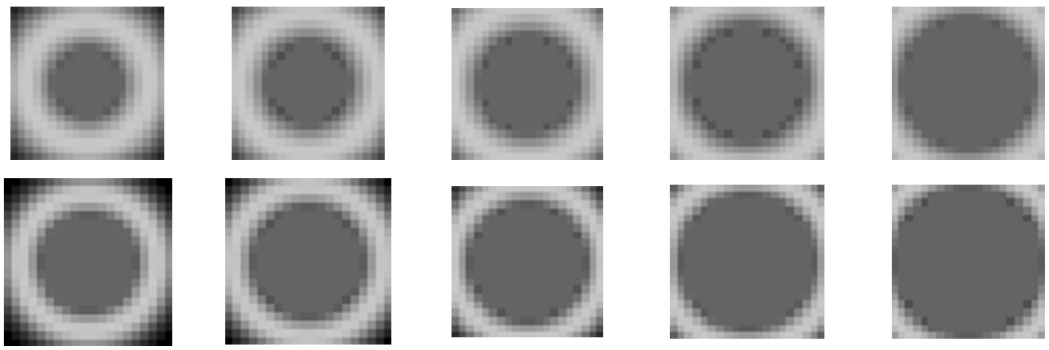

Fig. 6.15. Ten templates with size 20×20 used in the template matching techniques. Note the variation of the center heart radii and the ring thickness. The templates are magnified for demonstration purpose.

The performance of the proposed techniques, the LDED and the RLS based

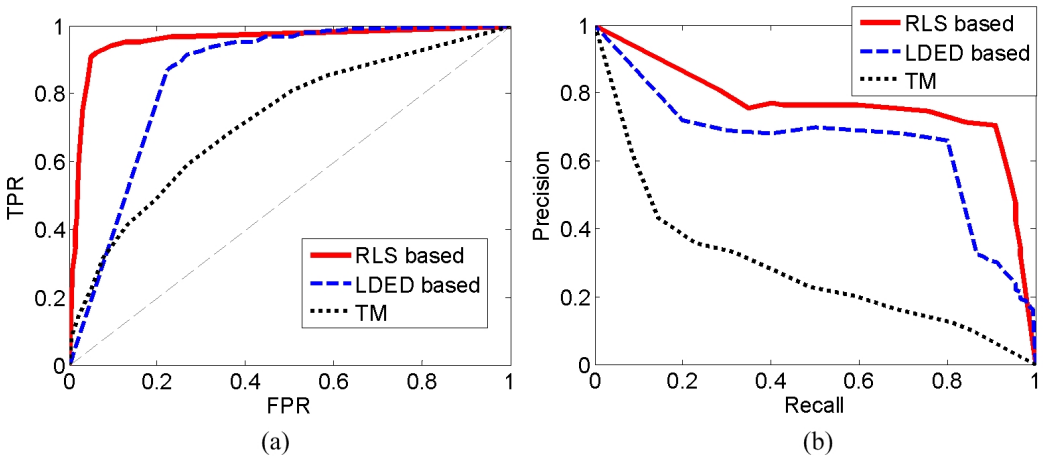

Fig. 6.16. The ROC and PRC curves of the proposed techniques and the TM technique. (a) the ROC curve. (b) PRC curve.

techniques, are evaluated using the Receiver Operating Characteristic (ROC) and the Precision-Recall Curve (PRC). The ROC and PRC curves of the proposed techniques and the TM technique are shown in Fig. 6.16. The ROC and PRC curves of the proposed LDED based technique are generated by varying the parameter τ_D from to 30 to 50 with a step of 1. The ROC and PRC curves of the proposed RLS based technique are generated by varying the parameter $T_{R_{HN}}$ from to 0 to 2 with a step of 0.1. The ROC and PRC curves of the TM technique are generated by varying the parameter T_{TM} from to 0 to 1 with a step of 0.1. It is noted that in the ROC curve, the curve that is close to the upper left corner is better than that is far away from the upper left corner.

It is observed from Fig. 6.16(a) that the proposed LDED based technique is able to provide 86% TPR with 80% FPR, whereas the proposed RLS based technique is able to provide the TPR around 90% with the FPR at 95%. As for the TM technique, the TM technique provide a poor performance because it is difficult to distinguish the melanocytes from other nuclei by using the templates. In the case of the PRC curve, the curve that is close to the upper right corner is better than that is far away from the upper right corner. In Fig. 6.16(b), it shows that the proposed LDED based is able to provide 80% recall rate with around 40% precision rate.

RLS based technique can provide 90% recall rate with around 80% precision

rate. As for the TM technique, it usually generate a large number of false detections (results in low precision rate) because the pattern of the other cytological components are very similar to the templates. It is observed from both ROC and PRC curves that the proposed technique provides a superior performance compare to the TM technique. Note that the template matching technique is a general technique for the object detection problem, and it could not be expected to provide a better performance compared to a specifically designed technique. Since there is no other available technique for the task at hand, i.e., melanocytes detection in the skin epidermis, we used the TM technique with specifically design templates as the baseline technique for the comparison.

6.4.5 Qualitative Evaluation on Detection and Segmentation

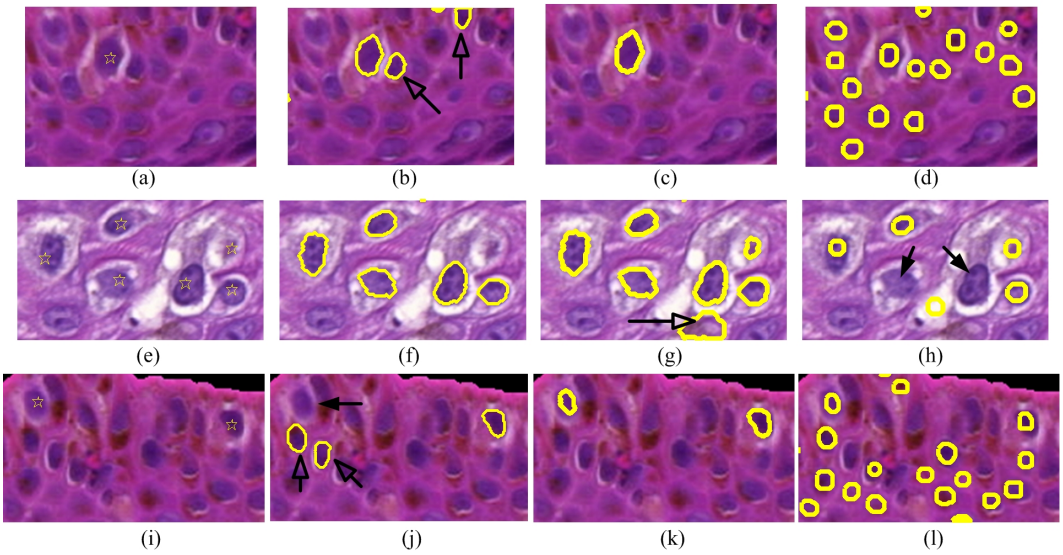

Fig. 6.17. Three examples for qualitative evaluation. The first column ((a), (e), and (i)) show three original color histopathological images. The manual labeled melanocytes locations are indicated by stars. The second, third, and fourth columns show the results provided by the proposed LDED based technique, RSL based technique, and TM technique, respectively. Note that segmented regions are presented as the thick contours. The solid arrows indicate the miss detection whereas the hollow arrows indicate the false detection.

For the qualitative evaluation, three close-up examples are shown in Fig. 6.17. These images are captured from different skin tissues, and the parameter $\tau_D = 34$, $T_{R_{HN}} = 0.8$ and $T_{TM} = 0.2$ were used for the proposed LDED based technique,

RLS based technique and the TM technique, respectively. Fig. 6.17 (a), (e), and (i) show three original color histopathological images, where the manual labeled melanocytes locations are indicated by stars. The last three columns show the results obtained using the proposed LDED based technique, RLS based technique and the TM technique, respectively. The detected regions are presented as the thick contours. The proposed LDED based technique (shown in Fig. 6.17 (b), (f), and (j)) is able to detect most of the melanocytes in the images with some of the false positives (indicated by hollow arrows). These false positives usually present in the vicinity of a typical melanocyte where its surrounding cytoplasm are retracted. The hallow regions are mistakenly included into the LDED, which result in the false positives. The proposed RLS based technique (shown in Fig. 6.17 (c), (g), and (k)) can detect all the melanocytes and has only one false positive (In Fig. 6.17(g)). The proposed RLS based technique resolves the overlap issue very well, therefore there is less false positives in the final result. In the results provided by the TM technique, we can observe many false detections (shown in Fig. 6.17 (d), (h), and (l)) since there are many cytological components similar to that of the templates. In addition, because it is very difficult to model a good template set that can capture the size and shape variations of the natural melanocytes, it misses some of the ground truths melanocytes (see shown in Fig. 6.17 (h), the solid arrows indicate the miss detection). Overall, the two proposed techniques are able to provide a good performance, where RLS based technique is the best, in the test images set.

6.4.6 Comparison of LDED and RLS Complexity

In the LDED technique, there are two main steps: the ellipse fitting and parameter estimation of the MoG model. The halo regions are estimated in a coarse manner using the enlarged fitted ellipse. In the RLS technique, however, the surrounding area of each nuclei, i.e., the halo regions, are estimated using a more sophisticated technique. For each nuclei, a set of radial lines are generated, and the cost function, shown in Eq. 6.19, is evaluated for every point on the radial line in order to determine the outer boundary of the halo region. This is the most time-consuming

part of the RLS technique. It is difficult to compare the complexity of these two techniques in terms of number of arithmetic operations, since it depends on several factors, such as the number of objects in the image, the number of pixels for each object and its boundary. Therefore, we have compared the complexity in terms of the processing time. These two techniques were implemented in MATLAB 7.04 and were run on a 2.4 GHz Intel Core II Duo CPU with 3GB RAM using . The comparison of LDED, RLS, and TM techniques in terms of processing time is shown in Table 6.2. The detection performance in terms of the area under the curve (AUC) for the ROC is also shown in Table 6.2. The AUC is a measure for the ROC curve, where the best performance is achieved when the AUC is equal to 1. To segment the melanocytes from a 512 $\times$ 512 pixels RGB color image, the proposed LDED technique and the RLS technique on average take 6 seconds and 23 seconds, respectively. On the other hand, the TM technique takes 3 seconds to detect the melanocytes in the image. Even though the proposed two techniques take more processing time, the performance is much superior compared to the TM technique, the AUC of the LDED and RLS technique is 0.85 and 0.95, respectively. Note that the RLS technique takes 4 times more processing time than the LDED technique. However, the accurate estimation of the halo region in the RLS technique helps to achieve a better performance compared to that in the LDED technique.

TABLE 6.2
COMPARISON OF LDED, RLS, AND TM TECHNIQUES IN TERMS OF PROCESSING TIME.

Techniques	Processing Time	AUC
TM	3 sec.	0.72
LDED	6 sec.	0.85
RLS	23 sec.	0.95

6.5 Summary

In this chapter, we discuss the importance of the melanocytes detection in the skin epidermis area. Two computerized techniques are proposed to detect and seg-

ment the melanocytes automatically. The evaluation using 40 histopathological images (with more than 300 melanocytes) shows the efficiency of the proposed techniques. However, note that in some malignant melanoma case, the nuclei of melanocytes are enlarged. In this situation, the proposed RLS based technique will reject the true melanocytes. To solve this issue, a threshold base on the size of nuclei can be applied to enhance the robustness of the proposed RLS-based technique.

Chapter 7

Detection of Mitotic Cells [1]

7.1 Introduction

Recently, image processing and pattern recognition techniques has been widely applied in histopathological images [23], [49]. These computer-aided techniques are aim to detect the interested biological markers in order to assist the final cancer grading. Mitotic count is an important parameter in cancer grading and detection [80]. Traditionally, a pathologist analyzes the biopsy slide manually by using high power microscopy. The mitotic cells are annotated manually at each view and the total mitotic count is used as a critical factor for the cancer grading, since the mitotic count reflects the aggressiveness of the tumor.

There are five main phases in the mitosis: interphase, prophase, metaphase, anaphase and telophase. Examples of all five phases from the hematoxylin and eosin (H&E) histopathological images are shown in Fig. 7.1 [81]. It is observed that the shapes of the nucleus (the darker region) are different at different phases of the mitosis. From the interphase to metaphase (the first, second and the third columns in Fig. 7.1), the shape of the nucleus is changed from large rounded to the narrow long. In anaphase and telophase (the fourth and fifth columns in Fig. 7.1),

[1] A version of this chapter has been accepted for publication. Cheng Lu, Mrinal Mandal, "Towards Automatic Mitotic Cells Detection and Segmentation in Multi-spectral Histopathological Images", *IEEE Journal of Biomedical and Health Informatics*. 2013.

two groups of chromosomes are drawn apart. In the last stage (i.e., the telophase), a mitotic cell has two distinct nuclei, but they are not yet full individual cells.

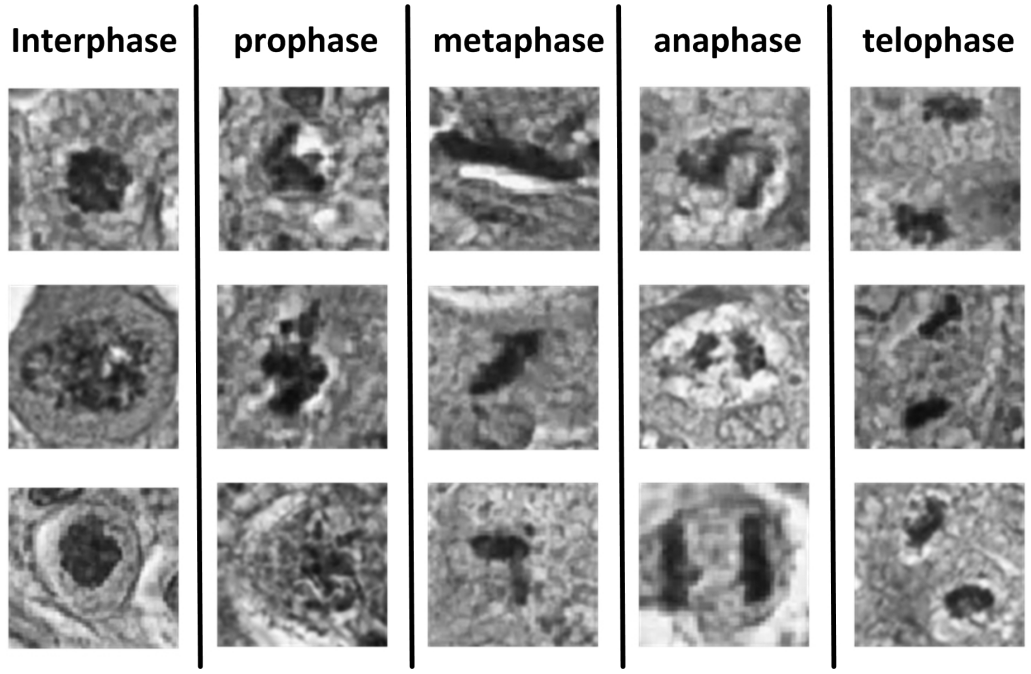

Fig. 7.1. Examples of MCs in 5 mitotic phases (images are obtained from reference [81]). Each column shows three examples of mitotic cells for each mitotic phase. The images are cropped from the original image captured under 40× magnification. The images have been expanded or shrunk for illustration purpose.

Besides the variations of the appearance in different mitotic phases, there is a large number of other cytological components (OCC) in a typical image which makes the automatic detection of mitotic cells (MC) difficult. In a high power field (HPF, size 512×512 μm^2) at 40× magnification, there might be only 1-10 MCs, or even none. However, there will be more than 30 times of OCC in the HPF which greatly influence the detection of the real MCs. Fig. 7.2 shows an example of the MC in a portion of a HPF image captured at 40× magnification. The locations of the MCs are denoted by the thick rectangles. It shows that a large number of OCCs are also present in the image and are similar to the MCs in terms of appearance and size.

Detection of mitotic cell in the traditional H&E stained histopathological image is a very challenging task since mitotic cells (MC) are small objects with a

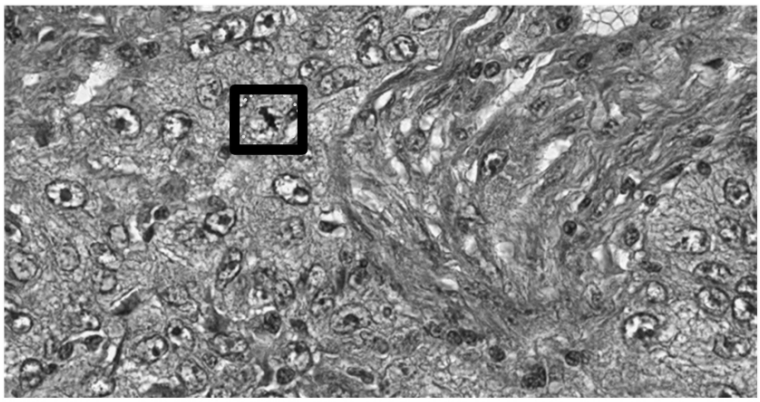

(a)

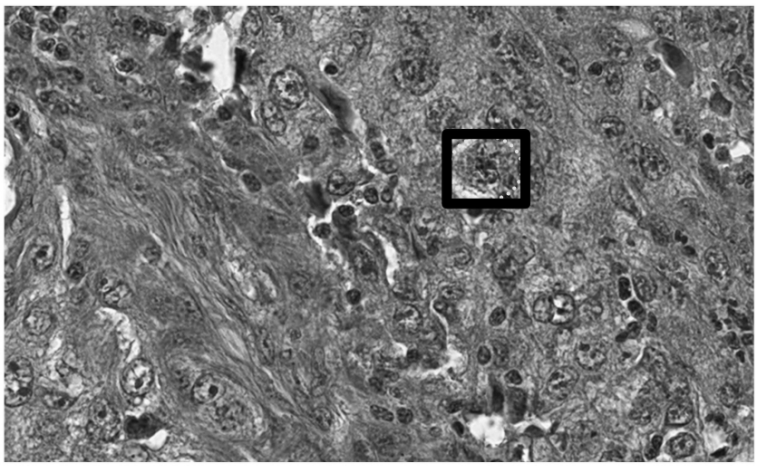

(b)

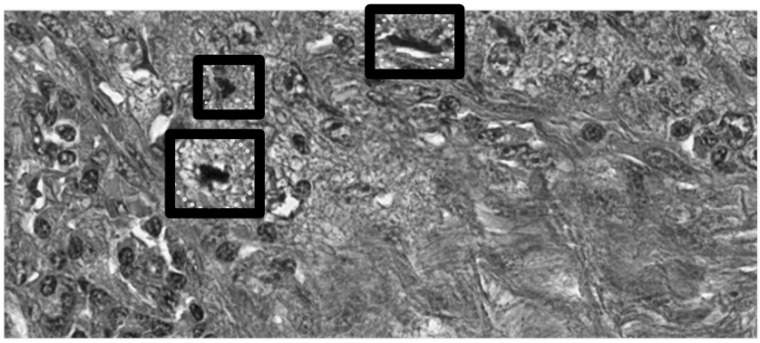

(c)

Fig. 7.2. Three examples of the MC in a portion of a HPF image captured at 40× magnification. There are one, one, and three MCs in (a), (b), and (c), respectively. The locations of the MCs are denoted by the thick rectangles. Note that there is a large number of OCCs in the image as well.

large variety of shape configurations. In addition, the wide variation in intensity information due to the staining differences and a large number of cytological components which are highly similar to the MC in terms of the color and morphological appearances make the automatic detection of MC difficult.

The first attempt to detect the MCs in traditional H&E stained histopathological images is done by Sertel et al. [30]. Sertel et al. proposed an automatic technique for detection of the mitosis and karyorrhexis cells (MKC) in digitized neuroblastoma histological images. The schematic of this detection technique (henceforth referered to as the DMKC technique) is shown in Fig. 7.3. Three color channels, R, G, and B are used in this technique. In the preprocessing step, the image quality is enhanced using histogram equalization and anisotropic diffusion. After the preprocessing, this technique calculates the posterior map of the MKC based on the pre-labeled image. A two-step thresholding method is then used to provide the final detection result. Note that this technique does not differentiate between the mitotic cells and the karyorrhexis cells which have similar appearance.

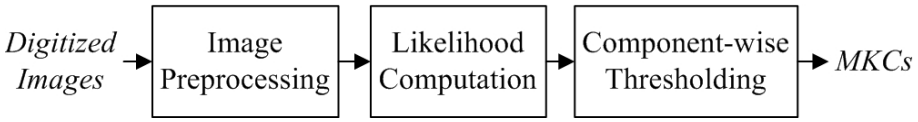

Fig. 7.3. The schematic of the DMKC technique.

Schlachter et al. [82] proposed to use harmonic filtering (HF) for the cells in metaphase of mitosis detection in Colorectal cancer under the microscope. In this work, special staining was used such that the background pixels were black and the nuclei pixels were dark blue. If a nuclei is in mitotic metaphase, many bright green dots will be present in the nuclei area. In this work, the blue channel and green channel images are used. The HF first project the features (such as intensity values and gradients) extracted from local windows onto local harmonic descriptors. The local harmonic descriptor are then combine to generate the output. Note that in the traditional H&E stained image, the MCs will not have special staining on it. The OCCs may have similar appearance with that of MCs. Therefore, the HF is not

suitable in the task at hand.

Several automatic mitosis detection techniques also have been proposed for phase contrast microscopy, where a sequence of gray level images is captured in time [83], [84]. In the phase-contrast time-lapse image, the mitotic activities can easily be monitored along the time axis. These techniques use a conditional random field-based spatio-temporal probabilistic model to detect the changes between different time frames where the mitotic activities occur.

A summary of the existing techniques for mitosis detection can be found in Table 7.1. The second column shows if this technique is applied in the traditional H&E stained images. The third column shows the number of spectral channels (NSC) used in the technique. The fourth column shows if time information can be used. The last column shows the characteristics of the MCs in the image. Note that the DMKC and proposed techniques can be applied to the traditionally used H&E staining images without any special marker on the MCs.

TABLE 7.1
COMPARISON OF THE EXISTING MC DETECTION TECHNIQUES. (NSC:NUMBER OF SPECTRAL CHANNELS; TI:TIME INFORMATION.)

Authors	H&E	NSC	TI	Characteristics of MCs
Sertel ea al. [30]	Yes	3	No	MCs and OCCs have similar appearances
Schlachter ea al. [82]	No	2	No	Special markers (bright green dots) on MCs
Huh ea al. [84]	No	1	Yes	Mitotic activity can be observed along time axis
The proposed	Yes	10	No	MCs and OCCs have similar appearances

As shown in Table 7.1, researchers have used multiple channels image to detect the MCs (up to 3). Better performance is expected to be obtained by introducing more spectral channels. Multi-spectral imaging has been successfully used in many applications, such as MR image classification [85], Iris detection [86], Chemometrics [87], satellite image classification [88]. In order to classify the multi-spectral MR images, Lin et al. [85] first use a fuzzy-set process to generate a set of potential targets as the training set. The linear discriminant analysis (LDA) is then employed to perform the classification. Chen et al. [86] proposed a technique for liveness detection in iris multi-spectral images. In this technique, a set of features are ex-

tracted from the multi-spectral images, followed by the classification using support vector machine. In order to utilize the multi-spectral images in an efficient way, principal component analysis (PCA) is widely used for the feature selection and dimension reduction [87]. By selecting a certain number of principal components, the main features can be extracted from the high dimensional space for better analysis. However, it is noted that the determination of the principal components to be extracted is a difficult task. Some of the important features of interest may be related to the low variance and some other unrelated signal may be treated as the principal component. Recently, multi-spectral images analysis have been introduced into the histopathology [89]. It has high potential to be used in efficient MC detections.

In this chapter, we propose an efficient technique for automatic detection of the mitotic cell in static multi-spectral H&E stained histopathological images. In the proposed technique, a discriminative image is first generated using linear discriminant analysis. The intact MC candidate areas are obtained using local region threshold and a set of features are extracted from candidate regions and their local areas. The final MC regions are finally determined using a multiple-expert decision system. The proposed computer-aided technique will be able to help the pathologists to focus on a small number of regions that are highly likely to be the MCs in traditionally used image and to reduce the workload of the pathologists.

7.2 The Proposed Technique

A brief review of existing techniques have been presented in Section 7.1. In this work, our goal is to develop an efficient technique for detecting and segmenting the MCs in H&E stained histopathological images. The objective of this work is similar to that of the DMKC technique. The proposed technique uses several novel approaches to improve the performance. For example, in the DMKC technique, the likelihood is computed for all three channels, and are then combined by computing their product in the Bayesian equation. In this way, the information unrelated to the MCs maybe included and will lead to lower discriminant. In the proposed tech-

nique, we use a different approach where the whole multi-spectral image space is projected into a single discriminant image using LDA. Another important difference is that the DMKC technique uses a two-step threshold to determine the final MKC regions, and does not differentiate between mitotic cells and karyorrhexis cells. In the proposed technique, the intact regions of the MC candidates are obtained by the Bayesian modeling and a local region threshold method in DI space. The final MCs are determined using a multi-expert system which considers the imbalanced classes distribution.

The schematic of the proposed technique is shown in Fig. 8.1. It is observed that the proposed technique consists of three main modules. In the first module, a single channel image, named discriminative image (DI) is generated from the multi-spectral images, in which the discrimination between MCs and OCCs, in terms of the intensity, is maximum. In the second module, the MC candidates are first detected and their intact nuclei regions are segmented in the image. In the last module, all segmented candidate regions are analyzed in a classification framework, and the final detected MC regions are obtained. The details of the modules are presented below.

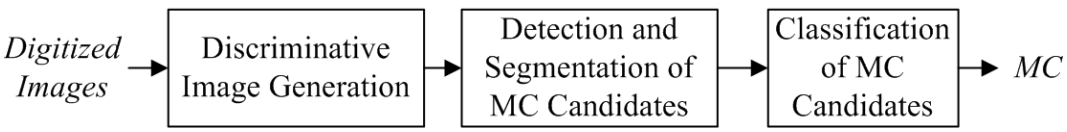

Fig. 7.4. The overall schematic of the proposed technique.

7.2.1 Discriminative Image Generation

The images with the 10 different spectral bands (details about the spectral bands can refer to Table 7.3) contain more biological signals than a single spectral image or the RGB image (three spectra), which will help us to identify the mitosis. However, we need to find a way to combine these 10 bands spectral images and perform the MC detection. Linear Discriminate Analysis (LDA) technique [78] is a supervised technique widely used in multi-label data analysis, pattern recognition and classi-

fication [85], [90]. The LDA aims to find a projection of the high dimension data into a lower dimension space such that the best discriminant between two or more classes are achieved. In this chapter, the LDA technique is employed to find an optimal linear combination of the available multi-spectral images. In this way, the multi-spectral images are combined and a discriminative image is generated such that the MCs and other cytological components have the largest discrimination in terms of the intensity value. The optimal linear combination will then be used to generate the DI for each unseen multi-spectral images set for further analysis. The DI is generated using the following equation:

$$I_D = \mathbf{AI} = [a_1, \ldots, a_K][I_1, \ldots, I_K]^T = \sum_{i=1}^{K} a_i I_i \tag{7.1}$$

where I_i is a spectral image (i is the spectral index), a_i is the coefficient for each spectral image, and K is the number of spectral bands.

Denote the pixels belonging to MC as class ω_1, the pixels belonging to other nuclei regions as class ω_2. Let the mean intensity of all pixels in ω_1 and ω_2 in the ith spectral image be denoted as m_{1i} and m_{2i}, respectively. Let the variant of all pixels in ω_1 and ω_2 in the ith spectral image be denoted as σ_{1i}^2 and σ_{2i}^2, respectively. We will have $1 \times K$ mean vectors and variant vectors as follows:

$$\mathbf{M}_1 = [m_{11}, m_{12}, \ldots m_{1K}] \tag{7.2}$$

$$\mathbf{M}_2 = [m_{21}, m_{22}, \ldots m_{2K}] \tag{7.3}$$

$$\mathbf{\Sigma}_1 = [\sigma_{11}^2, \sigma_{12}^2, \ldots \sigma_{1K}^2] \tag{7.4}$$

$$\mathbf{\Sigma}_2 = [\sigma_{21}^2, \sigma_{22}^2, \ldots \sigma_{2K}^2]. \tag{7.5}$$

Based on Fisher's discrimination criterion [65], the optimal coefficient vector A^* can be obtained by maximizing the separation criterion as follows:

$$\delta = \frac{|\mathbf{A}^T\mathbf{M}_1 - \mathbf{A}^T\mathbf{M}_2|^2}{\mathbf{A}^T(\mathbf{\Sigma}_1 + \mathbf{\Sigma}_2)\mathbf{A}} \tag{7.6}$$

In other words:

$$\mathbf{A}^* = \arg_{\mathbf{A}} \max \left[\frac{|\mathbf{A}^T\mathbf{M}_1 - \mathbf{A}^T\mathbf{M}_2|^2}{\mathbf{A}^T(\mathbf{\Sigma}_1 + \mathbf{\Sigma}_2)\mathbf{A}} \right] = \arg_{\mathbf{A}} \max \left[\frac{\mathbf{A}^T(\mathbf{M}_1 - \mathbf{M}_2)^2\mathbf{A}}{\mathbf{A}^T(\mathbf{\Sigma}_1 + \mathbf{\Sigma}_2)\mathbf{A}} \right] \quad (7.7)$$

It can be shown that the optimal coefficient vector A^*, as given in Eq. 7.7, can be obtained by the solving the general eigenvalue problem as follows [78]:

$$(\mathbf{\Sigma}_1 + \mathbf{\Sigma}_2)^{-1}(\mathbf{M}_1 - \mathbf{M}_2)\mathbf{A} = \lambda\mathbf{A} \quad (7.8)$$

where λ is the eigenvalue. In the proposed technique, we manually label a set of randomly selected MC (class ω_1) and other non-MC regions (class ω_2) as the training data (these training data will be used for the second and third modules as well). The mean intensity and the variance values for these two classes in the ten spectral images are calculated in order to find the optimal coefficient vector $\mathbf{A}^*$ using Eq. 7.8. The optimal coefficient vector $\mathbf{A}^*$ we obtained by using five sets of the multi-spectral images are as follows:

$$\mathbf{A}^* = [-5.16, -2.78, 7.41, -6.53, 0.58, -0.03, -0.01, 2.52, 1.16, 3.83]. \quad (7.9)$$

The DI can now be generated by using the equation as follows:

$$I_D = \mathbf{A}^*\mathbf{I} \quad (7.10)$$

The DI can provide better discriminant between the MC and other nuclei regions which will help in the latter segmentation and classification procedures. An example is shown in Fig. 7.5. Fig. 7.5 (a) to (j) show all 10 spectral image for a certain HPF. The DI is shown in Fig. 7.5 (k). The corresponding value of the objective function δ for each image is shown in (l). It is observed in Fig. 7.5(l) that the DI provides a superior discrimination between the MC and non-MC classes compared to individial spectral channel. This is also observed in Fig. 7.5(k), where

two MCs (pointed by arrows) are easier to be differentiated from other cytological components.

7.2.2 Detection and Segmentation of MC Candidates

The goal of this module is to detect and segment the MC candidates regions. The schematic of this module is shown in Fig. 7.6. It is observed that there are three steps in this module, which are discussed in more details in the following.

7.2.2.1 Bayesian Modeling for Posterior Map Generation

At first, the training set of the MC is utilized to build the probability density function (pdf) in terms of the intensity in the DI space.

Denote a pixel as x, and its intensity value as $f(x)$. Using the Bayesian theorem, the posterior is calculated as follows:

$$P(\omega_j|f(x)) = \frac{p(f(x)|\omega_j)P(\omega_j)}{p(f(x))} \tag{7.11}$$

where ω_j, $j \in 1, 2$, indicates the class label of the pixel. Class ω_1 corresponds to the MC regions, and class ω_2 corresponds to the remaining pixels in DI. The likelihood function $p(f(x)|\omega_j)$ indicates the probability of certain pixel intensity value given a certain class ω_j. The prior $P(\omega_j)$ indicates the proportion of different classes present in the image. The likelihood term $p(f(x)|\omega_j)$ is determined using the training data. Given a pixel from the unseen image, the posterior probability $P(\omega_j|f(x))$ that a pixel belongs to class ω_j given intensity value $f(x)$ can be calculated using Eq. 7.11. In this work, we aim to detect the pixels in the DI that belongs to the MC area. For each pixels in the DI, the posterior for class 1 (ω_1) is calculated as follows

$$P(\omega_1|f(x)) = \frac{p(f(x)|\omega_1)P(\omega_1)}{p(f(x))} \tag{7.12}$$

The posterior of each pixel will form a posterior map (PM), denoted as M_p. An example is show in Fig. 7.7(a) to (c). The DI is shown in Fig. 7.7(a). Fig. 7.7(b)

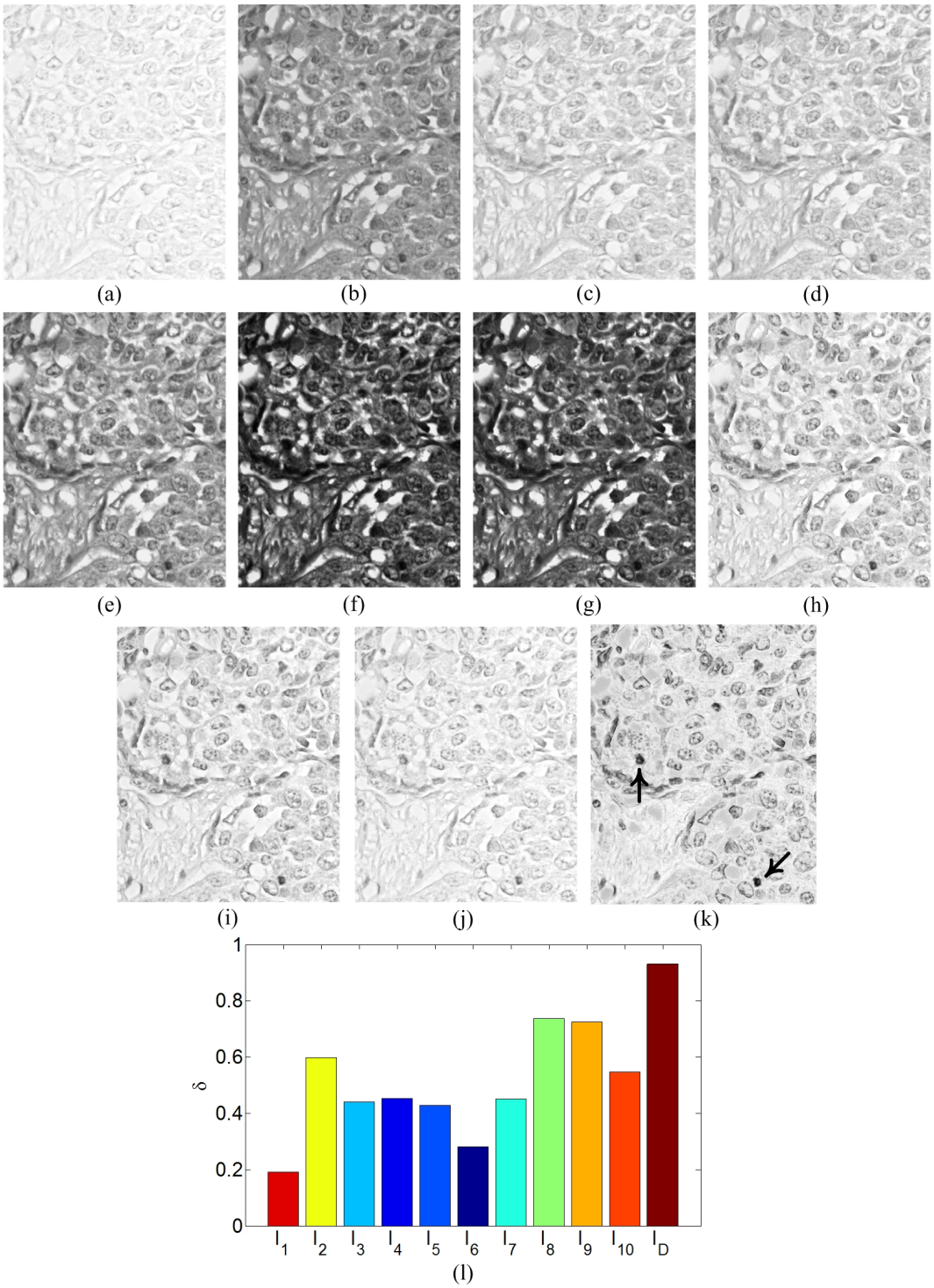

Fig. 7.5. An example of all 10 band spectral images((a) to (j)) and the DI ((k)). In the image, there are two MCs which are pointed by arrows (see (k)). The corresponding value of the objective function δ for each image is shown in (l).

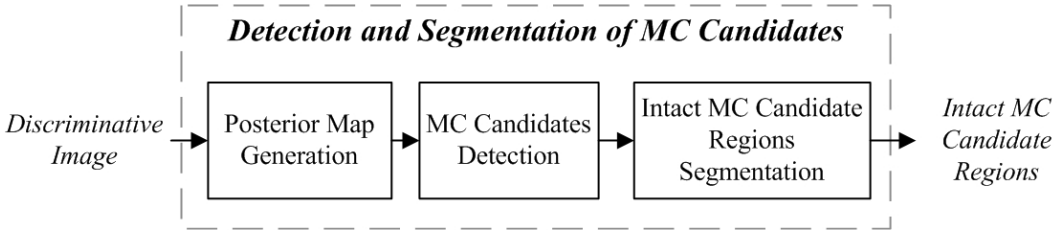

Fig. 7.6. The schematic of module 2.

shows the pdf of MC (class ω_1) and non-MC regions (class ω_2) in terms of intensity values in DI. Fig. 7.7(c) shows the PM where the bright regions (with posterior $\approx$ 1) indicate the high posterior.

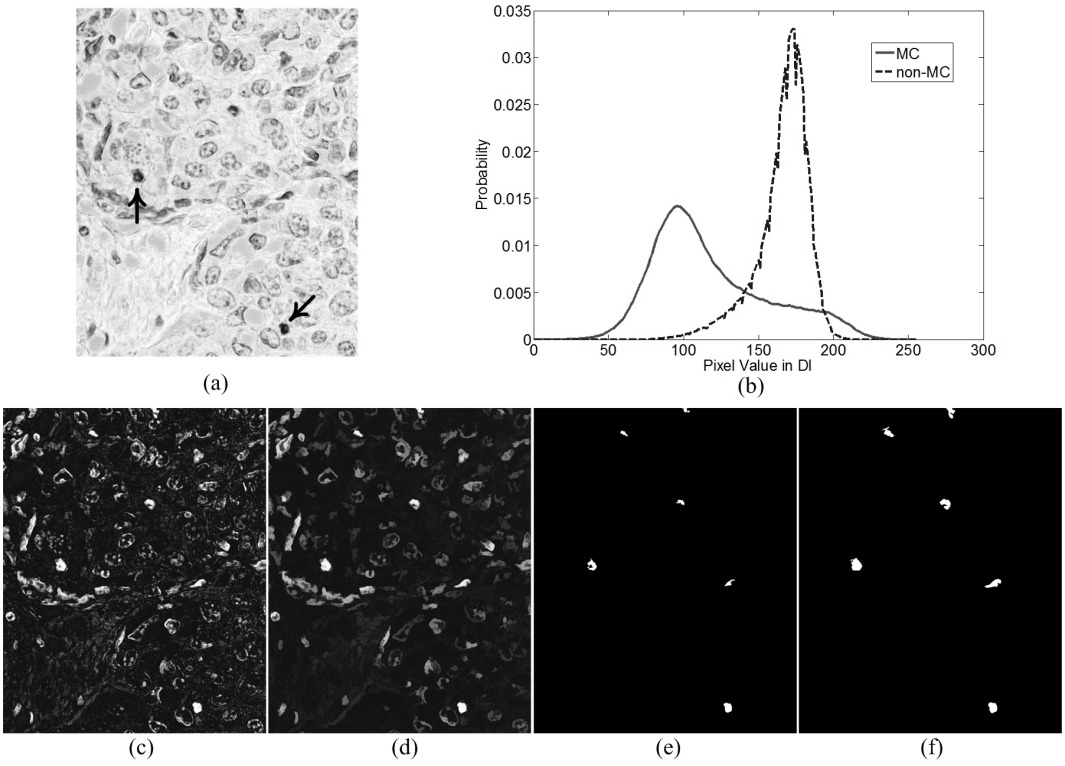

Fig. 7.7. The example of the MC candidates detection and intact region segmentation. (a) the DI. (b) the pdf of MC and non-MC regions from the training set. (c) the posterior map M_p. (d) the homogenous posterior map M_h. (e) the map M_t which contains potential MC regions. (f) the map which contains all intact MC candidate regions.

7.2.2.2 MC Candidates Detection

In a histopathological image, there might exist non-MC noisy pixels whose values are similar to that in the MC regions. This is reflected in Fig. 7.7(c) where many unrelated pixels (pixels not belonging to the MCs) have high posterior values because their intensity values are close to those in the MC regions. In order to remove these noisy pixels and achieve better segmentation result, we propose to smooth the PM so that the true MC regions are homogenous while the posterior of the noise regions are suppressed. A hybrid gray-scale morphological reconstruction method (HGMR)[21] is applied. The HGMR method has two steps. At first, the *Opening-by-Reconstruction* operation [66] is used to enhance the blob like regions. To reduce the noise further, the *Closing-by-Reconstruction* [66] is then applied. Since the MCs are elliptical shape objects, a disk-shape structure element is used in both operations. Fig. 7.7(d) shows the homogenous PM (HPM), M_h, after applying the HGMR method. By comparing Fig. 7.7(c) and Fig. 7.7(d), it is clear that the HGMR is able to make the nuclei region more homogenous for the subsequent nuclei segmentation, while at the same time, suppress the noise in the PM.

In order to detect the potential MC, a threshold $T_p = 0.5$ is then applied on the HPM, M_h, such that the pixels in the HPM M_h, whose value is greater than the T_p are regarded as the pixels located in the potential MC regions (we denote these pixels as the potential pixels (PP)). This will result in a binary map, M_b, where the white pixels correspond to the PP and black pixels correspond to other regions. Note that since other cytological components also have similar intensity value as that of the MC regions, the above operations will result in a large number of PP corresponding to the MC. We assume that in the MC regions, all the PP are grouped to form local clusters. Therefore, we calculate the connected components in M_b, and remove the components whose size are smaller than a pre-trained threshold T_r. This threshold is obtained from the training set such that all the true MC are included in the results and fewer false MC regions are included. So far, we get a binary map M_t, where each white component indicates a potential MC regions.

An example is shown in Fig. 7.7(e), where the white components represent the candidate MC regions.

7.2.2.3 Intact MC Candidate Regions Segmentation

Due to the nonuniform absorption of the staining dye, and staining variations, most of the potential MC regions in the M_t are not intact (see Fig. 7.7(e)). A close up example is shown in Fig. 7.8. It is observed that the pre-segmented region is not intact (shown in Fig. 7.8(b)) compared to the ground truth nuclei region shown in Fig. 7.8(c). In literatures, the geometric active contour [**?**], or known as snake, is used to segment the intact region with given initial region contour. In our task, there are a large number of MC candidates. It is computational expensive to evolve the snake on every MC candidate. Therefore, for each potential MC regions, we propose a efficient local threshold method to obtain intact nuclei regions which are required in the next module (i.e., the classification module).

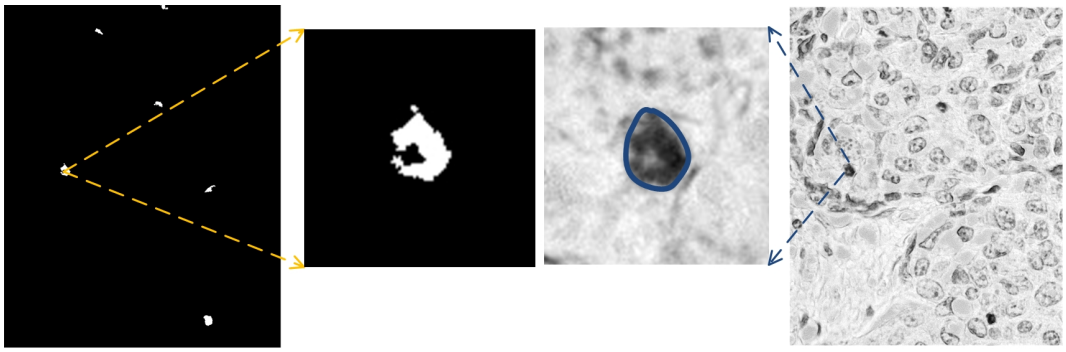

Fig. 7.8. A close up example for the non-intact candidate MC region. (a) binary map M_t which contains several candidate MC regions. (b) zoomed version of an MC region with non-intact region is shown for the illustration. (c) The corresponding image obtained from the DI. The expected intact region is mannually drawn as a thick contour. (d) The DI.

The local threshold method is performed as follows.

1) *Best fitted ellipse calculation*: Denote all the candidate regions in the binary map M_t as $R_{j|j=1...Q}$, where Q is the total number of the candidate regions. An ellipse is fitted based on the boundary points of a candidate region R_j using the direct least square fitting algorithm [55].

2) *Local region determination*: Denote the major axis length of the fitted ellipse as L_j. In order to recover the intact nuclei, a local circular area S_j with an enlarged radii ($2 \times L_j$) is determined.

3) *Local threshold calculation*: Within the local circular area S_j, pixels are retrieved from the DI (calculated from Section 7.2.1). A local threshold (denoted as T_j^{local}) for this local circular area is calculated by using the Otsu's thresholding method [68].

4) *Local area segmentation*: The local threshold T_j^{local} is used to segment its corresponding local area S_j into nuclei and background region. Based on the prior knowledge that the intensity value in the nuclei region is lower than the background, the segmentation is calculated as follows:

$$x = \begin{cases} nuclei, & if\ f(x) \leq T^{local} \\ background, & if\ f(x) > T^{local} \end{cases} \tag{7.13}$$

At the end, the main component in the local circular area is retained whereas other unrelated noisy components are removed by size filtering. The morphological opening operation is then applied to obtain a smooth boundary.

An illustration of the local threshold method is shown in Fig. 7.9. A binary map M_t which contains several candidate MC regions obtained from the last step is shown in Fig. 7.9(a) (the same image shown in Fig. 7.7(e)). An MC region with non-intact region is selected for the illustration, and is shown in Fig. 7.9(b). The centroid of this region and the circular area are shown as the thick point in the middle and the circle in the image, respectively. This local circular area will map to the DI, and a local threshold is calculated for segmentation. Fig.7.9(d) shows the final result for the intact region recovery. It shows that the region is more intact compared to the original region in Fig. 7.9(b). The binary map for all the intact regions is shown in Fig. 7.7(f). The intact regions will help to extract useful features and are required in the following classification module.

Since there exist other cytological components which have similar appearance with the MCs, the candidate regions we obtained so far still contain many false

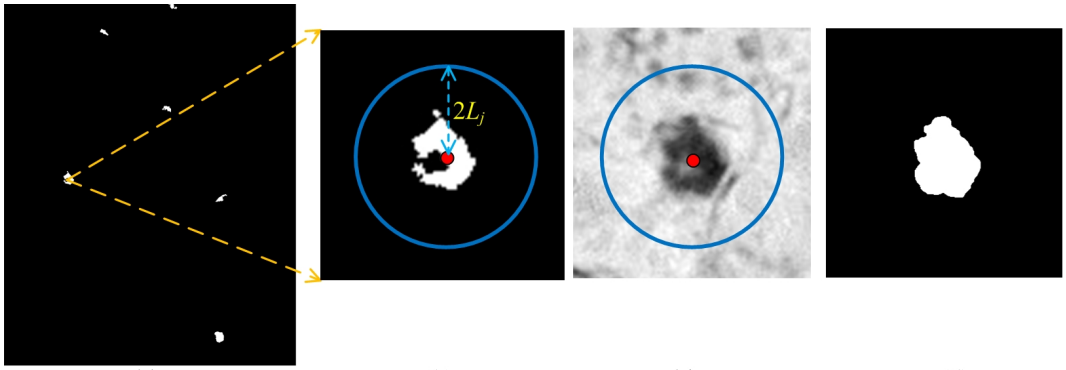

Fig. 7.9. Illustration of the local threshold method. (a) binary map M_t which contains several candidate MC regions. (b) an MC region with non-intact region is selected for the illustration. The centroid of the region is shown as the thick point in the middle. The circular area is shown as the circle in the image. (c) The local circular area will map to the DI, and a local threshold for this local circular area is calculated. (d) The result after the local thresholding within the local circular area.

positives. In the following step, classification is performed to distinguish the MCs and other cytological components.

7.2.3 Classification of MC Candidates

In this module, all the MC candidate regions are classified into MC and other regions using the features extracted from the intact regions.

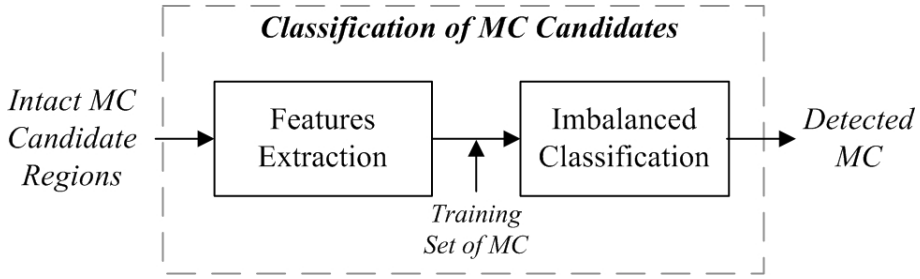

Fig. 7.10. The schematic of the classification module.

7.2.3.1 Features Extraction

In this part, we aim to extract all the features that contribute discrimination information for the final MC detection. These features can be divided into five categories and are summarized in Table 7.2.

We use 12 shape-based features which are shown in the second row of Table 7.2. We also extract the intensity-based and gradient-based features, shown in the third and fourth rows of Table 7.2, respectively. Two commonly used texture-based features, Tamura textures [91] and Haralick-based textures [50], are extracted to measure the textural information on the surface of the regions. Besides these 113 dimensions features extracted from the candidate regions, we also consider the surrounding area of the candidate regions. Thus the same set of features are extracted from the surrounding area of the candidate regions for the next classification module. In total, we have a feature vector $\mathcal{F}$ contains 226 features for each candidate region.

TABLE 7.2
THE SUMMARY OF FEATURES EXTRACTED FROM THE CANDIDATE MC REGIONS AND THE SURROUNDING REGIONS

Feature Type	Feature Name	Dim.
Shape-based [66]	Area, Perimeter, Form Factor, Eccentricity, Solidity, Major/Minor Axis Length, Ratio of Major and Minor Axis Length, Equivalent Diameter, Compactness, Roundness, Extent	12
Intensity-based [66]	Mean, Standard Derivation (SD), Maximum Value, Minimum Value, Entropy	5
Gradient-based [66]	Mean/SD/Entropy of the Gradient Magnitude, Mean Energy of the gradient Magnitude, Ratio of Edge Pixels and Other Pixels in MC	5
Texture-based [50], [91]	3 Tamura Textures: coarseness, contrast, direction, 22 Haralick Textures in 4 directions	91

7.2.3.2 Imbalanced Classification

Due to the high similarity of color and morphological appearances MC and other cytological components, we have obtained a large number of non MC regions versus a small number of MC regions. Note that if we use the traditional classification framework, which pre-assume that the class distribution is roughly even, we will obtain poor performance. Specifically, the trained classifier will have tendency towards the majority class and the accuracy of the minority class will be very low.

Therefore, the classification framework that can deal with the imbalanced class distribution is employed in our work to address the problem.

In the literature, there are four kinds of techniques to address the problem in imbalanced data set classification. The first kind of technique performs the under-sampling in the majority class in order to match the size of the other class [92]. On the other hand, the second kind of technique performs the up-sampling for the minority class to match the size of the other class [93]. The third kind of technique intentionally adjusts the weights for the imbalanced data used in the classification procedure [94]. The fourth kind of technique is based on the multi-experts system (MES) framework where the class decision is generated based on a set of classifiers trained by balanced subsets of training data. Unlike the other three kinds of technique, the MES does not change the samples and class distribution which may remove useful samples or lead to over-fitting. Therefore, it is expected to have better performance than other techniques [95], [96]. In this chapter, we use the MES framework for the MC and non-MC regions classification, which is described below.

Denote the positive training sample set as *P* and negative training sample set as *N*. In this work, the positive samples correspond to the MC regions whereas the negative samples correspond to the non-MC regions. Typically, $N \gg P$, and therefore *P* corresponds to the minority class and *N* corresponds to the majority class. In MES, the majority class set *N* is first decomposed into a few subsets $N_1, \ldots, N_Q$, where the size of each subset is equivalent to that of the minority class sample set. Let the number of subsets be denoted as Q, which is calculated as follows:

$$Q = \lfloor \frac{|N|}{|P|} \rfloor \tag{7.14}$$

where $|\cdot|$ is the cardinity operator to measure the number of elements inside a set. A set of classifiers $\{\mathcal{C}_j\}_{j=1,\ldots,Q}$ are then trained individually using the training set form by $\{N_j \cup P\}_{j=1,\ldots,Q}$. The Support Vector Machine (SVM) [97] with linear kernel is chosen as the base classifier for the classification. For each SVM, i.e., $\mathcal{C}_j$,

we obtained, we will have the seperating plane as follows:

$$(w^j)^T \phi(\mathcal{F}_j) + b^j = 0 \tag{7.15}$$

where w^j and b^j are the coefficients for the current plane $\mathcal{C}_j$ and $\phi(\cdot)$ is the mapping function. For the testing samples, the final label decision will be made based on the all the decisions contributed by the set of classifiers $\{\mathcal{C}_j\}_{j=1,\ldots,Q}$. The major voting rule is used for the final class label decision. Mathematically, the final class label $\mathcal{L}$ is decided by using the equation as follows:

$$\mathcal{L} = \begin{cases} \omega_1, & if \ \sum_{j=1}^{Q} \mathbf{1}\{l_j = \omega_1\} \geq \sum_{j=1}^{Q} \mathbf{1}\{l_j = \omega_2\} \\ \omega_2, & Otherwise \end{cases} \tag{7.16}$$

where l_j is the class label contributed by classifier $\mathcal{C}_j$, and $\mathbf{1}\{\cdot\}$ is the judgment function (if the expression inside the brackets is true then return 1 otherwise 0).

The final classification results will indicate which MC candidates regions are the true MC. The training phase and testing phase for the proposed technique are summarized in Algorithm 1 and Algorithm 2 , respectively. In the training phase, a set of training images $\{I'_j\}_{j=1\ldots S}$ is prepared as the input, where S is the number of spectral images. Also, a set of MC and non-MC regions $\{R_j^{\omega_1}\}_{j=1\ldots Z}$, $\{R_j^{\omega_2}\}_{j=1\ldots Z'}$ are prepared as the training set, where the Z and Z' are the number of regions in the MC and non-MC training set, respectively.

7.3 Performance Evaluation

7.3.1 Image Data

The image data used in this chapter is obtained from publicly available MITOS dataset [81], which includes 35 high resolution multi-spectral images. All images have been manually examined by two experienced pathologists and a total of 224 MCs have been labeled.

The images were acquired using a 10 bands multi-spectral microscope. At each

Algorithm 2 The training phase

Input: Training image set $\{I'_j\}_{j=1...S}$;
MC and non-MC regions training set $\{R_j^{\omega_1}\}_{j=1...Z}$, $\{R_j^{\omega_2}\}_{j=1...Z'}$.

Calculate the optimal coefficient vector $\mathbf{A}^*$ using Eq. 7.8.
Calculate the DI for all training images using Eq. 7.10.
Calculate the PDF $p(f(x)|\omega_1)$, $p(f(x)|\omega_2)$ in DI for $\{R_j^{\omega_1}\}_{j=1...Z}$ and $\{R_j^{\omega_2}\}_{j=1...Z'}$.
Extract the features vectors $\{\mathcal{F}_j^{\omega_1}\}_{j=1...Z}$, $\{\mathcal{F}_j^{\omega_2}\}_{j=1...Z'}$ in DI for $\{R_j^{\omega_1}\}_{j=1...Z}$, $\{R_j^{\omega_2}\}_{j=1...Z'}$.
Train the MES $\{\mathcal{C}_j\}_{j=1...Q}$ with features vector $\{\mathcal{F}_j^{\omega_1}\}_{j=1...Z}$, $\{\mathcal{F}_j^{\omega_2}\}_{j=1...Z'}$.

Output: The optimal coefficient vector $\mathbf{A}^*$;
The PDF $p(f(x)|\omega_1)$, $p(f(x)|\omega_1)$;
The trained SVM classifiers $\{\mathcal{C}_j\}_{j=1...Q}$.

Algorithm 3 The testing phase

Input: A test multi-spectral image **I**.

Calculate the DI using Eq. 7.10 with $\mathbf{A}^*$.
Calculate intact candidate MC regions $\{R'_j\}_{j=1...H}$.
for each candidate MC region R'_j **do**
  Extract the features vector $\mathcal{F}_j$.
  Decide class label $\mathcal{L}$ for R'_j using the trained SVM $\{\mathcal{C}_j\}_{j=1...Q}$.
 if $\mathcal{L}$=ω_1 **then**
  Assign current candidate region R'_j to the MC regions set, i.e., $R'_j \rightarrow \{R_j^{MC}\}_{j=1...H'}$.
 end if
end for

Output: Final detected MC regions set $\{R_j^{MC}\}_{j=1...H'}$.

spectral band, the digitization were performed at 17 different focus planes (each plane being separated from each other with a distance of 500 nm). The spectral bands are spread in the visible spectrum. The 10 spectral bands are described in Table 7.3 [81].

All 35 images in the database were obtained from the breast cancer biopsy slides stained with hematoxylin and eosin (H&E). Each image is captured under a high power fields, size 512×512 μm^2, at 40× magnification. The resolution for the

TABLE 7.3
PROPERTIES OF THE 10 SPECTRAL BANDS.

Band Index	Wavelength (nm)	Main visible color
1	665-710	red
2	410-750	white
3	410-450	dark blue
4	430-490	blue
5	460-510	cyan
6	480-540	green
7	525-575	apple green
8	580-595	yellow
9	590-640	orange
10	625-670	purple red

multi-spectral microscope is 0.185 μm per pixel, which results in a 2767$\times$2767 pixels digital image for each HPF [81].

7.3.2 Segmentation Performance Evaluation

The main objective of the evaluation is to determine if the segmented regions obtained by the proposed technique are consistent with the manually labeled ones. The MC segmentation results are provided with a binary image, where white regions indicate the MC regions. We perform two kinds of evaluations: the MC segmentation evaluation and MC detection evaluation.

In this section, we evaluate MCs segmentation performance. In this evaluation, we randomly selected a set of 50 detected true positive MCs regions. The manually labeled MC regions are treated as the ground truth and will be compared with the automatic segmented regions obtained by the proposed technique.

We define GT as the ground truth MC region, EST as the estimated MC region obtained by the proposed technique. Two area-based evaluation metrics: sensitivity ($\mathcal{A}_{SEN}$), precision ($\mathcal{A}_{PRE}$) are defined as follows:

$$\mathcal{A}_{PRE} = \frac{|GT \bigcap EST|}{|EST|} \times 100\% \tag{7.17}$$

$$\mathcal{A}_{SEN} = \frac{|GT \bigcap EST|}{|GT|} \times 100\% \tag{7.18}$$

where $|\cdot|$ is the cardinality operator. We also use another boundary-based evaluation metric: mean absolute distance (MAD) which is defined as follows:

$$MAD(C^{GT}, C^{EST}) = \frac{1}{M}\sum_{i=1}^{M}[min||C_i^{GT} - C_j^{EST}||] \tag{7.19}$$

where C^{GT} and C^{EST} are the contour/boundary of the ground truth region and estimated region, respectively. C_i^{GT} and C_j^{EST} represent the ith pixel and the jth pixel on the contour of the ground truth region and estimated region, respectively. M is the total number of pixels on the contour of the ground truth region. The MC segmentation performance is shown in Table 7.4. The average value for 150 random selected detected MCs of all the three evaluation metrics are shown in the second row of Table 7.4. Compared to the manually labeled MCs regions, the proposed technique is able to provide accurate segmentation results.

TABLE 7.4
MCs SEGMENTATION PERFORMANCE EVALUATION.

$\mathcal{A}_{SEN}$	$\mathcal{A}_{PRE}$	MAD
89.32%	87.45%	1.74 pixels

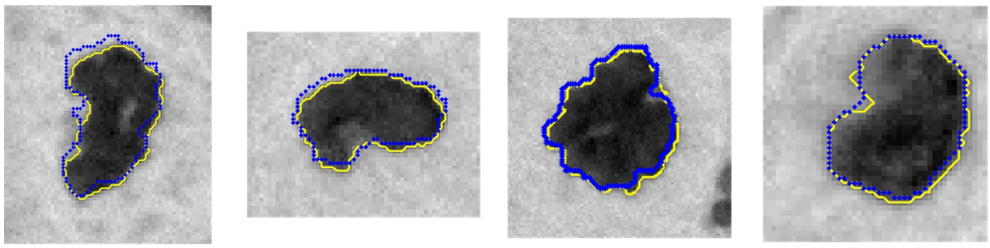

(a) (b) (c) (d)

Fig. 7.11. Examples of the segmented MC regions compared to manually labeled MC regions. The bright contour represent the estimated MC region boundary obtained by the proposed technique whereas the dotted contours are the manually labeled MC regions.

A few examples of the segmented MC regions are shown in Fig. 7.11. In each image, a MC region is presented. The bright contour represent the estimated MC

region boundary obtained by the proposed technique whereas the dotted contours are the manually labeled MC regions. It is observed that the boundary of the segmented MC region obtained by the proposed technique is very close to the manually labeled one.

7.3.3 Detection Performance Evaluation

For evaluating the detection performance, we calculate the centroid of each segmented region obtained by the technique. A segmented MC region is counted as correctly detected if its centroid is localized within a range of 15 pixels of the manually labeled MC centroid location.

We define N_{ML} as the total number of manually labeled MC locations, N_{DO} as the total number of detected MCs, N_{TP} as the number of true-positives, (i.e., correctly detected objects compared to the manually labeled ones), N_{FP} as the number of false-positives. (i.e., falsely detected objects compared to the manual labeled ones).

The performance is evaluated with respect to the precision ($\mathcal{D}_{PRE}$), sensitivity ($\mathcal{D}_{SEN}$), and F-measure ($\mathcal{D}_F$) which are defined as follows:

$$\mathcal{D}_{PRE} = \frac{N_{TP}}{N_{DO}} \times 100\% \tag{7.20}$$

$$\mathcal{D}_{SEN} = \frac{N_{TP}}{N_{ML}} \times 100\% \tag{7.21}$$

$$\mathcal{D}_F = \frac{2 \times (\mathcal{D}_{PRE} \times \mathcal{D}_{SEN})}{(\mathcal{D}_{PRE} + \mathcal{D}_{SEN})} \tag{7.22}$$

We use the 10-fold cross validation [78] for the evaluation. In other words, we first divide the whole dataset into 10 subsets. We then use 9 subsets as the training set and the remaining one subset as the testing set and we obtain the performance. We repeat this procedure for 10 times with different testing set, and use the average performance as the final MC detection results.

The performance of the proposed technique is shown in Table 7.5. The first row shows the detection performance where only the first two module, i.e., module

1 and module 2, are used. The second row shows the performance when a single SVM classifier, instead of the MES, is applied in Module 3. It is observed that the precision rate is increased to 18% with the reduction of the sensitivity rate to 82.5%. The last row shows the performance of the complete proposed technique. By taking into consideration of the distribution of the imbalanced classes, the proposed technique is able to provide a better precision rate at 33.9% with about 82% sensitivity rate, and also achieve the highest F-measure value.

TABLE 7.5
THE PERFORMANCE OF THE PROPOSED TECHNIQUE

Technique	$\mathcal{D}_{PRE}$	$\mathcal{D}_{SEN}$	$\mathcal{D}_{F}$
Module 1 + Module 2	8.8%	90.0%	16.0%
Module 1 + Module 2+ Module 3 (single SVM)	18.3%	82.5%	30.0%
Module 1 + Module 2+ Module 3 (MES)	33.9%	81.5%	47.9%

We also implemented the DMKC technique [30] and compare its performance with the proposed technique. The performance comparison is shown in Table 7.6. The performance of the DMKC technique is shown in the first row. It is observed that the precision rate is very low. In other words, the DMKC technique generated a large number of false positives. As discussed before, the DMKC technique computes the posterior for each pixel by calculating the product of likelihood from all channels in the Bayesian equation. As the intensity values of the MCs are very close to that of the OCCs, when the DMKC computes the posterior, the information unrelated to the MCs are included and lead to lower discriminant. In the proposed technique, we use a different approach (compared to DMKC technique), where the entire multi-spectral images space is first projected into a single discriminant image using the LDA. We then perform local threshold based intact region segmentation. The proposed technique is able to detect more MCs and include smaller proportion of OCCs in the MC candidates set. Overall, the proposed technique is able to provide superior performance compared to the available DMKC technique in the multi-spectral H&E stained histopathological images.

Although the precision is unable to reach a higher value, the proposed technique

TABLE 7.6
THE PERFORMANCE COMPARISON

Technique	$\mathcal{D}_{PRE}$	$\mathcal{D}_{SEN}$	$\mathcal{D}_F$
DMKC	4.5%	90.9%	8.5%
The proposed	33.9%	81.5%	47.9%

can still significantly reduce the workload of the pathologist. Approximately, there is one true positive in three detected objects. Instead of searching the MCs in a very large area, the pathologist can now only focus on the locations of detected objects. Note that the MC is a small object (about 30 μm^2) within a HPF (262,144 μm^2) image, and there are a large number of unrelated cytological components, which might be very similar to that of the MCs, present.

Fig. 7.12 presents three visual examples for the performance comparison. Each column in Fig. 7.12 corresponds to one example. The first row shows the DI for all three examples. The manually labeled (i.e., the ground truth) MCs are indicated by solid arrows in the image. As shown in the first row, there are two, one, and five MCs in the example 1, example 2 and example 3, respectively. The second, third, and fourth rows show the segmentation and detection results obtained by the DMKC technique, the Module 1 and Module 2 of the proposed technique, and the overall proposed technique, respectively. For each image, the result is a binary image, where the white regions represent the detected/ segmented MC regions. A few dotted-line circles are superimposed onto the binary image to highlight the location of the manually label MCs for better comparison. It is observed that in the results obtained by the DMKC technique, except the true positive regions (the white region inside the dotted-line circles), there are a large number of false positive regions. As for the results obtained by the proposed technique, less false positives regions are obtained and all MCs are detected.

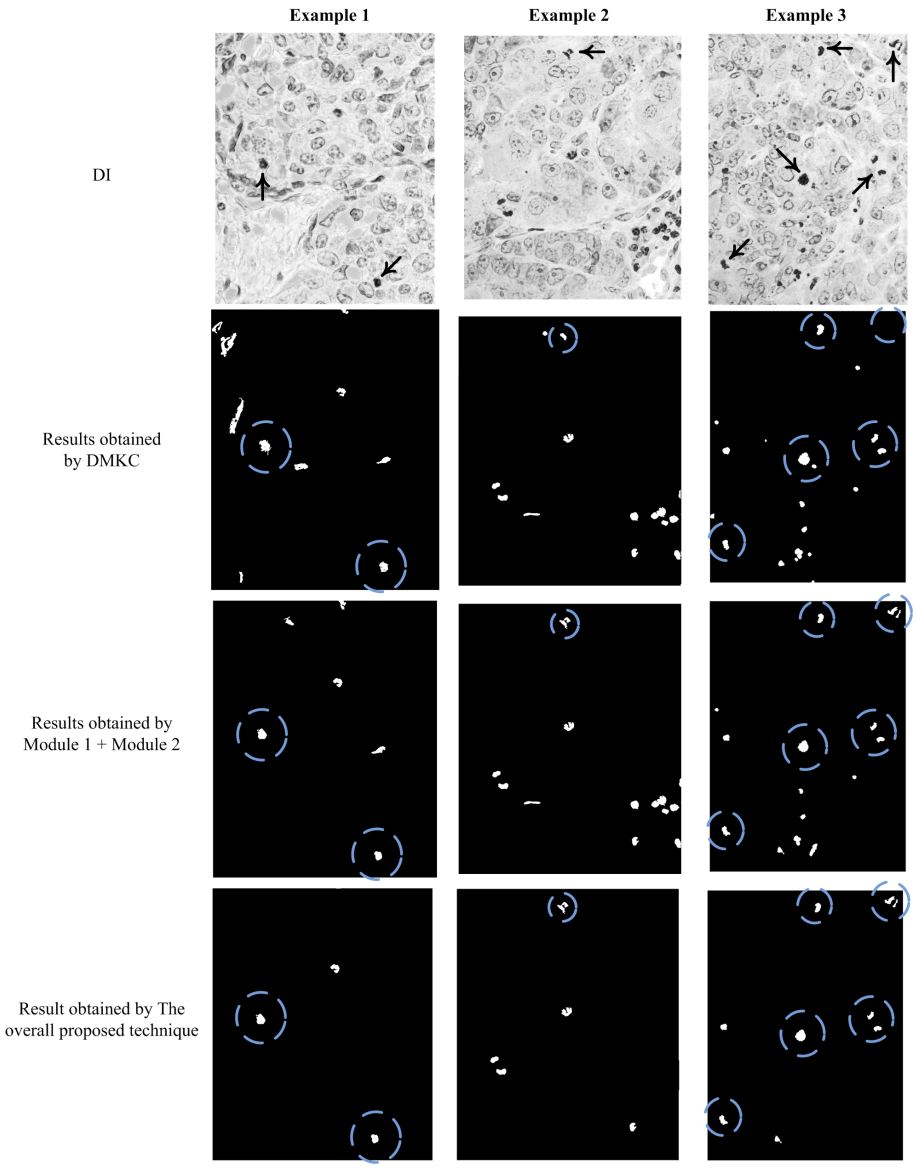

Fig. 7.12. Subjective evaluation of DMKC and the proposed technique.

7.4 Summary

This chapter present an effective computerized technique for mitosis segmentation and detection in histopathological images. The proposed technique first utilizes the multi-spectral images to generate a discriminative image which provides good discrimination between the mitotic cells and other cytological components. The mitotic cell candidates are then identified and segmented by the Bayesian modeling

and local threshold method. Imbalanced classification framework is then applied to perform the classification based on the 226 dimension extracted features from the candidate regions. Evaluation on the public available dataset and comparison with the existing technique show the effectiveness of the proposed technique. The proposed technique is expected to reduce the workload of pathologists when they evaluate the cancer grade of biopsy.

Chapter 8

Classification of the Skin WSI[1]

8.1 Introduction

In this chapter, I present an automatic analysis and diagnosis system for the whole slide skin pathological image. This system is mainly based on the fundamental techniques presented in Chapter 4 (segmentation and analysis the epidermis), Chapter 5 (nuclei segmentation in epidermis), and Chapter 6 (melanocytes detection in epidermis). By combining these techniques, and constructed the features for classification, the goal of the system is to provide quantitative measures which will help the pathologist for their diagnosis and classify the melanoma (mainly contain superficial spreading melanoma), melanotic nevus and normal skin biopsy automatically.

8.2 The Proposed Technique

8.2.1 The Overview of the Proposed Technique

The schematic of the proposed technique is shown in Fig. 8.1. The proposed technique consists of five modules. Given a WSI, the first three cascade modules are used for the segmentation and detection of ROIs. The *epidermis area segmentation*

[1] A version of this chapter has been submitted for publication. Cheng Lu, Mrinal Mandal, "Automated Analysis and Diagnosis of Skin Melanoma on Whole Slide Histopathological Images", *Pattern Recognition*.

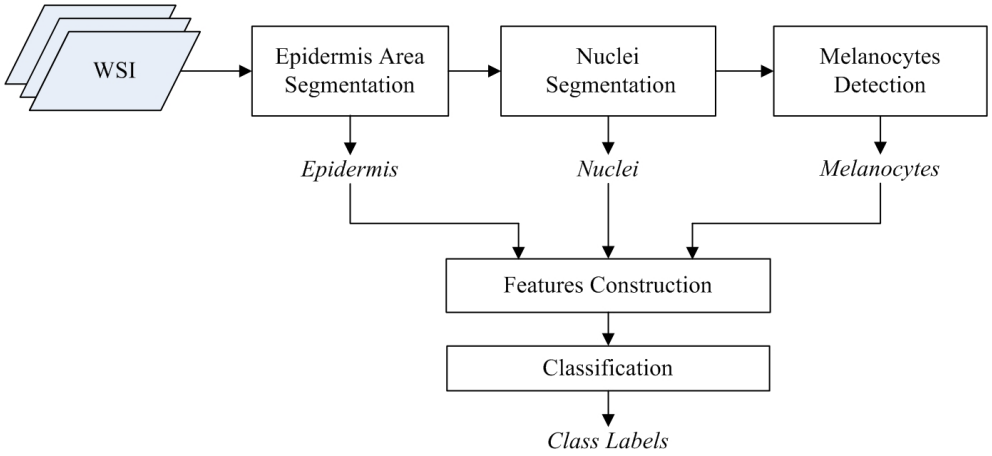

Fig. 8.1. The overall schematic of the proposed technique.

module aims to segment the skin epidermis in the WSI. The *nuclei segmentation* module is applied to segment the nuclei in epidermis. The *melanocytes detection* module is used to detect the melanocytes from the pre-segmented nuclei. Based on the pre-segmented epidermis area, nuclei, and melanocytes, the *features construction* module will consider the spatial arrangement and morphological characteristics of the pre-segmented ROIs and construct the features according to the diagnostic factors used by pathologists. The last module, i.e., the *classification* module, utilizes the features to classify the tissues into three categories: melanoma, nevus, or normal skin.

8.2.2 Epidermis Area Segmentation

Unlike other types of tissue specimen, a typical skin tissue slide consists of three main parts: epidermis, dermis and subcutaneous tissues. The anatomy of a typical skin tissue is shown in Fig. 8.2, where the lower image shows the manually labeled contour of the epidermis. The epidermis area is the most important observation area for the diagnosis of a skin tissue. In most cases of melanoma, the grading of the cancer can be made by analyzing the architectural and morphological features of atypical cells in the epidermis or epidermis-dermis junctional area. Therefore, segmentation of the epidermis area is an important step before further analysis is

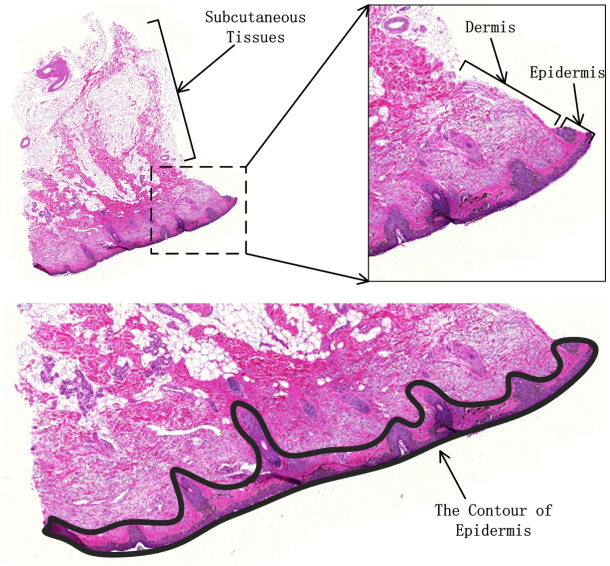

Fig. 8.2. The anatomy of a skin tissue.

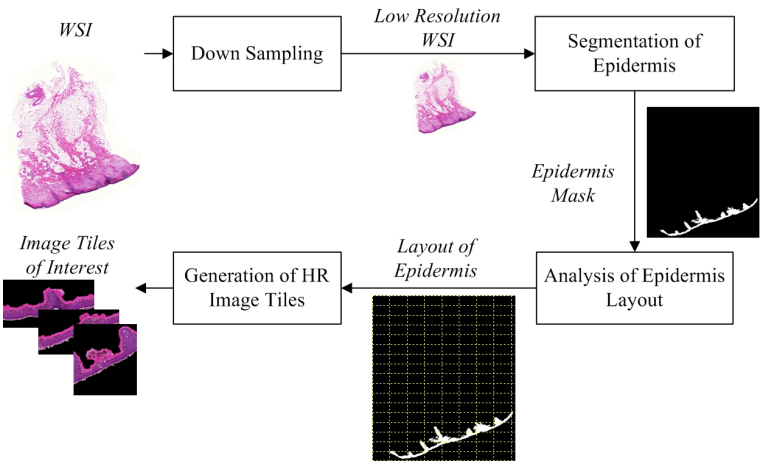

Fig. 8.3. The schematic for epidermis area segmentation module.

performed.

In our previous work [20], an efficient technique for automatic epidermis area segmentation and analysis has been proposed. This technique is adopted here for the epidermis segmentation and high resolution (HR) image tile generation. The schematic of the epidermis area segmentation technique is shown in Fig. 8.3 and explained as follows [20].

- **Down sampling:** In order to reduce the processing time, the high resolu-

tion (HR) WSI is first down sampled into a low resolution (LR) WSI.

- **Segmentation of epidermis:** In this step, the red channel of the WSI is selected for the segmentation since it provides the most discrimination between the epidermis and other regions ([20]). The Otsu's threshold method [68] is then applied for the initial segmentation. In order to eliminate the false positive regions after the thresholding, two critera based on the area size and shape are used to determine the real epidermis area. Finally, morphological operation (e.g., opening and closing) are applied to fill in the holes and smooth the boundary. An epidermis mask is thus obtained.

- **Analysis of epidermis layout:** Based on the epidermis mask, the epidermis layout is determined. The layout of epidermis is defined as horizontal or vertical. The entire epidermis mask is first divided into small grids. Within each grid, the percentage of bright pixels is counted. If the percentage of the bright pixels is greater than a threshold, this grid is assigned a value 1, otherwise 0. A straight line is then fitted through the grids with value 1 to determine the acute angle between the epidermis and the horizontal line. If the angle is greater and equal to 45°, the epidermis layout is vertical, otherwise horizontal.

- **Generation of HR image tiles:** The segmented epidermis in LR is first mapped to HR. The whole segmented epidermis area is then divided into several image tiles for further analysis. Based on the layout of the epidermis, the HR image tiles are generated across the epidermis area so that at each image tile all sub-layers of the epidermis can be observed. If the layout is vertical (horizontal), we generate the image tiles by stitching the image blocks with segmented epidermis mask horizontally (vertically). An example is illustrated in Fig. 8.4.

In Fig. 8.4, the binary mask represents the segmented epidermis area, where the white region indicates the epidermis area and the black region indicates the background and other regions. The layout of the epidermis is horizontal, and therefore

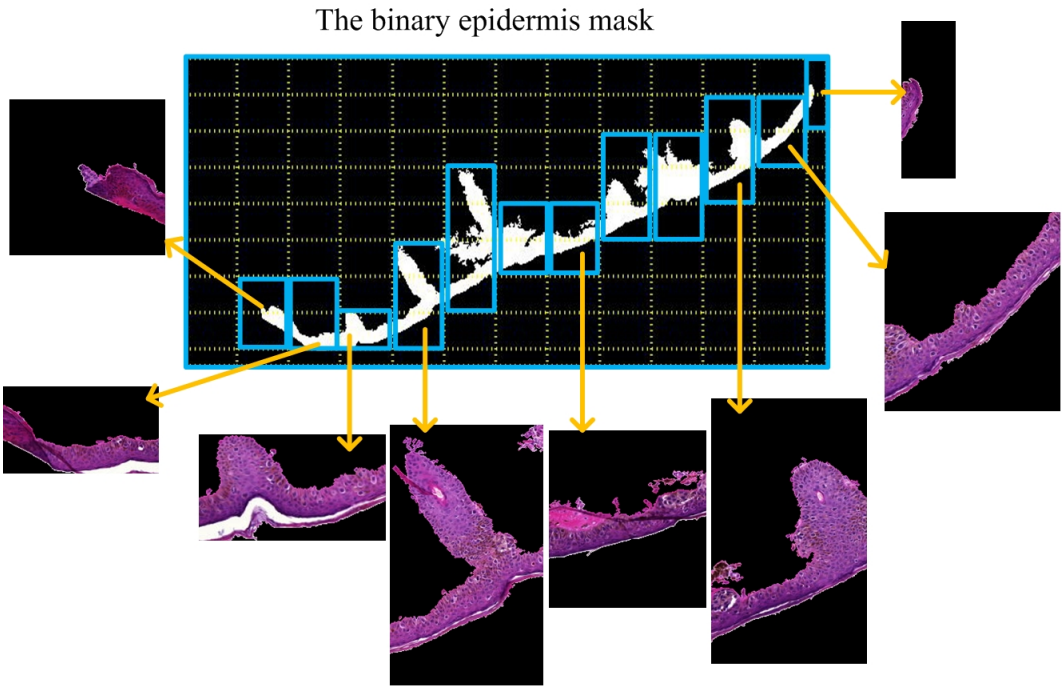

Fig. 8.4. An example of generating the image tiles from the binary epidermis mask (shown in the center). Note that the layout of the epidermis is horizontal in this example, and hence the image tiles are generated vertically. The rectangles indicate the generated image tiles for further processing. Some of the snapshot of the image tiles are present.

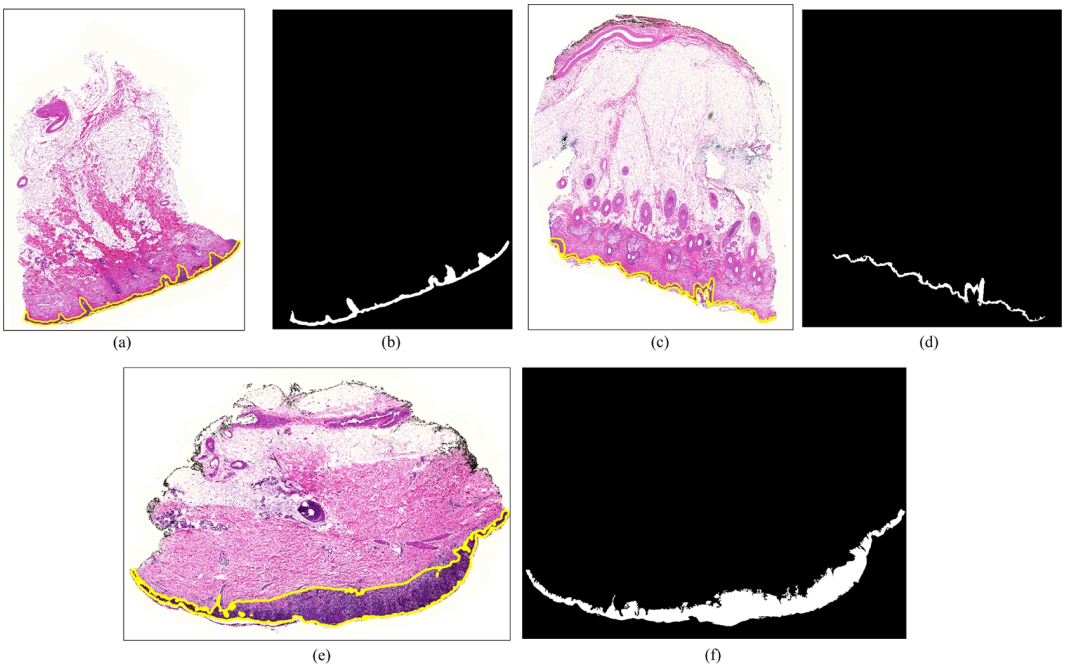

Fig. 8.5. Three examples of the epidermis segmentation results. (a), (c), and (e) show original images with manually labeled epidermis area (shown as bright contour). (b), (d), and (f) show the binary images that represent the segmentation result where the white region indicates the epidermis area, and the black region indicates the background and other regions.

the images tiles are generated vertically. The thick rectangles indicate the generated image tiles for further processing. Some of the snapshot of the HR image tiles are shown in Fig. 8.4.

Three epidermis area segmentation results are shown in Fig. 8.5. In Figs. 8.5(a), (c), and (e), the original images with manually labeled epidermis area (shown as bright contour) are shown. Figs. 8.5(b), (d), and (f) show the binary mask that represent the segmentation result.

8.2.3 Nuclei segmentation

Based on the HR image tiles obtained from Section 8.2.2, it is now possible to segment the nuclei in the epidermis area. Considering the intensity variations, an adaptive threshold technique is applied to segment the nuclei regions [21]. This technique has two main steps which are described as follows.

8.2.3.1 Hybrid gray-scale morphological reconstruction (HGMR).

In order to reduce the influence from undesirable variations in the image and to make the nuclei region homogenous, a hybrid gray-scale morphological reconstruction method is applied. The steps of HGMR are described below.

(a) Complement of the Image: Assuming an 8-bit image R, the complement image $\bar{R}$ is calculated as follows:

$$\bar{R}(x, y) = 255 - R(x, y) \tag{8.1}$$

where (x, y) is the coordinate.

(b) Opening-by-Reconstruction: In order to enhance the nuclei regions, the *opening-by-reconstruction* operation [66] is performed on the image $\bar{R}$ as follows:

$$\bar{R}_{obr} = \mathfrak{R}(\bar{R}_e, \bar{R}) \tag{8.2}$$

where $\mathfrak{R}$ is the morphological reconstruction operator [66], $\bar{R}_e = \bar{R} \ominus S$ (where $\ominus$ is the erosion operator), and S is the structuring element. The eroded image obtained by applying erosion on Fig. 8.6(b) is shown in Fig. 8.6(c). The result of the *opening-by-reconstruction* is shown in Fig. 8.6(d). Comparing Fig. 8.6(d) and Fig. 8.6(b), it is observed that the nuclei regions have been enhanced.

(c) Closing-by-Reconstruction: In order to reduce the noise further, the closing-by-reconstruction is performed on $\bar{R}_{rbo}$ as follows:

$$\bar{R}_{obrcbr} = 255 - \mathfrak{R}((255 - \bar{R}_{obr}) \ominus S, 255 - \bar{R}_{obr}) \tag{8.3}$$

The result of the *closing-by-reconstruction* is shown in Fig. 8.6(g). Note that the intensity within the nuclei regions is more homogenous compared to that in Fig. 8.6(d).

(d) Complement of the Image: This step calculates the complement of $\bar{R}_{obrcbr}$ in order to map the image into the original intensity space, i.e., $R'(x, y) = 255 -$

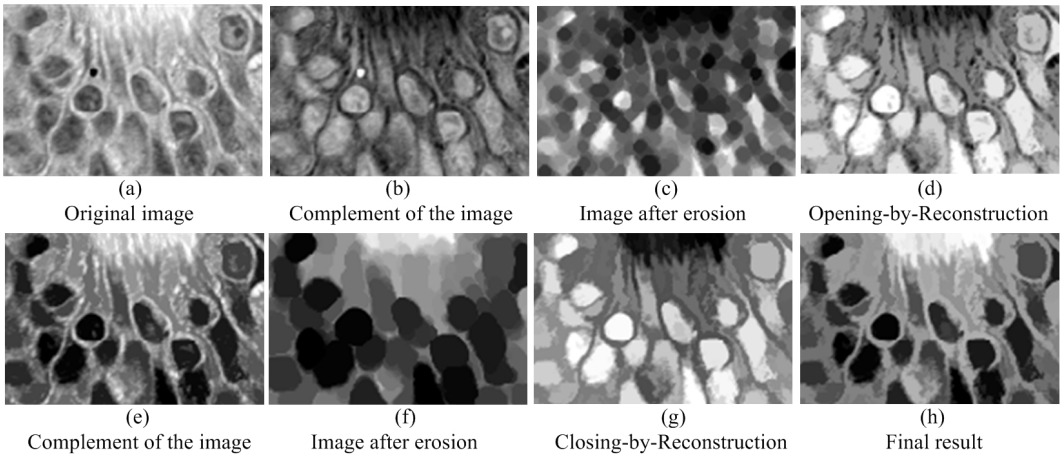

Fig. 8.6. Example of hybrid gray-scale morphological reconstruction. nuclei segmentation result in epidermis area.

$\bar{R}_{obrcbr}(x, y)$. The final image is shown in Fig. 8.6(h).

8.2.3.2 Local region adaptive threshold selection

For initial segmentation, a global threshold (Otsu's threshold method [68]) is first applied on the image. We have found that the touching of multiple nuclei often results in an abnormally large region (ALR), and degrades the segmentation performance. To address this, a local region adaptive threshold selection (LRATS) method has been proposed to achieve finer segmentation [21]. In LRATS, a local threshold is determined by minimizing a pre-defined cost function. Denote an ALR as L and the kth fragment obtained by a threshold t within an ALR as $L_k(t)$, the cost $C(t)$ is calculated for the current threshold t as follows:

$$C(t) = \frac{1}{K}\sum_{k=1}^{K}[\Phi_E(L_k(t)) + \Phi_A(L_k(t))] \tag{8.4}$$

where K is the total number of segmented fragments obtained by the current threshold t, and $\Phi_E(L_k(t))$ and $\Phi_A(L_k(t))$ are two penalty functions that correspond to the ellipticity and area of the regions, respectively. Intuitively, if the segmented fragments are close to elliptical shape and the segmented areas are within the pre-defined area range [A_{min}, A_{max}], the cost function $C(t)$ will have a small value.

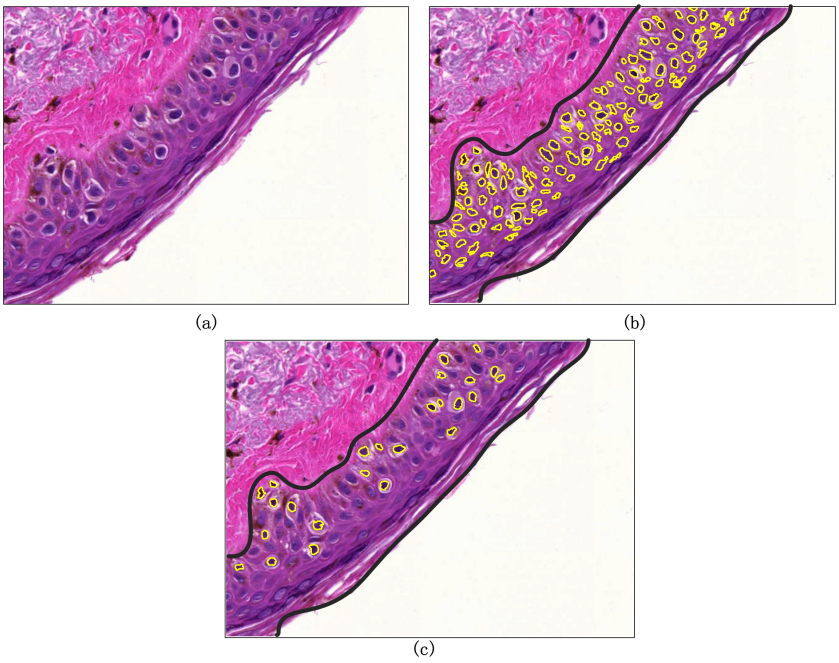

Fig. 8.7. An example of nuclei segmentation result in epidermis area. (a) shows a small portion of the epidermis in WSI. (b) shows the automatic segmented nuclei (indicated by the thick bright contours) within the epidermis area (indicated by the thick black line). (c) shows the automatic segmented melanocytes (indicated by the thick bright contours).

An epidermis area is shown in Fig. 8.7(a), and the nuclei segmentation result is shown in Fig. 8.7(b).

8.2.4 Melanocytes Detection

In the skin melanoma diagnosis, the architectural and cellular features (e.g., size, distribution, location) of the melanocytes in the epidermis area are important factors. In this module, the melanocytes are detected from the pre-segmented nuclei in the epidermis.

In the epidermis area of skin, a normal melanocyte is typically a cell with a dark nuclei, lying singly in the basal layer of epidermis. However, in the melanoma or nevus, the melanocytes grow abnormally, and can be found in the middle layer of epidermis. The digitized histopathological images we used in this work are stained with haematoxylin and eosin (H&E). Three examples of skin epidermis images are shown in Figs. 8.8(a), (b), and (c). The cell nuclei are observed as dark blue whereas

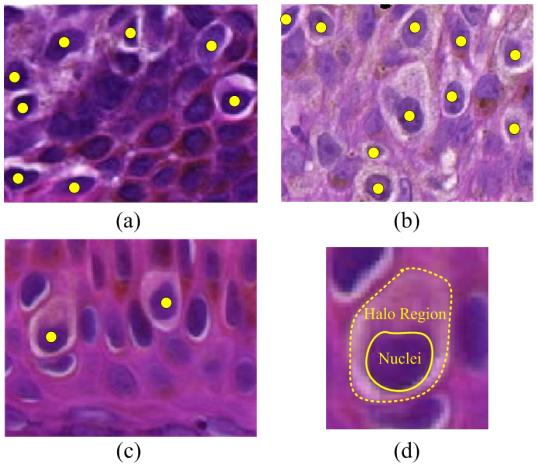

Fig. 8.8. Melanocytes in epidermis area from different skin samples. Inter- and intra-image variations are observed in terms of the color. These images are sampled from the skin WSI. In (a), (b), and (c), the bright seed points indicate the location of melanocytes whereas other nuclei are keratinocytes. (d) is a close up image of a melanocyte.

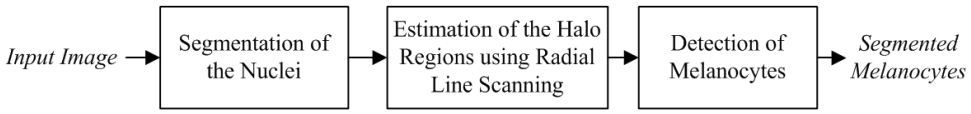

Fig. 8.9. The schematic of the melanocyte detection technique.

the intra-cellular material and cytoplasm are observed as bright pink. Note that the bright seed points indicate the location of melanocytes whereas other nuclei are the keratinocytes.

It is observed that the differences between melanocytes and other nuclei are the surrounding region. The melanocytes generally have brighter halo-like surrounding regions and are retracted from other cells, due to the shrinkage of cytoplasm [74]. One close up example of a melanocyte is shown in Fig. 8.8(d), where the outer dotted contour represents the halo region and the inner solid contour represents the nuclei. In contrast, the other nuclei are in close contact with the cytoplasm and have no or little brighter area. The brighter halo-like region of the melanocyte is an important pattern for differentiation of the melanocytes and other nuclei.

In this module, we adopted one of our previous works for the melanocytes detection [23]. The schematic of the melanocyte detection technique is shown in Fig. 8.9.

Based on the pre-segmented keratinocytes, the melanocyte detection technique first estimated the outer boundary of halo region using the radial line scanning (RLS) method. At first, the RLS method initializes the radial center and radial lines for each pre-segmented keratinocytes (see Fig. 8.10(c)). On each radial line, the gradient information is calculated and the outer boundary points of the halo region is estimated (the inner boundary is already obtained by the *nuclei segmentation* module). Intuitively, the point on a radial line whose gradient direction is going inwards is determined as the outer boundary point of the halo. Examples of the estimated halo regions are shown in Fig. 8.10(e). Once the halo region is estimated, the melanocytes are then determined based on the ratio of the estimated halo region and the original nuclei region. The ratio, R_{HN}, is calculated as follows:

$$R_{HN} = \frac{A_{HR}}{A_{NR}} \tag{8.5}$$

where A_{HR} and A_{NR} are the areas of the halo and nuclei regions, respectively. For the melanocyte detection, we select the nuclei regions as the melanocytes if its R_{HN} value is greater than a predefined threshold $T_{R_{HN}}$. Examples of the value R_{HN} are shown in Fig. 8.10(e). A melanocytes detection result is shown in Fig. 8.7(c).

8.2.5 Features Construction: Spatial Distribution Features

In the previous modules, the epidermis area, the keratinocytes and the melanocytes in the epidermis area are segmented and detected by the automated techniques. These ROIs are now ready to be further analyzed by computer-aided techniques based on the pathologist's evaluation procedure. In the manual evaluation, several important factors are considered by a pathologist. In the proposed technique, these important factors are considered for the classification.

The spatial distribution of the melanocytes in epidermis area is an important diagnostic factor. In normal skin epidermis, the melanocytes are evenly distributed along the basal layer of the epidermis. The ratio between the melanocytes and other keratinocytes in skin tissues is between 1:10 and 1:20. In the case of melanotic

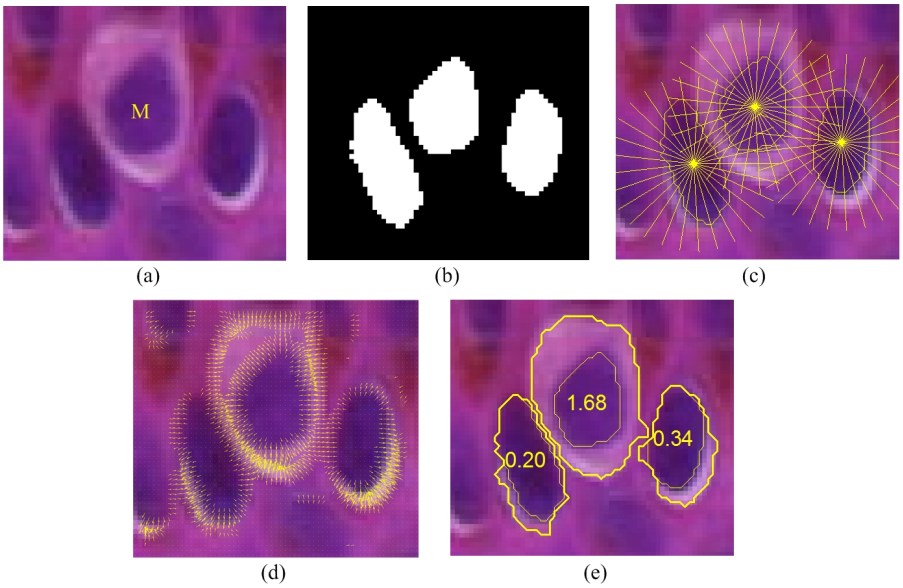

Fig. 8.10. Illustration of the RLS method. (a) is the original image with three nuclei regions where the melanocyte is indicates with letter 'M'. (b) shows the segmented nuclei regions. (c) shows the radial lines for each nuclei region (nuclei regions are shown with thick contours). (d) shows the suppressed smoothed gradient map. (e) shows the halo region estimation result. The value of the parameter R_{HN} is shown inside the nuclei region.

nevus, there is a large number of melanocytes and these melanocytes may form several nests in the junction of epidermis and dermis area or penetrate into the dermis area. In the case of melanoma, the number of the melanocytes is large as well, but not as large as that in the case of nevus. However, the melanocytes may invade into the upper layers of the epidermis or invade deep into the dermis area. Based on the characteristics mentioned above, we utilize the number and location of the pre-segmented ROIs, i.e., keratinocytes, melanocytes to construct the spatial distribution features for further analysis.

In order to calculate the spatial distribution, we first determine the thickness of the epidermis. The spatial distribution features are then generated.

8.2.5.1 Local thickness measurement

The thickness of epidermis in skin varies significantly, and therefore the thickness of epidermis needs to be measured locally. The measurement method is described below.

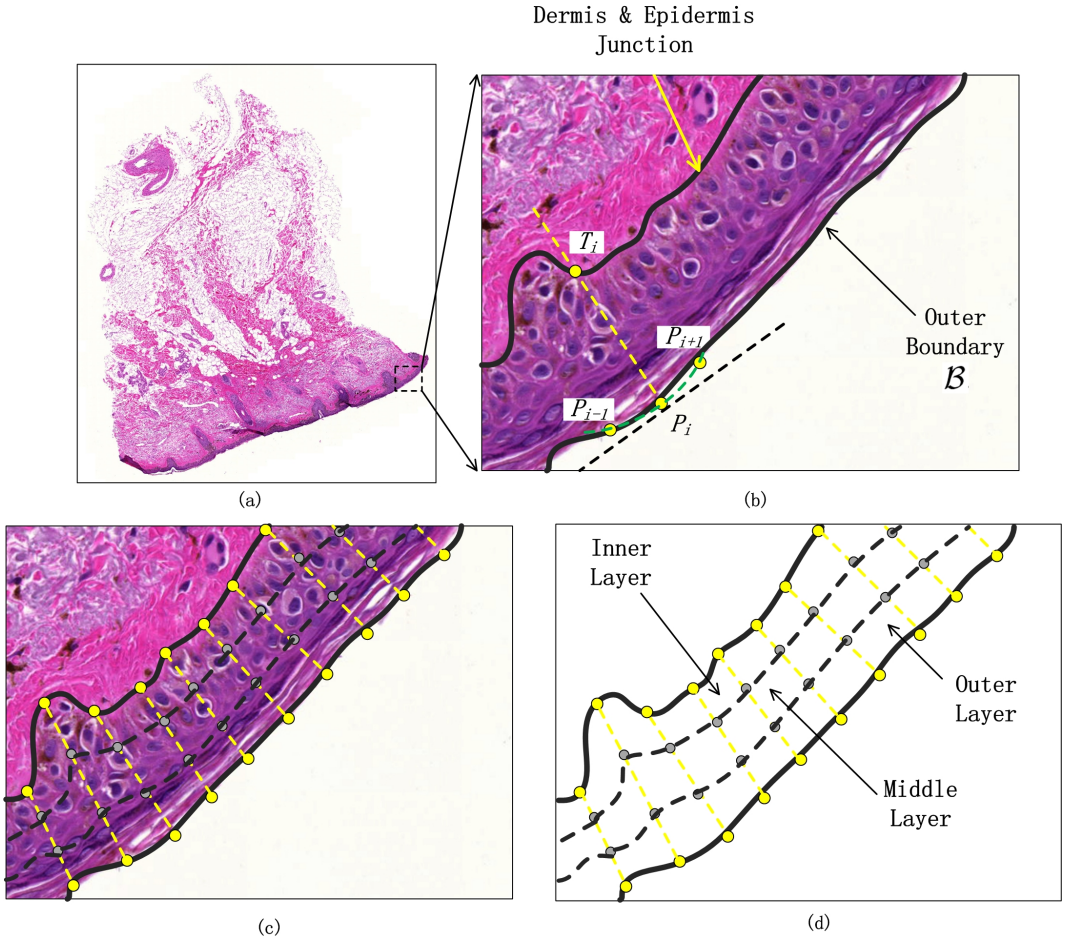

Fig. 8.11. Epidermis depth measurement, and construction of sub-layers for the epidermis.

- **Determine the boundary of epidermis base**: At first, based on the layout of the epidermis area, horizontal or vertical, the outer boundary of epidermis is determined. Fig. 8.11(a) shows a horizontal layout skin tissue and Fig. 8.11(b) shows a zoomed version of local epidermis area. The boundary of epidermis base is highlighted in Fig. 8.11(b).

- **Assign sampling points**: On the pre-determined base boundary, we select a few points by fixed-interval sampling. Assuming that there are K points on the outer boundary $\mathcal{B}$, and setting the interval to $\varepsilon = 5$, we obtain a set of boundary points as follows:

$$\Lambda = \{p_i \in \mathcal{B} | i = \varepsilon \times j, j = 1, \ldots, \lfloor K/\varepsilon \rfloor\}. \tag{8.6}$$

  Fig. 8.11(c) illustrate the sampling points (shown as bright dots) on the epidermis base boundary.

- **Measure local thickness**: Based on the sampling points on the base boundary, the thickness of the epidermis is measured. Given a sampling point $p_i \in \mathcal{B}$, we obtain its neighboring sampling points p_{i-1} and p_{i+1}. A curve $\mathfrak{C}$ is estimated based on the three points p_i, p_{i-1} and p_{i+1} using a polynomial curve fitting method. A line $\mathfrak{T}_i$, which is tangent to the fitted curve at point p_i, is then calculated. The line $\mathfrak{N}_i$ normal to the tangent line $\mathfrak{T}_i$ will reflect the orientation of local epidermis area. The local depth measure $\mathfrak{D}_i$ is calculated as the distance from the current sampling point $p_i \in \mathcal{B}$ along the estimated normal line $\mathfrak{N}_i$ until it reaches the inner boundary of the epidermis (i.e., the dermis and epidermis junction). This is illustrated in Fig. 8.11(b). For each sampling point, the local thickness is measured.

8.2.5.2 Spatial Distribution Features

Based on the thickness measured in the last section, we divide the epidermis into three sub-layers evenly. These three sub-layers are denoted as $\mathbb{L}_{inner}$, $\mathbb{L}_{middle}$, and

$\mathbb{L}_{outer}$, respectively. This is illustrated in Fig. 8.11(c) and (d), where the boundary of the three layers are highlighted. The number of pre-segmented nuclei and melanocytes which are located within these three sub-layers are then calculated. The ratio of the melanocytes and nuclei within these sub-layers are calculated as a set of features for the classification. Denote $\mathcal{N}_{Nu}$, and $\mathcal{N}_{Me}$ as the number of nuclei and melanocytes in epidermis area, respectively. The ratio of the number of the keratinocytes and melanocytes in inner, middle, outer layers are calculated as follows:

$$R_{MN}^{\mathbb{L}_{inner}} = \mathcal{N}_{Me}^{\mathbb{L}_{inner}} / \mathcal{N}_{Nu}^{\mathbb{L}_{inner}}, \tag{8.7}$$

$$R_{MN}^{\mathbb{L}_{middle}} = \mathcal{N}_{Me}^{\mathbb{L}_{middle}} / \mathcal{N}_{Nu}^{\mathbb{L}_{middle}}, \tag{8.8}$$

$$R_{MN}^{\mathbb{L}_{outer}} = \mathcal{N}_{Me}^{\mathbb{L}_{outer}} / \mathcal{N}_{Nu}^{\mathbb{L}_{outer}}. \tag{8.9}$$

8.2.6 Features Construction: Morphological Features

Besides the spatial distribution of the pre-segmented melanocytes, the morphological features are also important features for the classification. The morphological features will reflect the grading of the skin tissue under examination.

The five morphological features used in this chapter are presented below:

- Area: The area of the detected nuclei.
- Perimeter: The perimeter of the detected nuclei.
- Eccentricity: The eccentricity is the ratio of the distance between the foci of the best fit ellipse and the major axis length.
- Equivalent Diameter: Measure the diameter of a circle that has the same area of current measured region, i.e., $\sqrt{4 \times Area/\pi}$.
- Ellipticity: The ratio of the major axis and minor axis of the best fit ellipse.

For each feature, we calculate the mean value and the SD value for the pre-segmented melanocytes in the epidermis area. This results in 10 morphological features.

In total, a 13 dimensional feature vector $\mathcal{F}$ (three spatial distribution features and ten morphological features) is constructed for each skin WSI.

8.2.7 Classification

After the feature construction, a classification technique is applied to classify the WSI into three classes. In this work, support vector machine (SVM) is used for the classification. While the SVM is originally proposed for two-class classification, it has been extended for the multi-class classification [98]–[100]. The "one-against-one" multi-class SVM method has been shown to provide better performance than other multi-class SVM methods [100]. In "one-against-one" multi-class SVM method, the multi-class classification problem is decomposed into $n(n-1)/2$ two-class classification problems, where n is the number of classes. These $n(n-1)/2$ two-class SVMs are trained using the samples from the corresponding paired classes.

The hyperplane to separate the ith class and the jth class can be expressed as:

$$(w^{ij})^T \phi(\mathcal{F}) + b^{ij} = 0 \tag{8.10}$$

where w^{ij} and b^{ij} are the coefficients for the hyperplane, and $\phi(\cdot)$ is the mapping function.

In the testing phase, the testing sample will be labeled by all the $n(n-1)/2$ two-class SVMs. If the current SVM labels the sample as the ith class, then the votes of the ith class is increased by 1. After the testing sample is labeled by all $n(n-1)/2$ two-class SVMs, the accumulated votes is calculated. The class label that has the maximum votes will be assigned to the testing sample.

8.3 Performance Evaluation

8.3.1 Image Dataset

In this study, we have evaluated the proposed technique on 66 different whole slide cutaneous histopathological images. The histological sections used for image acquisition are prepared from formalin-fixed paraffin-embedded tissue blocks of skin biopsies. The sections prepared are about 4μm thick and are stained with H&E using automated stainer. The skin samples used includes melanoma (most of them are superficial spreading melanoma, and these type of melanoma are the most frequently melanoma), melanocytic nevus, and normal skin. Table 8.1 shows the distribution of these three classes. The digital images were captured under 40X objective magnification on Carl Zeiss MIRAX MIDI Scanning technique (Carl Zeiss Inc., Germany).

TABLE 8.1
DESCRIPTION OF THE IMAGE DATASET.

Class	No.	Percentage
melanoma	32	48.48%
nevus	17	25.76%
normal	17	25.76%
Total	66	100%

8.3.2 Performance Comparison

We use the 10-fold cross validation [78] for the evaluation. In other words, we first divide the whole dataset into 10 subsets. We then use 9 subsets as the training set and the remaining one subset as the testing set, and we obtain the performance. We repeat this procedure for 10 times with different testing set. We also repeat the 10-fold cross validation for 100 times, the average performance is used as the final performance for the classification.

It is observed that the proposed technique is able to classify most of the skin

TABLE 8.2
PERFORMANCE EVALUATIONS.

Techniques	Classification Accuracy (%)
The proposed technique with all (13) features	89.07 ± 2.72
The proposed technique with only distribution-based (3) features	77.41 ± 1.19
The proposed technique with only morphological (10) features	83.21 ± 2.29
The TCA technique	70

tissues correctly by using all features. If only the distribution-based features are used, the classification accuracy goes down to about 78%. It is noted that if only the morphological features are used, about 84% accuracy is achieved.

We also implement the TCA technique for comparison, the classification accuracy is shown in the last row of Table 8.2. In the implementation of the TCA technique, we randomly select 12 WSIs for the training phase and select the remaining WSIs for the testing phase. In the testing phase, the WSI is first divided into small image blocks. In each WSI, the background blocks and the tissue blocks are manually labeled. Within the tissue blocks, the blocks containing cells (denoted as cell block) and the blocks containing other cytological components are manually labeled. Within the cell blocks, the blocks containing malignant cells and the blocks containing benign cells are manually labeled. The features extracted from these three paired of blocks (i.e., background and tissue blocks, cell blocks and other cytological components blocks, malignant cells and benign cells blocks) are then used to train three classifiers. In the testing phase, the WSI is divided into small image blocks. Each block is then be classify by the pre-trained classifiers. The percentage of the malignant cells and benign cells blocks with respect to the total number of blocks are then calculated. If the percentage of the malignant cells blocks is dominant (with a threshold set at 50%), a WSI is determined as a melanoma, otherwise normal or nevus tissue. Note that in the implementation of the TCA technique, we consider a two classes classification problem, i.e., the malignant tissue (melanoma) versus benign tissue (naevus and normal skin). The classification performance of

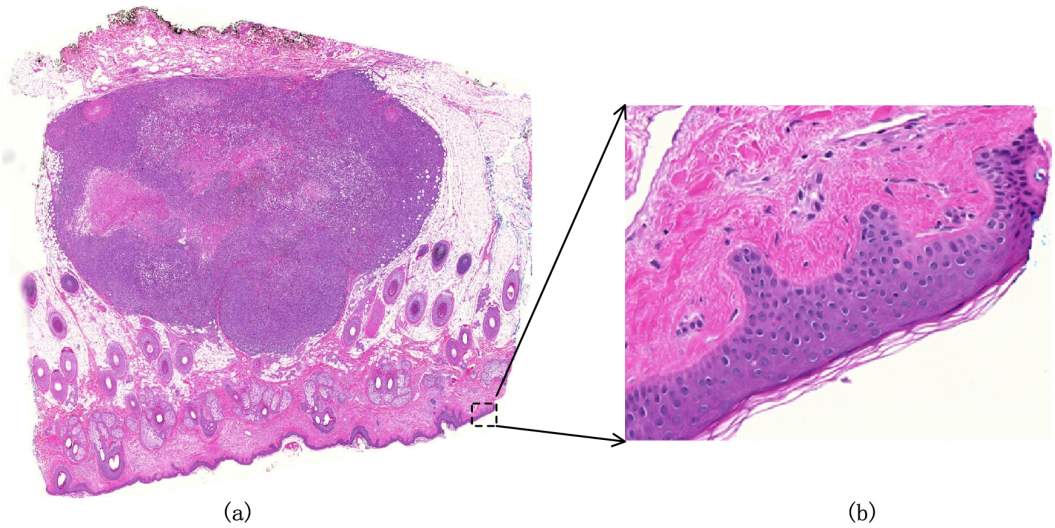

Fig. 8.12. An example of misclassified skin tissue. (a) An snapshot of a skin WSI. (b) a zoom in image of the rectangle area in (a).

the TCA technique is 70%, which is lower than the proposed technique. One reason behind this performance is that the TCA technique only consider the pixel-level features, the staining variation will degrade the classification performance. However, the proposed technique considers the object-level features which are less affected by the staining variations. Another draw back is that the TCA technique requires user interactions for the training blocks selection whereas the proposed technique requires less user interactions.

An example of the misclassification by the proposed technique is shown in Fig. 8.12. This skin tissue belongs to the melanoma class (in-transit metastasis type). The proposed technique misclassified this skin tissue as the normal class. This is because this melanoma skin tissue is in-transit metastasis, and hence the spatial distribution and the morphological features in the WSI (in the epidermis) look very similar to that of the normal skin. Therefore, the proposed technique misclassifies this melanoma tissue as a normal class. Incorporating additional features from dermis area is required to classify it as melanoma.

8.3.3 Computational Complexity Evaluation

All experiments were carried out on a 2.4-GHz Intel Core II 597 Duo CPU with 3-GB RAM using MATLAB 7.04. On average, the proposed technique takes about 36 minutes to finish the analysis on a 12,000 $\times$ 10,000 color WSI, which contains about 2300 nuclei and 350 melanocytes in the epidermis area. The *epidermis segmentation* module takes 0.5% of the whole processing time. The *nuclei segmentation* module takes 2.6% of the whole processing time. The *melanocytes detection* module takes 94.4% of the whole processing time. The *feature construction* module and the *classification* module take 2.5% of the whole processing time.

8.4 Conclusion

In this chapter, we present an automatic analysis and classification technique for the melanotic skin WSI. The epidermis area, nuclei, and melanocytes are first segmented by automatic techniques. The spatial distribution and morphological features based on the pre-segmented ROIs are then extracted, and classified. The proposed technique provides about 90% accuracy on the classification of melanotic nevus, melanoma, and normal skin.

Chapter 9

Conclusions and Future Research Direction

9.1 Conclusions

This thesis has developed several new techniques for quantitative analysis of the whole slide skin specimen. The main contributions have been presented in Chapters 4 to 8.

Chapter 4 developed a framework for segmentation and analysis of the whole slide image which is an important step before further analysis is performed. In order to perform an effective segmentation, a monochromatic color channel is first determined. By using the pre-determined monochromatic channel, a hybrid technique based on global threshold and shape analysis is employed to segment the epidermis from the WSI. This chapter also discussed generation of the HR image tiles of the epidermis for further analysis. Experimental results show that the proposed framework provides a good performance.

Chapter 5 focused on the segmentation of the nuclei in epidermis area. A novel computer-aided technique for segmentation of the nuclei in histopathological images is proposed. In the proposed technique, the hybrid morphological reconstructions operations are first applied to reduce the noise and the intra-object intensity variations. A novel threshold selection algorithm for local regions is then used to

segment the nuclei. By incorporating the domain specific knowledge, this technique reduces the under-segmentation effect and provides a superior performance compared to the existing techniques.

Chapter 6 presented two techniques for melanocytes detection in the epidermis area. By utilizing the pre-segmented nuclei regions, these two techniques distinguish the melanocytes and other nuclei by using two different methods. In the LDED technique, a double elliptical model is constructed and the image data within the double elliptical model is analyzed using Gaussian mixture model. A set of two parameters is then estimated by the double elliptical model for detecting the melanocytes. In the RLS technique, the boundary of the halo pattern is estimated by the radial line and the gradient information. Based on the observation that the melanocytes have larger halo regions compared to other nuclei, the ratio of the estimated halo region and the nuclei region is used to differentiate the melanocytes and other nuclei.

Chapter 7 considered the mitotic cell detection and segmentation problem in multi-spectral histopathological image. We developed an efficient technique for detecting and segmenting the mitotic cells in high resolution multi-spectral image. The proposed technique consists of three main modules: discriminative image generation, mitotic cell candidates detection and segmentation, and mitotic cell candidates classification. The proposed technique is able to provide superior performance compared to the existing technique, 81.5% sensitivity rate and 33.9% precision rate in terms of detection performance, and 89.3% sensitivity rate and 87.5% precision rate in terms of segmentation performance.

Chapter 8 investigated the classification of the whole slide skin biopsy between melanoma, melanocytic nevus and normal skin. Based on the pre-segmented melanocytes and other keratinocytes, the feature based on the spatial distribution and the morphological features of melanocytes are constructed. These features are used as the input for a multi-class SVM classifier. The classification performance using all features archives around 90% accuracy in 10-fold cross validation, which suggest that the constructed features are effective to differentiate the the whole slide

skin biopsy between melanoma, melanocytic nevus and normal skin.

9.2 Publications

Parts of this thesis have been published in (or submitted) to the following journals and conferences:

- Cheng Lu, Muhammad Mahmood, Naresh Jha, Mrinal Mandal. "A Robust Automatic Nuclei Segmentation Technique for Quantitative Histopathological Image Analysis " *Analytical and Quantitative Cytology and Histopathology*. December 2012, P. 296-308.

- Cheng Lu, Muhammad Mahmood, Naresh Jha, Mrinal Mandal. "Detection of Melanocytes in Skin Histopathological Images using Radial Line Scanning", *Pattern Recognition*. Volume 46, Issue 2, February 2013, P. 509-518.

- Cheng Lu, Muhammad Mahmood, Naresh Jha, Marinal Mandal. "Automated Segmentation of the Melanocytes in Skin Histopathological Images", *IEEE Journal of Biomedical and Health Informatics (formerly named IEEE Transactions on Information Technology in Biomedicine)*. Vol. 17, NO. 2, March 2013, P. 284-296.

- Cheng Lu, Mrinal Mandal. "Automated Segmentation and Analysis of the Epidermis Area in Skin Histopathological Images", *In Proc: The 34th Annual International Conference of the Engineering in Medicine and Biology Society (EMBC 2012)*. August 2012, P. 5355-5359.

- Cheng Lu, Mrinal Mandal, "Towards Automatic Mitotic Cells Detection and Segmentation in Multi-spectral Histopathological Images", *IEEE Journal of Biomedical and Health Informatics (formerly named IEEE Transactions on Information Technology in Biomedicine)*. Accepted.

- Cheng Lu, Mrinal Mandal, "Automated Analysis and Diagnosis of Skin Melanoma on Whole Slide Histopathological Images", *submitted to Pattern Recognition*.

9.3 Future Work

In this thesis, several techniques for automatic quantitative analysis of skin WSI are described. However, more research work should be done to improve the efficiency of the CAD system. A few selected future research directions are presented as follows.

Depth of Invasion

As discussed in this thesis, we are mainly focusing on analyzing the cytological components in the epidermis area. Note that there is another key feature that will provide important diagnosis information - the depth of invasion of melanocytes. This requires analyzing the cytological components in dermis area. An efficient way to quantify the depth of the melanocytes invasion is to utilize the MART-1 staining slide, where the melanocytes are stained with dark brown color. In the MART-1 staining slide, it is very easy to identify all the melanocytes since the color is well differentiate with other cytological components.

Improvement of Mitosis Detection

Mitotic count is an important parameter in cancer grading and detection [80]. However, detection of mitotic cell in the HPF H&E stained histopathological image is a very challenging task. In Chapter 7, an efficient technique is proposed for solving the mitotic cells detection problem with multi-spectral histopathological images (with 10 bands). This technique provides satisfactory recall rate, but the precision is around 33%. Improving the precision rate is still a challenge problem. In additional, there is a large number of histopathological images captured in a RGB format. An efficient technique for RGB color format image is still required. The sparse representation and classification technique is a powerful technique for object representation and classification task [101]. By presenting a mitotic cell with a few representative samples, it is expected to differentiate the true mitotic cell from other types of cells. Alternatively, we can assess the skin tissue with mitosis-specific marker Phospho-Histone H3 Ser10 (PHH3). In such special staining image,

the mitotic cells are highlighted by brown color, which can be easily differentiated with other cytological components [102], [103]. The mitosis detection problem thus still an open problem to be solved.

Analysis and inclusion of additional features in the dermis area

In this thesis, we mainly focus on analyzing the epidermis of the skin tissue. There are many cases in which the diagnosis information is obtain from the dermis area. For example, the vascular regions in the dermis area is an important observation area. The present of cancel cells in such area indicates vascular invasion which is a serious case of the cancer. In the future, other types of cytological components in the dermis area, i.e., the lymphocytes, solar elastosis, will provide useful information for the final classification and diagnosis.

Subtypes of Melanocytic Nevus and Melanoma

In this work, I present a CAD system that can classify the melanoma, melanocytic nevus, and normal skin biopsies. The distinguish within the subtype of melanoma and melanocytic nevus will be a more challenging research topic. By achieving this goal, dedicated analysis among the classes is required.

References

[1] J. Tang, R. Rangayyan, J. Xu, I. El Naqa, and Y. Yang, "Computer-aided detection and diagnosis of breast cancer with mammography: Recent advances," *IEEE Transactions on Information Technology in Biomedicine*, vol. 13, no. 2, pp. 236–251, 2009.

[2] T. Xu, I. Cheng, and M. Mandal, "An improved fluid vector flow for cavity segmentation in chest radiographs," in *2010 20th International Conference on Pattern Recognition (ICPR)*. IEEE, 2010, pp. 3376–3379.

[3] Y. Jiang, R. M. Nishikawa, R. A. Schmidt, A. Y. Toledano, and K. Doi, "Potential of computer-aided diagnosis to reduce variability in radiologistsŠ interpretations of mammograms depicting microcalcifications1," *Radiology*, vol. 220, no. 3, pp. 787–794, 2001.

[4] I. Maglogiannis and C. Doukas, "Overview of advanced computer vision systems for skin lesions characterization," *IEEE Transactions on Information Technology in Biomedicine*, vol. 13, no. 5, pp. 721–733, 2009.

[5] American Cancer Society, "What are the key statistics about melanoma?" American Cancer Society, Tech. Rep., 2008.

[6] D. Rigel, J. Russak, and R. Friedman, "The evolution of melanoma diagnosis: 25 years beyond the ABCDs," *CA: A Cancer Journal for Clinicians*, vol. 60, no. 5, pp. 301–316, 2010.

[7] M. Vestergaard, P. Macaskill, P. Holt, and S. Menzies, "Dermoscopy compared with naked eye examination for the diagnosis of primary melanoma: a meta-analysis of studies performed in a clinical setting," *British Journal of Dermatology*, vol. 159, no. 3, pp. 669–676, 2008.

[8] V. Kumar, A. Abbas, N. Fausto, *et al.*, *Robbins and Cotran pathologic basis of disease*. Elsevier Saunders Philadelphia:, 2005.

[9] S. Ismail, A. Colclough, J. Dinnen, D. Eakins, D. Evans, E. Gradwell, J. O'Sullivan, J. Summerell, and R. Newcombe, "Observer variation in histopathological diagnosis and grading of cervical intraepithelial neoplasia." *British Medical Journal*, vol. 298, no. 6675, p. 707, 1989.

[10] M. Rojo, G. García, C. Mateos, J. García, and M. Vicente, "Critical comparison of 31 commercially available digital slide systems in pathology," *International Journal of Surgical Pathology*, vol. 14, no. 4, pp. 285–305, 2006.

[11] R. Weinstein, A. Graham, L. Richter, G. Barker, E. Krupinski, A. Lopez, K. Erps, A. Bhattacharyya, Y. Yagi, and J. Gilbertson, "Overview of telepathology, virtual microscopy, and whole slide imaging: prospects for the future," *Human pathology*, vol. 40, no. 8, p. 1057, 2009.

[12] S. Petushi, F. U. Garcia, M. M. Haber, C. Katsinis, and A. Tozeren, "Large-scale computations on histology images reveal grade-differentiating parameters for breast cancer." *BMC Med Imaging*, vol. 6, p. 14, 2006.

[13] C. Huang, A. Veillard, L. Roux, N. Lomenie, and D. Racoceanu, "Time-efficient sparse analysis of histopathological whole slide images," *Computerized Medical Imaging and Graphics*, 2010.

[14] S. Doyle, M. Feldman, J. Tomaszewski, and A. Madabhushi, "A boosted bayesian multi-resolution classifier for prostate cancer detection from digitized needle biopsies," *IEEE Transactions on Biomedical Engineering*, no. 99, pp. 1–1, 2010.

[15] M. Mete, X. Xu, C.-Y. Fan, and G. Shafirstein, "Automatic delineation of malignancy in histopathological head and neck slides." *BMC Bioinformatics*, vol. 8 Suppl 7, p. S17, 2007. [Online]. Available: http://dx.doi.org/10.1186/1471-2105-8-S7-S17

[16] Y. Wang, D. Crookes, O. S. Eldin, S. Wang, P. Hamilton, and J. Diamond, "Assisted diagnosis of cervical intraepithelial neoplasia (cin)," *IEEE Journal of Selected Topics in Signal Processing*, vol. 3, no. 1, pp. 112–121, 2009.

[17] O. Sertel, J. Kong, H. Shimada, U. V. Catalyurek, J. H. Saltz, and M. N. Gurcan, "Computer-aided prognosis of neuroblastoma on whole-slide images: Classification of stromal development," *Pattern Recognition*, vol. 42, no. 6, pp. 1093–1103, 2009.

[18] J. Kong, O. Sertel, H. Shimada, K. L. Boyer, J. H. Saltz, and M. N. Gurcan, "Computer-aided evaluation of neuroblastoma on whole-slide histology images: Classifying grade of neuroblastic differentiation," *Pattern Recognition*, vol. 42, no. 6, pp. 1080–1092, 2009.

[19] N. Signolle, M. Revenu, B. Plancoulaine, and P. Herlin, "Wavelet-based multiscale texture segmentation: Application to stromal compartment characterization on virtual slides," *Signal Processing*, vol. 90, no. 8, pp. 2412–2422, 2010.

[20] C. Lu and M. Mandal, "Automated segmentation and analysis of the epidermis area in skin histopathological images," in *2012 Annual International Conference of the IEEE Engineering in Medicine and Biology Society (EMBC)*, 2012, pp. 5355–5359.

[21] C. Lu, M. Mahmood, N. Jha, and M. Mandal., "A robust automatic nuclei segmentation technique for quantitative histopathological image analysis," *Analytical and Quantitative Cytology and Histopathology*, vol. Vol. 12, pp. 296–308, 2012.

[22] C. Lu, M. Mahmood, N. Jha, and M. Mandal, "Automated segmentation of the melanocytes in skin histopathological images." *IEEE Transactions on Information Technology in Biomedicine*, 2012.

[23] ——, "Detection of melanocytes in skin histopathological images using radial line scanning," *Pattern Recognition*, vol. Volume 46, Issue 2, pp. 509–518, 2013.

[24] C. Lu and M. Mandal, "Towards automatic mitosis detection and segmenation using multi-spectral h&e staining histopathological images," *under review*, 2013.

[25] C. Lu, M. Mahmood, N. Jha, and M. Mandal, "Automated diagnosis system for skin whole slide hitopathological images," submited to Pattern Recognition.

[26] MedicineNet, Inc., "Medicinenet.com, we bring doctor's knowledge to you," website, 1996. [Online]. Available: http://www.medterms.com

[27] National Cancer Institute, "Treatment statement for patients: Melanoma treatment (pdq)," website, Feb. 2011. [Online]. Available: https://www.meb.uni-bonn.de/Cancernet

[28] R. Odom, W. James, T. Berger, *et al.*, *Andrews' diseases of the skin: clinical dermatology*. Saunders Philadelphia, 2000.

[29] Dermatology, University of Iowa, "Normal skin histologic image," Website, 1995. [Online]. Available: http://tray.dermatology.uiowa.edu/DPT/Hist/Nrml-001.htm

[30] O. Sertel, U. Catalyurek, H. Shimada, and M. Guican, "Computer-aided prognosis of neuroblastoma: Detection of mitosis and karyorrhexis cells in digitized histological images," in *Proc. of International Conference of the IEEE Engineering in Medicine and Biology Society (EMBC).*, 2009, pp. 1433–1436.

[31] V. Roullier, O. Lezoray, V. Ta, and A. Elmoataz, "Multi-resolution graph-based analysis of histopathological whole slide images: Application to mitotic cell extraction and visualization," *Computer medical imaging and graph*, 2011.

[32] M. Gurcan, T. Pan, H. Shimada, and J. Saltz, "Image analysis for neuroblastoma classification: Segmentation of cell nuclei," in *Proce. of the 28th IEEE Annual International Conference of EMBS*, 2006, pp. 4844 – 4847.

[33] V. Korde, H. Bartels, J. Barton, and J. Ranger-Moore, "Automatic Segmentation of Cell Nuclei in Bladder and Skin Tissue for Karyometric Analysis," *Analytical and quantitative cytology and histology*, vol. 31, no. 2, p. 83, 2009.

[34] M. Sezgin and B. Sankur, "Survey over image thresholding techniques and quantitative performance evaluation," *Journal of Electronic imaging*, vol. 13, p. 146, 2004.

[35] L. Vincent and P. Soille, "Watersheds in digital spaces: an efficient algorithm based on immersion simulations," *IEEE transactions on pattern analysis and machine intelligence*, vol. 13, no. 6, pp. 583–598, 1991.

[36] X. Zhou, F. Li, J. Yan, and S. Wong, "A novel cell segmentation method and cell phase identification using Markov model," *IEEE Transactions on Information Technology in Biomedicine*, vol. 13, no. 2, pp. 152–157, 2009.

[37] J. Cheng and J. Rajapakse, "Segmentation of clustered nuclei with shape markers and marking function," *IEEE Transactions on Biomedical Engineering*, vol. 56, no. 3, pp. 741–748, 2009.

[38] C. Jung and C. Kim, "Segmenting Clustered Nuclei Using H-minima Transform-Based Marker Extraction and Contour Parameterization," *IEEE Transactions on Biomedical Engineering*, vol. 57, no. 10, pp. 2600–2604, 2010.

[39] S. Naik, S. Doyle, M. Feldman, J. Tomaszewski, and A. Madabhushi, "Gland segmentation and computerized gleason grading of prostate histology by integrating low-, high-level and domain specific information," in *MIAAB Workshop*. Citeseer, 2007.

[40] O. Sertel, U. Catalyurek, H. Shimada, and M. Guican, "Computer-aided Prognosis of Neuroblastoma: Detection of mitosis and karyorrhexis cells in digitized histological images," in *Proceeding of the 31th IEEE Annual International Conference of EMBS*. IEEE, 2009, pp. 1433–1436.

[41] A. N. Basavanhally, S. Ganesan, S. Agner, J. P. Monaco, M. D. Feldman, J. E. Tomaszewski, G. Bhanot, and A. Madabhushi, "Computerized image-based detection and grading of lymphocytic infiltration in HER2+ breast cancer histopathology," *IEEE Transactions on Biomedical Engineering*, vol. 57, no. 3, pp. 642–653, 2010.

[42] H. Fatakdawala, J. Xu, A. Basavanhally, G. Bhanot, S. Ganesan, M. Feldman, J. Tomaszewski, and A. Madabhushi, "Expectation–maximization-driven geodesic active contour with overlap resolution (EMaGACOR): Application to lymphocyte segmentation on breast cancer histopathology," *IEEE Transactions on Biomedical Engineering*, vol. 57, no. 7, pp. 1676–1689, 2010.

[43] S. Acton and N. Ray, *Biomedical Image Analysis: Segmentation*. Morgan & Claypool Publishers, 2009, vol. 4, no. 1.

[44] J. Sethian, *Level set methods and fast marching methods: evolving interfaces in computational geometry, fluid mechanics, computer vision, and materials science*. Cambridge Univ Press, 1999.

[45] I. Sintorn, M. Homman-Loudiyi, C. Söderberg-Nauclér, and G. Borgefors, "A refined circular template matching method for classification of human cytomegalovirus capsids in tem images," *Computer methods and programs in biomedicine*, vol. 76, no. 2, pp. 95–102, 2004.

[46] S. Naik, S. Doyle, S. Agner, A. Madabhushi, M. Feldman, and J. Tomaszewski, "Automated gland and nuclei segmentation for grading of prostate and breast cancer histopathology," in *Proc. 5th IEEE Int. Symp. Biomedical Imaging: From Nano to Macro ISBI 2008*, 2008, pp. 284–287.

[47] Y. Al-Kofahi, W. Lassoued, W. Lee, and B. Roysam, "Improved automatic detection and segmentation of cell nuclei in histopathology images," *IEEE Transactions on Biomedical Engineering*, vol. 57, no. 4, pp. 841–852, 2010.

[48] C. Demir and B. Yener, "Automated cancer diagnosis based on histopathological images: a systematic survey," *Rensselaer Polytechnic Institute, Tech. Rep*, 2005.

[49] M. N. Gurcan, L. E. Boucheron, A. Can, A. Madabhushi, N. M. Rajpoot, and B. Yener, "Histopathological image analysis: A review," *IEEE Journal of Reviews on Biomedical Engineering*, vol. 2, pp. 147–171, 2009.

[50] R. Haralick, K. Shanmugam, and I. Dinstein, "Textural features for image classification," *IEEE Transactions on systems, man and cybernetics*, vol. 3, no. 6, pp. 610–621, 1973.

[51] A. Gerger and J. Smolle, "Diagnostic imaging of melanocytic skin tumors," *Journal of Cutaneous Pathology*, vol. 30, no. 4, pp. 247–252, 2003.

[52] M. Galloway, "Texture analysis using gray level run lengths," *Computer graphics and image processing*, vol. 4, no. 2, pp. 172–179, 1975.

[53] A. Tosun and C. Gunduz-Demir, "Graph run-length matrices for histopathological image segmentation," *IEEE Transactions on Medical Imagin*, vol. 30, no. 3, pp. 721–732, 2011.

[54] S. Doyle, M. Hwang, K. Shah, A. Madabhushi, M. Feldman, and J. Tomaszeweski, "Automated grading of prostate cancer using architectural and textural image features," in *Proc. 4th IEEE Int. Symp. Biomedical Imaging: From Nano to Macro ISBI 2007*, 2007, pp. 1284–1287.

[55] M. Fitzgibbon, A. W.and Pilu and R. B. Fisher, "Direct least-squares fitting of ellipses," *IEEE Transactions on Pattern Analysis and Machine Intelligence*, vol. 21, no. 5, pp. 476–480, May 1999.

[56] R. Graham, "An efficient algorithm for determining the convex hull of a finite point set," *Info. Proc. Letters*, vol. 1, pp. 132–133, 1972.

[57] O. Sertel, J. Kong, U. V. Catalyurek, G. Lozanski, J. H. Saltz, and M. N. Gurcan, "Histopathological image analysis using model-based intermediate representations and color texture: Follicular lymphoma grading," *Journal of Signal Processing Systems for Signal Image and Video Technology*, vol. 55, no. 1-3, pp. 169–183, 2009.

[58] C. Bilgin, P. Bullough, G. Plopper, and B. Yener, "Ecm-aware cell-graph mining for bone tissue modeling and classification," *Data mining and knowledge discovery*, vol. 20, no. 3, pp. 416–438, 2010.

[59] D. Altunbay, C. Cigir, C. Sokmensuer, and C. Gunduz-Demir, "Color graphs for automated cancer diagnosis and grading." *IEEE Trans Biomed Eng*, vol. 57, no. 3, pp. 665–674, Mar 2010.

[60] M. Wiltgen, A. Gerger, and J. Smolle, "Tissue counter analysis of benign common nevi and malignant melanoma," *International Journal of Medical Informatics*, vol. 69, no. 1, pp. 17–28, 2003.

[61] L. Kuncheva and C. Whitaker, "Measures of diversity in classifier ensembles and their relationship with the ensemble accuracy," *Machine Learning*, vol. 51, no. 2, pp. 181–207, 2003.

[62] Y. Freund and R. Schapire, "Experiments with a new boosting algorithm," in *In Proceedings of the Thirteenth International Conference on Machine Learning*. Citeseer, 1996, pp. 148–156.

[63] J. Smolle, "Computer recognition of skin structures using discriminant and cluster analysis," *Skin Research and Technology*, vol. 6, no. 2, pp. 58–63, 2000.

[64] J. Smolle and A. Gerger, "Tissue counter analysis of tissue components in skin biopsies - evaluation using cart (classification and regression trees)," *American Journal of Dermatopathology*, vol. 25, no. 3, pp. 215–222, 2003.

[65] R. Duda, P. Hart, and D. Stork, *Pattern classification*. Citeseer, 2001, vol. 2.

[66] R. Gonzalez and R. Woods, *Digital image processing*, 2002.

[67] P. Burt and E. Adelson, "The laplacian pyramid as a compact image code," *IEEE Transactions on Communications*, vol. 31, no. 4, pp. 532–540, 1983.

[68] N. Otsu, "A threshold selection method from gray-level histograms," *IEEE Transactions on Systems, Man, and Cybernetics*, vol. 9, no. 1, pp. 62–66, 1979.

[69] B. Cambazoglu, O. Sertel, J. Kong, J. Saltz, M. Gurcan, and U. Catalyurek, "Efficient processing of pathological images using the grid: computer-aided prognosis of neuroblastoma," in *Proceedings of the 5th IEEE workshop on Challenges of large applications in distributed environments*. ACM, 2007, pp. 35–41.

[70] T. Fuchs and J. Buhmann, "Computational pathology: Challenges and promises for tissue analysis," *Computerized Medical Imaging and Graphics*, vol. 35, no. 7, pp. 515–530, 2011.

[71] D. Altman and J. Bland, "Measurement in medicine: the analysis of method comparison studies," *The statistician*, pp. 307–317, 1983.

[72] S. Hanneman, "Design, analysis and interpretation of method-comparison studies," *AACN advanced critical care*, vol. 19, no. 2, p. 223, 2008.

[73] B. Saha and N. Ray, "Image thresholding by variational minimax optimization," *Pattern Recognition*, vol. 42, no. 5, pp. 843–856, 2009.

[74] D. Weedon and G. Strutton, *Skin pathology*. Churchill Livingstone: New York, 2002, vol. 430.

[75] L. E. Boucheron, "Object- and spatial-level quantitative analysis of multispectral histopathology images for detection and characterization of cancer," Ph.D. dissertation, University of California, Santa Barbara, Mar 2008.

[76] X. Chen, X. Zhou, and S. T. Wong, "Automated segmentation, classification, and tracking of cancer cell nuclei in time-lapse microscopy," *Biomedical Engineering, IEEE Transactions on*, vol. 53, no. 4, pp. 762–766, 2006.

[77] T. W. Nattkemper, H. Wersing, W. Schubert, and H. Ritter, "A neural network architecture for automatic segmentation of fluorescence micrographs," *Neurocomputing*, vol. 48, no. 1, pp. 357–367, 2002.

[78] C. Bishop, *Neural networks for pattern recognition*. Oxford university press, 1995.

[79] J. Lewis, "Fast normalized cross-correlation," in *Vision Interface*, vol. 10. Citeseer, 1995, pp. 120–123.

[80] C. Elston and I. Ellis, "Pathological prognostic factors in breast cancer. I. the value of histological grade in breast cancer: experience from a large study with long-term follow-up," *Histopathology*, vol. 19, no. 5, pp. 403–410, 1991.

[81] IPAL, TRIBVN, Pitié-Salpêtrière Hospital, and The Ohio State University, "Mitosis detection in breast cancer histological images: an ICPR 2012 contest," HTTP://IPAL.CNRS.FR/ICPR2012/?Q=NODE/1, 2012.

[82] M. Schlachter, M. Reisert, C. Herz, F. Schlurmann, S. Lassmann, M. Werner, H. Burkhardt, and O. Ronneberger, "Harmonic filters for 3d multichannel

data: Rotation invariant detection of mitoses in colorectal cancer," *IEEE Transactions on Medical Imaging*, vol. 29, no. 8, pp. 1485–1495, 2010.

[83] A. Liu, K. Li, and T. Kanade, "Mitosis sequence detection using hidden conditional random fields," in *2010 IEEE International Symposium on Biomedical Imaging: From Nano to Macro*. IEEE, 2010, pp. 580–583.

[84] S. Huh, D. Ker, R. Bise, M. Chen, and T. Kanade, "Automated mitosis detection of stem cell populations in phase-contrast microscopy images," *IEEE Transactions on Medical Imaging*, vol. 30, no. 3, pp. 586–596, 2011.

[85] G. Lin, W. Wang, C. Wang, and S. Sun, "Automated classification of multispectral mr images using linear discriminant analysis." *Computerized medical imaging and graphics: the official journal of the Computerized Medical Imaging Society*, vol. 34, no. 4, p. 251, 2010.

[86] R. Chen, X. Lin, and T. Ding, "Liveness detection for iris recognition using multispectral images," *Pattern Recognition Letters*, 2012.

[87] J. Prats-Montalbán, A. De Juan, and A. Ferrer, "Multivariate image analysis: A review with applications," *Chemometrics and Intelligent Laboratory Systems*, vol. 107, no. 1, pp. 1–23, 2011.

[88] M. Dalla Mura, A. Villa, J. Benediktsson, J. Chanussot, and L. Bruzzone, "Classification of hyperspectral images by using extended morphological attribute profiles and independent component analysis," *Geoscience and Remote Sensing Letters, IEEE*, vol. 8, no. 3, pp. 542–546, 2011.

[89] L. Boucheron, N. Harvey, and B. Manjunath, "Utility of multispectral imaging for analysis of routine clinical histopathology imagery," in *Workshop on Multiscale Biological Imaging, Data Mining, & Informatics, Santa Barbara, CA*, 2006.

[90] H. Yu and J. Yang, "A direct lda algorithm for high-dimensional data-with application to face recognition," *Pattern recognition*, vol. 34, no. 10, p. 2067, 2001.

[91] H. Tamura, S. Mori, and T. Yamawaki, "Textural features corresponding to visual perception," *IEEE Transactions on Systems, Man and Cybernetics*, vol. 8, no. 6, pp. 460–473, 1978.

[92] T. Jo and N. Japkowicz, "Class imbalances versus small disjuncts," *ACM SIGKDD Explorations Newsletter*, vol. 6, no. 1, pp. 40–49, 2004.

[93] G. Batista, A. Carvalho, and M. Monard, "Applying one-sided selection to unbalanced datasets," *MICAI 2000: Advances in Artificial Intelligence*, pp. 315–325, 2000.

[94] R. Barandela, J. Sánchez, V. García, and E. Rangel, "Strategies for learning in class imbalance problems," *Pattern Recognition*, vol. 36, no. 3, pp. 849–851, 2003.

[95] R. Barandela, R. Valdovinos, and J. Sánchez, "New applications of ensembles of classifiers," *Pattern Analysis & Applications*, vol. 6, no. 3, pp. 245–256, 2003.

[96] S. Kotsiantis and P. Pintelas, "Mixture of expert agents for handling imbalanced data sets," *Annals of Mathematics, Computing & Teleinformatics*, vol. 1, no. 1, pp. 46–55, 2003.

[97] N. Cristianini and J. Shawe-Taylor, *An introduction to support Vector Machines and other kernel-based learning methods*. Cambridge Univ Pr, 2000.

[98] U. Kreßel, "Pairwise classification and support vector machines," in *Advances in kernel methods*. MIT Press, 1999, pp. 255–268.

[99] K. Crammer and Y. Singer, "On the learnability and design of output codes for multiclass problems," *Machine Learning*, vol. 47, no. 2, pp. 201–233, 2002.

[100] C. Hsu and C. Lin, "A comparison of methods for multiclass support vector machines," *IEEE Transactions on Neural Networks*, vol. 13, no. 2, pp. 415–425, 2002.

[101] J. Wright, A. Y. Yang, A. Ganesh, S. S. Sastry, and Y. Ma, "Robust face recognition via sparse representation," *IEEE Transactions on Pattern Analysis and Machine Intelligence*, vol. 31, no. 2, pp. 210–227, 2009.

[102] M. Angi, B. Damato, H. Kalirai, A. Dodson, A. Taktak, and S. E. Coupland, "Immunohistochemical assessment of mitotic count in uveal melanoma," *Acta ophthalmologica*, vol. 89, no. 2, pp. e155–e160, 2011.

[103] K. Ikenberg, M. Pfaltz, C. Rakozy, and W. Kempf, "Immunohistochemical dual staining as an adjunct in assessment of mitotic activity in melanoma," *Journal of Cutaneous Pathology*, vol. 39, no. 3, pp. 324–330, 2012.

[104] Wikimedia Foundation, Inc., "Wikipedia, the free encyclopedia," website, Feb. 2011. [Online]. Available: http://en.wikipedia.org

[105] H. L. Brannon, "Epidermis anatomy," Website, September 2007. [Online]. Available: http://dermatology.about.com/od/skindiseases/a/skindisease.htm

[106] J. McGrath, R. Eady, and F. Pope, "Anatomy and organization of human skin," *Rook's textbook of dermatology*, pp. 3–1, 2004.

[107] A. Yung, "The structure of normal skin," Website, April 2010. [Online]. Available: http://www.dermnetnz.org/pathology/skin-structure.html

[108] M. Ross, G. Kaye, and W. Pawlina, *Histology: a text and atlas: with cell and molecular biology*. Lippincott Williams & Wilkins, 2003.

[109] F. J. W.-M. Leong and A. S. Y. Leong, "Digital imaging in pathology: theoretical and practical considerations, and applications." *Pathology*, vol. 36, no. 3, pp. 234–241, Jun 2004. [Online]. Available: http://dx.doi.org/10.1080/00313020410001692576

[110] X. Ying and T. M. Monticello, "Modern imaging technologies in toxicologic pathology: An overview." *Toxicol Pathol*, vol. 34, no. 7, pp. 815–826, 2006.

[111] Carl Zeiss MicroImaging, "Mirax midi-the versatile slide scanner for research and routine," Website, 2009. [Online]. Available: www.zeiss.de/mirax

[112] T. D. Chiara, "What is skin cancer," Website, May 2009. [Online]. Available: http://skincancer.about.com/od/skincancerbasics/a/Skin_Cancer.htm

[113] ——, "Introduction to melanoma skin cancer," Website, October 2009. [Online]. Available: http://skincancer.about.com/od/skincancerbasics/a/Melanoma.htm

Appendix A

Histopathological Knowledge

A.1 Physiological Terms

In this section, some important physiological terms related to dermatopathology are defined [8], [26], [104].

A.1.1 General Terms

- **Pathology:** “Pathology is the study (logos) of disease (pathos). More specifically, it is devoted to the study of the structural, biochemical, and functional changes in cells, tissues, and organs that underlie disease." [8]
- **Cytology:** “The medical and scientific study of cells.” [26]
- **Cytopathology:** “A branch of pathology that studies and diagnoses diseases on the cellular level." [26]
- **Histopathology:** “ Histopathology refers to the microscopic examination of tissue in order to study the manifestations of disease. Specifically, in clinical medicine, histopathology refers to the examination of a biopsy or surgical specimen by a pathologist, after the specimen has been processed and histological sections have been placed onto glass slides. In contrast, cytopathology examines free cells or tissue fragments." [26]

- **Dermatopathology:** “Dermatopathology is a subspecialty of dermatology and surgical pathology that consist in the study of skin disease at a microscopic level."[104]

- **Cytoplasm:** “The cytoplasm is a thick liquid residing between the cell membrane holding organelles, except for the nucleus." [26]

- **Nucleus:** “is a membrane-enclosed organelle found in eukaryotic cells. It contains most of the cell’s genetic material, organized as multiple long linear DNA molecules in complex with a large variety of proteins to form chromosomes." [26]

- **Nucleolus:** “The nucleolus (also called nucleole) is a non-membrane bound structure composed of proteins and nucleic acids found within the nucleus." [26]

- **Mitosis:** “Mitosis is the process by which a eukaryotic cell separates the chromosomes in its cell nucleus into two identical sets in two nuclei." [26]

A.1.2 Four Layers in Skin Epidermis

- **Basal layer:** Also termed the stratum basale. It is the bottom layer of keratinocytes in the epidermis. It has cells that are shaped like columns. In this layer the cells divide and push already formed cells into higher layers [105].

- **Spinous layer:** Also termed the prickle cell layer or stratum spinosum. The center of epidermis that has a spiny appearance where keratinocytes produce keratin [105]. Intercellular bridges called desmosomes link the cells together.

- **Granular layer:** Also termed the stratum granulosum. The cells in this layer lost their nuclei and are featured by dark clumps of cytoplasmic material [105].

- **Cornified layer:** Also termed the stratum corneum, keratin layer. The cells in this layer have flattened out and are composed mainly of keratin protein [105].

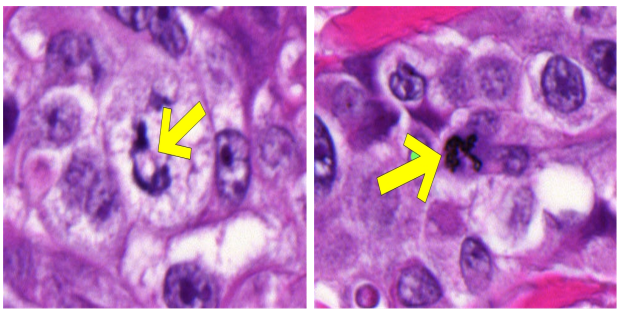

(a) Mitosis 1 (b) Mitosis 2

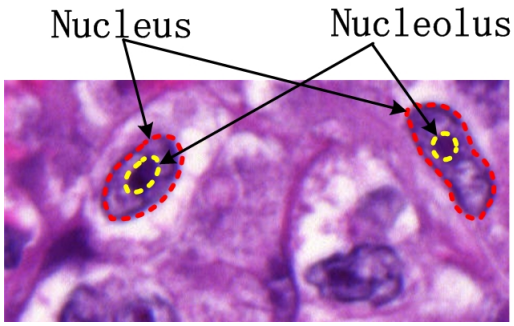

(c) Nucleus and nucleolus

Fig. A.1. The atlas of cytological components.

A.1.3 Biological Components in Skin Tissue

- **Keratinocytes:** Keratinocytes are the predominant cell type in the epidermis, the outermost layer of the human skin, constituting 95% of the cells found there [106]. The keratinocytes become more mature or differentiated and accumulate keratin as they move outwards. They eventually fall or rub off. They form four distinct layers in the epidermis which will be introduced in next subsection [105].

- **Melanocytes:** Melanocytes are found in the lower part of the epidermis (Figure 2.3). Melanocytes prefer to have plain cytoplasm and round, oval, high staining nucleus in normal skin. A pigment-producing cell in the skin, hair and eye that determines their color [26]. They produce the pigment, called melanin, which is packaged into small parcels (or called melanosomes) are then transferred to keratinocytes [107].

- **Langerhans cells:** “Langerhans cells are immune cells found in the epidermis, and are responsible for helping the body learn and later recognize new ąőallergensąf (material foreign to the body)” [107]. Langerhans cells usually have complex, lobed, dense staining nuclei and usually found in spinous layer.

- **Papillary dermis:** “The uppermost layer of the dermis, intertwined with the rete ridges of the epidermis, composed of fine and loosely arranged collagen fibers." [26]

- **Reticular dermis:** “The reticular dermis is the lower layer of the dermis, found under the papillary dermis, composed of thick, densely packed collagen fibers, and the primary location of dermal elastic fibers." [26]

- **Hair follicle:** “A sac from which a hair grows and into which the sebaceous (oil) glands open. The follicle is lined by cells derived from the epidermal (outside) layer of the skin." [26]

- **Sweat gland:** “The sweat (sudoriferous) glands are small tubular structures situated within and under the skin (in the subcutaneous tissue). They discharge sweat by tiny openings in the surface of the skin." [26]

- **Lymphocyte:** “A small white blood cell (leukocyte) that plays a large role in defending the body against disease." [26]

- **Red blood cell:** “The blood cells that carry oxygen. Red cells contain hemoglobin and it is the hemoglobin which permits them to transport oxygen (and carbon dioxide)." [26]

- **Endothelial progenitor cell:** “A primitive cell made in the bone marrow that can enter the bloodstream and go to areas of blood vessel injury to help repair the damage." [26]

- **Nevus:** “1. Any birthmark. 2. A benign pigmented spot on the skin such as a mole (a cluster of melanocytes and supportive tissue that appears as a tan,

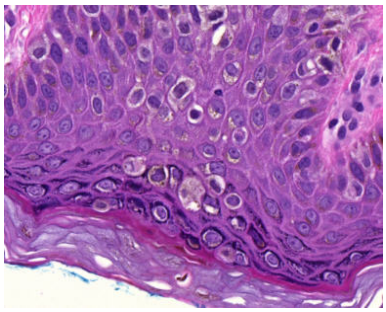

(a) Atypical melanocytes in epidermis area

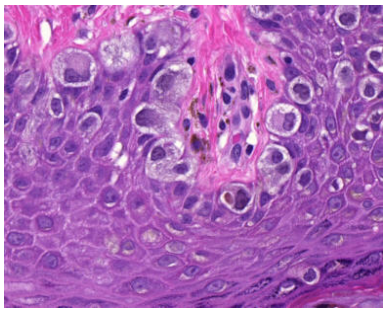

(b) Atypical melanocytes in epidermis area

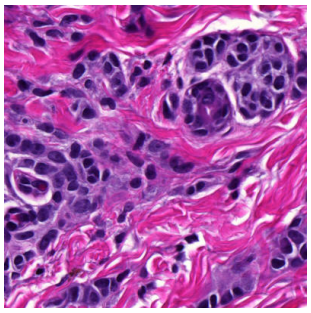

(c) Melanocytes in dermis area

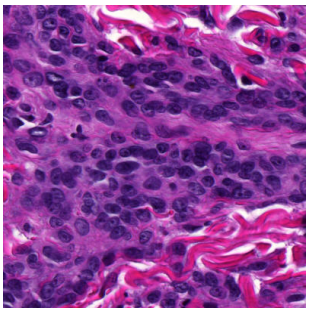

(d) Melanocytes in dermis area

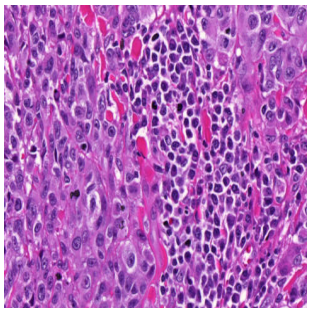

(e) Melanocytes in dermis area

Fig. A.2. The atlas of melanocytes.

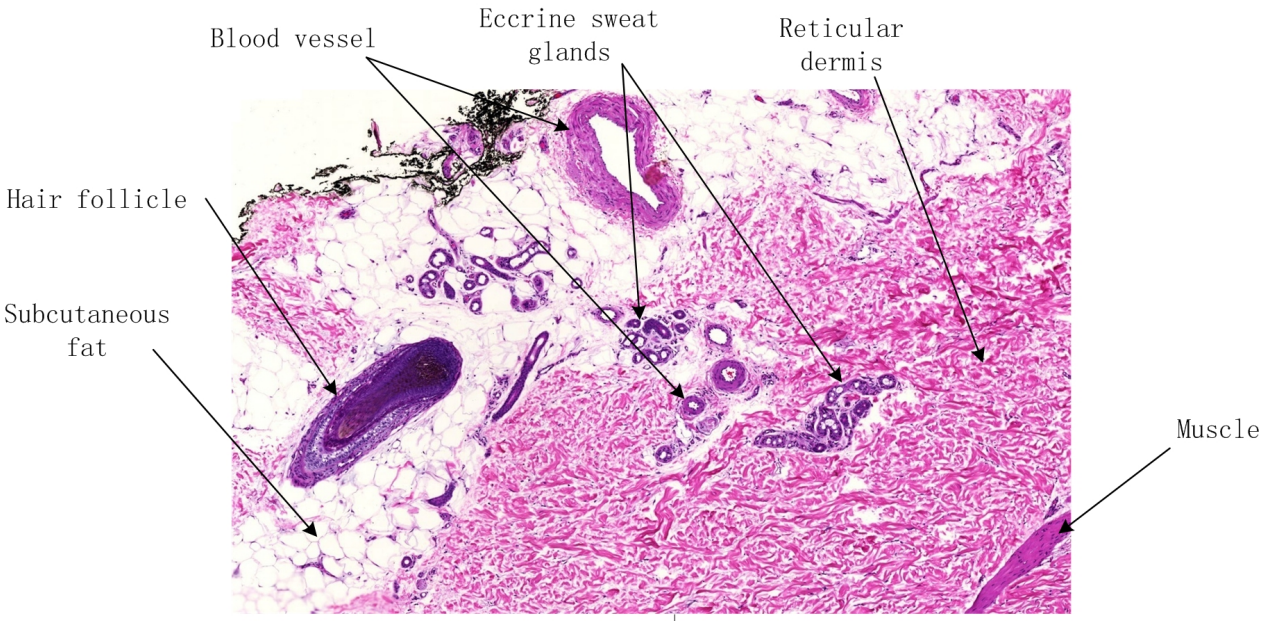

(a) The anatomy in the dermis-sebaceous junctional

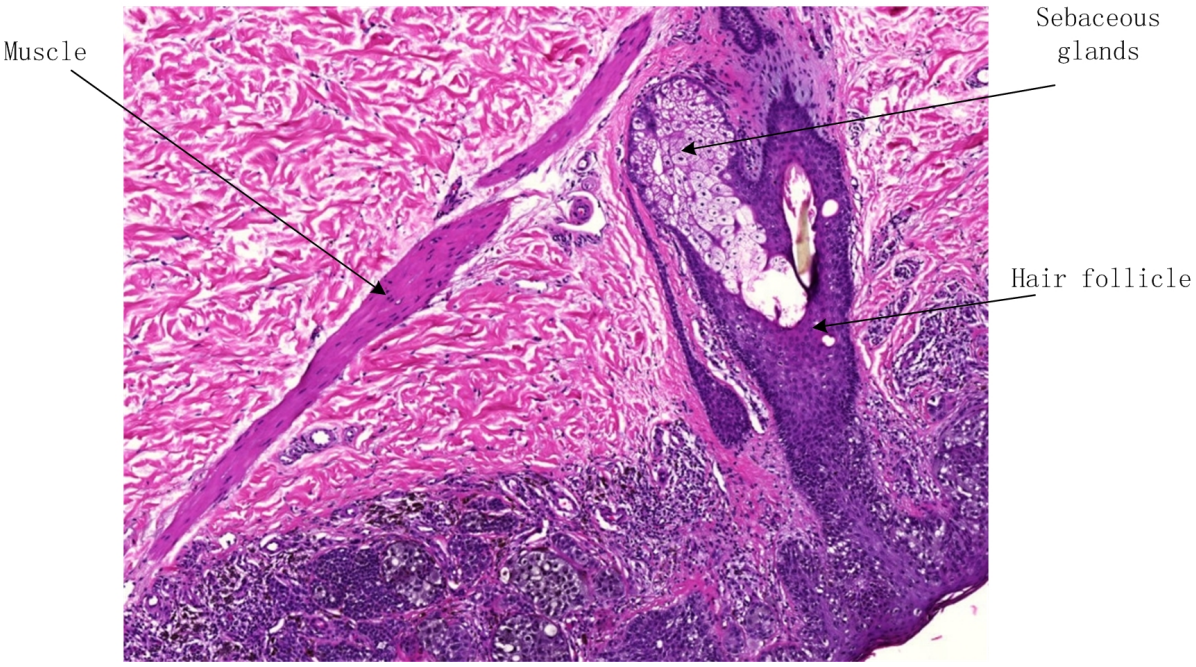

(b) Hair follicle and sebaceous gland in the Epidermis-dermis junctional

Fig. A.3. The anatomy of histopathology skin specimen. (under 5X magnification, H&E stained)

brown, or flesh-colored spot on the skin). 3. A benign blood vessel tumor on the skin such as a vascular nevus, a local collection of capillaries of the skin (a strawberry birthmark, stork mark, or port wine stain)." [26]

- **Melanoma:** “Melanoma is a type of skin cancer. It begins in cells in the skin called melanocytes.” [26]
- **Solar/Actinic elastosis:** “Degeneration of subdermal elastic tissue by prolonged sun exposure, causing wrinkling ’sailor skin’- aka, farmer’s skin, golfer’s skin, which predisposes skin to malignancy, e.g., melanoma." [26]

A.2 Tissue Slide Preparation

The histological tissue slide preparation follows the following process[104], [108]:

- **Tissue Fixation:** Chemical fixatives are used to maintain the structure of the cell and of sub-cellular components such as cell organelles (e.g., nucleus, endoplasmic reticulum, mitochondria).
- **Tissue Embedding:** In this step the water is removed and replaced with a medium that let tissue solidifies. After that the tissue samples are placed into molds and ready to be sectioned.
- **Tissue Sectioning:** The tissue samples are cut into thin sections (about 5 - 15 μm) by steel knife. Then the thin sections are mounted on a glass slide for the appropriate stain.
- **Tissue Staining:** Staining creates contrast between cell organelles, which is necessary to observe features of interest. Hematoxylin and Eosin (H&E) is the basic staining methodology in pathology. In the H&E method, the alkaline hematoxylin colors cell nuclei blue while the acidic eosin colors cytoplasm, connective tissues and other organelles different shades of pink. In this dissertation, except special annotation, the histopathology image are all H&E staining.

A.3 Histopathological Image Acquisition

After the tissue slide preparation, the tissue glass slide is ready to be scanned and stored as digital images for further analysis. The digitization requires the digital micro-imaging system which usually consists of a digital camera, a computer, a digital image input device, imaging software, and an optical connector to the microscope. The pathologist can browser, analysis, capture the region of interest as digital image with the help of the computer. With the rapid development of microscopy imaging techniques, it is now possible to digitized the whole tissue slide [109].

Technically, automated microscopy imaging for digitizing an whole slide employs one of the following three basic slide scanning techniques [110].

- **Automated area-scan micro-imaging**, which involves ąőtile-by-tileą́ acquisition over the entire tissue followed by a stitching of images to form an entire digital slide.
- **Automated 1D line-scan microimaging**, which consists of linear scanning of small tissue section areas to form a ąőstrap imageą́ with further stitching of the straps to form a digital slide.
- **Array microscopy imaging** where a microlens array and a large 2D imaging chip are designed to scan the entire slide.

For example, the whole slide tissue image can be digitized by the Carl Zeiss MIRAX MIDI (CZMM) Scanning system [111]. CZMM is capable of 12 scanning tissue glass slides together within 5 minutes with 20X objective magnification. The CZMM utilizes the automated area-scan micro-imaging technology for the whole slide digitizing.

A.4 The Histopathological Aspects of Skin Tumors

Malignant Tumors: The skin cancer, or called malignant tumors occur when the abnormal cells grow at an uncontrollable speed. The three common forms of skin

cancer are distinguished by the types of cells affected. The descriptions for these three common skin cancer is shown in Table A.1. [112].

TABLE A.1
DESCRIPTION OF THREE COMMON SKIN CANCERS.

Name	Cells affected	Characteristics
Malignant melanomas	Abnormal growths of melanocytes	The most aggressive form of skin cancer; Spread quickly to other parts of the body; Fatal if not detected and treated early.
Squamous cell carcinomas	Middle layer of the epidermis	Can spread and life threatening if not treated appropriately.
Basal cell carcinoma	Cells at basal layer	The most common form of skin cancer; Not typically spread; Often develop in areas of the skin exposed to sun.

While melanoma accounts for roughly 4% of all skin cancers, it is responsible for more than 74% of skin cancer deaths. Melanoma is the most common form of cancer for young adults 25- to 29-years-old and the second most common cancer in adolescents and young adults 15- to 29-years-old. Unfortunately, it is increasing at a faster rate than any other cancer (with the exception of lung cancer in women). In the past 30 years, the incidence of malignant melanoma has increased by 270% [113].

Appendix B

Direct least square fitting algorithm

In Chapter 6-Sec. III(c) the elliptical model was introduced. In this appendix, the direct least square fitting algorithm is explained for fitting an ellipse with a nucleus.

Let $(u,\ v)$ be a 2-D point of an ellipse, and the ellipse is modeled using the following implicit second-order polynomial

$$E(u,v) = au^2 + buv + cv^2 + du + ev + f = 0 \tag{B-1}$$

with an ellipse-specific constraint $b^2 - 4ac < 0$, where a, b, c, d, e, and f denote the ellipse coefficients. Eq. B-1 can be rewritten in the vector form as follows.

$$E(u,v) = \mathbf{au} = 0 \tag{B-2}$$

where $\mathbf{a} = [a,\ b,\ c,\ d,\ e,\ f]^T$ and $\mathbf{u} = [u^2,\ uv,\ v^2,\ u,\ v,\ 1]$.

Assuming that $b^2 - 4ac = -r$, the inequality constraint $b^2 - 4ac < 0$ can be converted into an equality constraint $4ac - b^2 = r$ [55], where r is an arbitrary positive number. Without any loss of generality, let $r = 1$. The equality constraint can then be represented in matrix form as follows:

$$\mathbf{a}^T\mathbf{Ca} = 1 \tag{B-3}$$

where

$$\mathbf{C} = \begin{bmatrix} 0 & 0 & 2 & 0 & 0 & 0 \\ 0 & -1 & 0 & 0 & 0 & 0 \\ 2 & 0 & 0 & 0 & 0 & 0 \\ 0 & 0 & 0 & 0 & 0 & 0 \\ 0 & 0 & 0 & 0 & 0 & 0 \\ 0 & 0 & 0 & 0 & 0 & 0 \end{bmatrix}. \tag{B-4}$$

Assume a set of B boundary points corresponding to a candidate region. In the ideal case, all the boundary points will be on an ellipse defined by **a**, and will satisfy the following equation:

$$||\mathbf{Da}||^2 = 0 \tag{B-5}$$

where the design matrix **D** is defined as follows:

$$\mathbf{D} = \begin{bmatrix} u_1^2 & u_1 v_1 & v_1^2 & u_1 & v_1 & 1 \\ \vdots & \vdots & \vdots & \vdots & \vdots & \vdots \\ u_i^2 & u_i v_i & v_i^2 & u_i & v_i & 1 \\ \vdots & \vdots & \vdots & \vdots & \vdots & \vdots \\ u_B^2 & u_B v_B & v_B^2 & u_B & v_B & 1 \end{bmatrix} \tag{B-6}$$

where (u_i, v_i) denote the 2D coordinate of the ith boundary point for the region. In general, the boundary points will not form a perfect ellipse and Eq. B-5 will not be satisfied. The optimal coefficients vector $\hat{\mathbf{a}}$ corresponding to the best matched ellipse can be estimated by solving the following least square minimization:

$$\hat{\mathbf{a}} = arg\min_{\mathbf{a}} ||\mathbf{Da}||^2 \;\; subject\ to \;\; \mathbf{a}^T\mathbf{Ca} = 1. \tag{B-7}$$

Eq. B-7 can be solved via Lagrange multiplier method [55].